

**DETERMINATION OF FLAME CHARACTERISTICS IN  
A LOW SWIRL BURNER AT GAS TURBINE  
CONDITIONS THROUGH REACTION ZONE IMAGING**

A Dissertation  
Presented to  
The Academic Faculty

by

Karthik Periagaram

In Partial Fulfillment  
of the Requirements for the Degree  
Doctor of Philosophy in the  
Guggenheim School of Aerospace Engineering

Georgia Institute of Technology  
December 2012

# TABLE OF CONTENTS

<b>List of Figures</b>	<b>v</b>
<b>List of Tables</b>	<b>vii</b>
<b>List of Symbols</b>	<b>viii</b>
<b>Summary</b>	<b>ix</b>
<b>1 Introduction</b>	<b>1</b>
1.1 Motivation . . . . .	2
1.2 Literature Review . . . . .	7
1.2.1 Low Swirl Burner . . . . .	7
1.2.2 CH PLIF Implementations . . . . .	8
1.3 Objectives and Overview . . . . .	10
<b>2 Background</b>	<b>12</b>
2.1 LSB Reacting Flow Field . . . . .	12
2.1.1 Role of swirl and recirculation zones . . . . .	13
2.1.2 Axial velocity profile and self-similarity . . . . .	14
2.1.3 Flame stabilization mechanism . . . . .	16
2.1.4 Effect of Flow Parameters on Flame Characteristics . . . . .	16
2.1.4.1 Effect on Flame Standoff Distance . . . . .	17
2.1.4.2 Effect on Flame Shape . . . . .	19
2.1.4.3 Effect on Flame Structure . . . . .	19
2.2 CH PLIF Signal Modeling . . . . .	20
2.2.1 Basic Model . . . . .	21

2.2.1.1	Absorption Integral Calculation . . . . .	23
2.2.1.2	Population Distribution . . . . .	24
2.2.1.3	Solution . . . . .	25
2.2.2	CH PLIF Process . . . . .	26
2.2.3	Improved Model . . . . .	30
2.2.3.1	Absorption Integral Calculation . . . . .	34
2.2.3.2	Population Distribution . . . . .	35
2.2.3.3	Solution . . . . .	36
<b>3</b>	<b>Experimental Methods and Considerations</b>	<b>37</b>
3.1	LSB Configurations . . . . .	37
3.1.1	Configuration A . . . . .	38
3.1.1.1	Test Facility . . . . .	38
3.1.1.2	Low Swirl Burner . . . . .	41
3.1.2	Configuration B . . . . .	42
3.1.2.1	Test Facility . . . . .	42
3.1.2.2	Low Swirl Burner . . . . .	44
3.2	Diagnostics . . . . .	45
3.2.1	Laser Doppler Velocimetry . . . . .	45
3.2.2	CH* Chemiluminescence . . . . .	48
3.2.2.1	Image Processing . . . . .	48
3.2.3	CH Planar Laser-Induced Fluorescence . . . . .	51
3.2.3.1	Imaging System . . . . .	53
3.2.3.2	Laminar Flame Setup . . . . .	53
3.2.3.3	Laser Wavelength Calibration . . . . .	54
<b>4</b>	<b>CH PLIF Signal Modeling and Validation</b>	<b>57</b>
4.1	CH PLIF Preliminary Experiments . . . . .	57

4.1.1	Excitation Scan . . . . .	57
4.1.2	Linearity Test . . . . .	61
4.1.3	LIF Emission Spectrum . . . . .	64
4.2	Fluorescence Signal Modeling . . . . .	65
4.2.1	Fluorescence Yield . . . . .	66
4.2.2	Absorption Integral . . . . .	69
4.3	Chemkin modeling . . . . .	75
4.4	Results . . . . .	76
4.4.1	Unstrained Laminar Flames . . . . .	76
4.4.1.1	Methane-air flames . . . . .	76
4.4.1.2	Higher-order alkane flames . . . . .	81
4.4.1.3	Syngas flames . . . . .	85
4.4.2	Strained Flames . . . . .	86
4.5	Summary of Results . . . . .	87
<b>5</b>	<b>LSB Flame Characteristics</b>	<b>89</b>
5.1	Effect of Reference Velocity . . . . .	90
5.2	Effect of Preheat Temperature . . . . .	96
5.3	Effect of Swirl . . . . .	100
5.4	Effect of Equivalence Ratio . . . . .	103
5.5	Effect of Combustor Pressure . . . . .	108
5.6	Summary of Results . . . . .	111
<b>6</b>	<b>Conclusions</b>	<b>113</b>
<b>A</b>	<b>Seeder Design</b>	<b>114</b>
	<b>References</b>	<b>118</b>

# LIST OF FIGURES

2.1	Schematic of a vaned swirler . . . . .	12
2.2	Location of recirculation zones in the LSB flow field . . . . .	14
2.3	Schematic of LSB flame stabilization . . . . .	15
2.4	Borghi diagram . . . . .	20
2.5	Transitions in a basic two-level model for fluorescence . . . . .	21
2.6	CH $B^2\Sigma^- \leftarrow X^2\Pi$ (0,0) R-bandhead absorption lines . . . . .	27
2.7	Potential curves for electronic energy levels in the CH molecule . . . . .	29
2.8	Relevant transitions in a CH molecule . . . . .	31
2.9	Transitions in the improved CH fluorescence model . . . . .	32
3.1	Schematic of test facility A . . . . .	39
3.2	Detail schematic of configuration A . . . . .	41
3.3	Schematic of test facility B . . . . .	42
3.4	Detail schematic of configuration B . . . . .	44
3.5	Schematic of the LDV setup . . . . .	46
3.6	Sample CH* chemiluminescence data . . . . .	49
3.7	Schematic of the alexandrite laser . . . . .	51
3.8	Schematic of the laser calibration experiment . . . . .	54
3.9	Results of the laser calibration experiment . . . . .	55
4.1	Schematic of the excitation scan experiment . . . . .	58
4.2	Processing of the excitation scan images . . . . .	59
4.3	Results of the excitation scan experiment . . . . .	61
4.4	Schematic of the linearity experiment . . . . .	62
4.5	Results of the linearity experiment . . . . .	63

4.6	Spectrum of the CH LIF emission . . . . .	65
4.7	Validation of LIF signal model . . . . .	77
4.8	Comparison of GRI Mech 3.0 and San Diego mechanisms . . . . .	79
4.9	Methane flames - I . . . . .	80
4.10	Methane flames - II . . . . .	81
4.11	Methane flames - III . . . . .	82
4.12	C <sub>1</sub> -C <sub>3</sub> flames - I . . . . .	83
4.13	C <sub>1</sub> -C <sub>3</sub> flames - II . . . . .	84
4.14	C <sub>1</sub> -C <sub>3</sub> flames - III . . . . .	84
4.15	Syngas-alkane flames - I . . . . .	85
4.16	Syngas-alkane flames - II . . . . .	86
4.17	Strained flames . . . . .	87
5.1	Effect of reference velocity on the flame location and shape . . . . .	91
5.2	Effect of reference velocity on the flame structure . . . . .	92
5.3	Effect of temperature on the LSB flow field - I . . . . .	96
5.4	Effect of temperature on the LSB flow field - II . . . . .	97
5.5	Effect of swirl on the flame structure . . . . .	101
5.6	Effect of equivalence ratio on the flame shape - I . . . . .	104
5.7	Effect of equivalence ratio on the flame shape - II . . . . .	105
5.8	Effect of equivalence ratio on the flame structure . . . . .	106
5.9	Effect of combustor pressure on the flame location and shape . . . . .	109
A.1	Schematic of the old seeder design . . . . .	115
A.2	Schematic of the new seeder design . . . . .	116

# LIST OF TABLES

3.1	Swirler dimensions . . . . .	38
4.1	CH emission coefficients . . . . .	66
4.2	CH quenching cross-sections . . . . .	67
4.3	Spectroscopic constants for the CH $X^2\Pi$ state . . . . .	70
4.4	Absorption lines and coefficients for the $B^2\Sigma^- \leftarrow X^2\Pi$ (0,0) R branch	71
5.1	Test conditions for studying reference velocity effects . . . . .	90
5.2	Test conditions for studying preheat temperature effects . . . . .	95
5.3	Test conditions for studying swirl effects . . . . .	100
5.4	Test conditions for studying equivalence ratio effects . . . . .	103
5.5	Test conditions for studying pressure effects . . . . .	108

## LIST OF SYMBOLS

$X_f$  Flame standoff distance



## SUMMARY

# CHAPTER 1

## INTRODUCTION

The need to reduce pollutant emissions, particularly the oxides of nitrogen,  $\text{NO}_x$ , is driven by increasing ecological awareness and stringent government regulations. This spurs efforts in the gas turbine industry to seek cleaner, more environment-friendly combustion concepts. Several mechanisms have been identified to explain the production of  $\text{NO}_x$  in hydrocarbon-air combustion systems. Of these, the thermal  $\text{NO}_x$  mechanism discovered by Zel'dovich, is a prominent source of  $\text{NO}_x$  production at the high temperature conditions encountered in typical combustors. The amount of thermal  $\text{NO}_x$  produced scales exponentially with the adiabatic flame temperature.

Efforts to reduce the flame temperature have led low  $\text{NO}_x$  gas turbine manufacturers to adopt one of two options—Lean Premixed (LP) operation, or Rich-Quench-Lean (RQL) operation. Of these, ground-based gas turbines used in power generation have tended to favor LP operation as it is conceptually simpler and avoids issues resulting from inhomogeneous mixing of fuel and air. Further, the ultra-lean operating conditions reduce flame temperature and minimize  $\text{NO}_x$  production.

In practice, 1800 K is considered a limiting value for the flame temperature, ensuring that the thermal  $\text{NO}_x$  production is constrained to a minimum.<sup>[1]</sup> Operating a combustor at such lean conditions results in weaker combustion processes that are highly susceptible to perturbations and results in combustor instabilities or even flame blow off. This highlights the requirement for robust flame stabilization techniques that can sustain combustion at ultra-lean conditions. In their most basic form, flame stabilization techniques work by making the local reactant velocity and the local flame speed equal. In the context of lean flames, the risk is of the slowly propagating flames to be blown off by the high velocity reactant stream. Consequently, flame

stabilization in gas turbine combustion is brought about either by reducing the local  
reactant velocity (e.g. by using bluff body flame holders), by boosting the local flame  
velocity (e.g. by enhancing product recirculation), or by providing continual ignition  
to the flame (e.g. by using pilot flames).

Swirl-stabilized combustion is a widely used flame stabilization technique in gas  
turbine applications.[2,3] It primarily functions by inducing recirculation zones in  
the flow field that transport heat and radicals from the products into the reactants.  
This enhances the flame propagation velocity by increasing reaction rates within the  
flame, resulting in robust flame stabilization. However, the recirculation zones are  
associated with high peak residence times for hot combustion products and are sites of  
thermal  $\text{NO}_x$  production in the combustor. Nevertheless, swirl-stabilized combustors  
are ubiquitously employed today in land-based gas turbines used for power generation.

More recent research[4] on the Low Swirl Burner (LSB) has identified a potential  
solution for this problem. The LSB anchors a lifted flame, reducing the need for high  
swirl in the flow field. The lifted, V-shaped flame is stabilized by aerodynamic means  
which allows for robust operation even at low equivalence ratios. This weakens the  
recirculation zones and eliminates pockets of high residence times, resulting in the  
potential for significantly reduced  $\text{NO}_x$  emissions compared to a similar high-swirl  
design.

## 1.1 Motivation

By comparison to atmospheric pressure experiments, high pressure experimental test-  
ing of combustion systems is fraught with difficulties. This is reflected in the com-  
paratively smaller subset of publications that report experimental results from high  
pressure tests. The primary source of these difficulties stems from the need for com-  
plicated testing facilities to reach and maintain high pressures. The inherently limited  
access afforded by pressure vessels makes intrusive methods of data gathering nearly

impossible. As a result, any need for spatially resolved data other than temperature  
and pressure measurements has to be met by optical diagnostics.

In the context of LSB research, these difficulties have confined much of the published experimental results to ambient conditions. The eventual application of this technology in gas turbine engines requires high quality data acquired at high pressure conditions. Ideally, such data will map the velocity field and heat release in the LSB and study their variation with flow conditions. Since the LSB relies on the velocity field to stabilize its flame, its flame characteristics hold information pertinent to both the velocity field and the heat release distribution within the combustor. This allows a passive diagnostic such as recording the flame chemiluminescence to be used even at high pressure conditions to observe and record usable data about the LSB flame characteristics. Such data, acquired at conditions closer to real world gas turbine combustor operating conditions is of particular interest to the gas turbine industry as it can be used for designing better, more robust combustors with low  $\text{NO}_x$  emissions.

The primary flame characteristic of interest is the flame standoff distance, defined as the distance from the flame stabilization point to the inlet of the LSB. This metric is useful in gauging the stability of the flame and the need for control systems to closely monitor its tendency to flashback or blow-off. The standoff distance also relates to the heat load experienced by the injector and consequently affects how often the mechanical components of the LSB will require to be replaced in operation. Finally, a systemic variation in the location of the flame over a range of flow parameters may indicate potential problems operating the combustor at previously untested conditions.

Quantifying the shape of the flame can complement the information gleaned from the flame standoff measurements. In case of the V-shaped LSB flame, this can be conveniently obtained by measuring the angle of the flame cone. Changes in the flame angle affect the length of the flame, which is a design consideration for sizing LSB

combustors in gas turbines.

The profile of the flame chemiluminescence along the length of the combustion zone is representative of the local heat release at those locations. A uniform heat release profile is preferred so as to avoid thermally stressing the combustor at the hot spots. Further, since  $\text{NO}_x$  production rates are so strongly dependent on temperature, the heat release profile can help forecast emissions performance issues of the combustor, particularly when augmented by knowledge of the local flow velocity (and hence, residence time). Finally, the heat release map could be incorporated into  $n$ - $\tau$  models to predict the onset of thermo-acoustic instabilities in the combustor.

The primary goal of this research work is to study the flame characteristics of the LSB, such as its location and shape, as a means to learn more about the combustor operation at high pressure conditions.

In case of lean hydrocarbon flames, the primary sources of flame chemiluminescence are  $\text{OH}^*$  ( $A^2\Sigma^+ \rightarrow X^2\Pi$  bands, 310 nm),  $\text{CH}^*$  ( $A^2\Delta \rightarrow X^2\Pi$  bands, 430 nm,  $B^2\Sigma^- \rightarrow X^2\Pi$  bands, 390 nm),  $\text{C}_2^*$  ( $d^3\Pi \rightarrow a^3\Pi$  Swan bands, 470 nm, 550 nm) and the  $\text{CO}_2^*$  (band continuum, 320–500 nm). Of these,  $\text{CH}^*$  chemiluminescence has several advantages that make it suitable for this particular study. First, collection of  $\text{CH}^*$  chemiluminescence is less affected by blackbody radiation from the walls of the combustor, compared to longer wavelength emissions from a species like  $\text{C}_2^*$ . Its narrow bandwidth allows one to use a bandpass filter to collect signals from only the wavelengths of interest, further minimizing interference from other light sources. Using such a narrow bandpass filter for a broad band emitter like  $\text{CO}_2^*$  would result in rejecting most of the available signal.  $\text{CH}^*$  chemiluminescence occurs in the visible wavelengths and does not require expensive UV lenses or imaging systems with high quantum efficiencies in UV to record it—as would be needed to image  $\text{OH}^*$  chemiluminescence, for instance. In typical LSB operation, where the flame is not expected to operate near extinction,  $\text{CH}^*$  chemiluminescence can serve as a reliable indicator

of heat release in the combustor. For all these reasons,  $\text{CH}^*$  chemiluminescence is a suitable technique to image the LSB flame.

Ultimately, the amount of information that can be gathered by imaging the flame chemiluminescence is limited by its spatial resolution. Since chemiluminescence imaging is integrated over the line of sight, studying the flame brush or the flame structure is beyond its capabilities. A planar imaging technique such as Planar Laser-Induced Fluorescence (PLIF) is better suited for such applications.

In hydrocarbon flames, species accessible to PLIF are generally minor species in the flame. PLIF studies of hydrocarbon flames have hitherto focused on the hydroxyl, OH, radical. However, OH is produced in the flame zone and destroyed by relatively slow three-body reactions, causing it to persist and be transported away from the flame and into the product zone.[5] As a result, it does not serve as a direct marker of the flame front. Instead, the location of the flame is inferred from the sharp gradient in the OH signal as the reactants are converted into products.

The persistence of OH in the products makes OH PLIF somewhat less suited to studying flames in flows with high product recirculation. In such flows, the presence of OH in both the reactants and the products weakens the gradient at the flame. Further, since OH radicals could be transported transverse to the flame, its presence or absence serves as an unreliable indicator of local flame extinctions. Nevertheless, researchers have been able to use OH PLIF successfully[6, 7] to study such flames, particularly when the images are enhanced by nonlinear filtering techniques.[8, 9]

This study utilizes CH PLIF as the flame visualization technique. CH is produced and destroyed rapidly by fast two-body reactions, confining it to the thin heat release zone of the flame. This makes it suitable for use as a marker species for the flame front.[10] CH is formed during the breakup of hydrocarbon fuel molecules[11] and is also known to play an important role in the production of prompt  $\text{NO}_x$ . [12] Hence, it is a minor species of considerable importance to combustion research. This leads us

to the second motivation for this study—to examine the use of CH PLIF as a flame  
imaging technique in combustion systems and further, to use it to image and study  
the LSB flame.

The use of CH PLIF to study lean hydrocarbon flames has been difficult in the past  
due to several issues. First, the concentration of the CH species in hydrocarbon flames  
rapidly declines with equivalence ratio, making high quality imaging of the flame front  
at lean conditions challenging. Further, the implementation techniques in the past  
have suffered from a host of problems ranging from elastic scattering interference  
to saturation issues leading to diminished signal-to-noise ratios. However, a recent  
implementation by Li et al.[13] has managed to overcome these issues and has been  
demonstrated to image moderately lean flames with good fidelity.

Recent studies[14] have indicated that the formyl species HCO is a superior indi-  
cator of heat release in hydrocarbon flames when compared to CH or OH. The HCO  
LIF signal has been demonstrated to correlate well with the heat release rate, with  
little dependence on equivalence ratio or strain rate. The last factor, in particular, has  
been shown to quench the CH PLIF signal[15] in highly strained flames, even when  
the flame itself is not extinguished. Unfortunately, the signal levels from HCO LIF  
are very poor[14, 16] and are unsuitable for single-shot investigation of hydrocarbon  
flames. To overcome this, one study[16] proposed a simultaneous LIF investigation of  
formaldehyde,  $\text{CH}_2\text{O}$ , and OH with the reasoning that the formation rate of HCO is  
governed directly by the product of the concentration of these two intermediates. This  
method has been used in a number of investigations,[17] despite being experimentally  
cumbersome. A more recent implementation[18], published after the initiation of  
the present effort, has demonstrated single-shot HCO PLIF with moderate signal-to-  
noise ratios by utilizing a novel excitation scheme. Follow up studies applying this  
technique in other hydrocarbon flames are awaited.

## 1.2 Literature Review

159

### 1.2.1 Low Swirl Burner

160

The LSB is a relatively new combustion technology and as such has a brief history. 161  
Initial interest in low swirl combustion was primarily motivated by its ability to sta- 162  
bilize a freely propagating turbulent flame.[19] As a result, initial designs of the LSB 163  
(which at the time used tangential jets to produce swirl) were pursued by Bédard and 164  
Cheng[4, 20] as test beds for studying 1-D, planar turbulent flames. Several subse- 165  
quent studies[21–27] utilized this behavior and investigated fundamental turbulent 166  
flame structure and propagation in the jet LSB. Simultaneously, the discovery of its 167  
ability to achieve low  $\text{NO}_x$  emissions prompted interest in commercial applications of 168  
the LSB, such as in industrial furnaces and boilers.[28–30] 169

The current form of the LSB (as used in this thesis) using vanes to generate swirl 170  
was originally modified from a typical production swirl injector used in gas turbine 171  
combustors. The results of testing this new design were published by Johnson et 172  
al.[31] The design elements of the new injector—now called the Low Swirl Injector 173  
(LSI)—were tuned in an atmospheric pressure test rig using LBO and flame location 174  
as the criteria. The atmospheric tests were conducted with preheated reactants at 175  
up to 650 K. The more interesting results from the work came from high pressure, 176  
high preheat tests (15 atm, 700 K) in a test rig with limited optical access. The 177  
researchers measured a dramatic (50%) reduction in the  $\text{NO}_x$  emissions by switching 178  
from the original (“High” Swirl Injector) to the new low swirl design. The emissions 179  
performance was also noted by Nazeer et al.[32] 180

Subsequent studies by Cheng et al.[33,34] explored the characteristic velocity field 181  
in the LSB using PIV and discovered self-similar behavior that implied that the flame 182  
location was unaffected by the mass flow rate of the reactants. This led to further 183  
insights into the flame stabilization mechanism used by the LSB. These results will 184



be revisited in Chapter 2 in greater detail.

The effects of using an enclosure to contain the combustion zone were explored by Cheng et al.[35] who found scaling criteria for minimizing the effect of the enclosure on the flame stabilization location. More recent work has tended to focus on the use of various fuels such as hydrogen mixtures[36] with and without dilution[37], landfill gas[34, 38] and syngas[39].

Relatively little research has focused on the flame location and other characteristics and studied their variation at gas turbine relevant conditions. Plessing et al.[21] and Petersson et al.[40] have presented planar images of the LSB flame, but have been confined working with non-preheated, atmospheric flames at low flow rates. Of these, Plessing et al. used a jet-LSB design and imaged the resulting flame with OH Laser-Induced Predissociative Fluorescence to calculate turbulent burning velocities. Petersson et al. studied a vane-LSB design that is slightly modified from the one tested by Cheng and co-workers and used a bevy of techniques, including OH PLIF to study the turbulent flame. The OH PLIF images were used to extract mean reaction progress variable contours for comparison to and validation of LES models. Although their test conditions and burner geometry were different, their results were consistent with the ones published by Cheng et al. These are notable for being some of the few works that afford us a look at the flame structure in the LSB with good spatial resolution.

### 1.2.2 CH PLIF Implementations

Historically, CH was the first species to be detected using LIF in a flame.[41] Early attempts[42, 43] to excite the CH layer used variations of short-pulsed, YAG-pumped dye laser output targeting transitions in one branch of the  $A^2\Delta \leftarrow X^2\Pi$  (0,0) band and observing resulting fluorescence in the same band, but at a different rotational branch. These methods relied on the strong absorption of the  $A-X$  bands to generate

high signal values, but suffered from interference from elastic scattering. Further, the short pulsewidth and narrow spectral bandwidths of the excitation sources quickly saturated the transition being pumped, limiting the amount of LIF signal measured.

Namazian et al.[44] and Schefer et al.[45] had better success at overcoming interference issues by exciting the  $A - X$  (0,0) band, but observing fluorescence from the (0,1) band. Another similarly non-resonant technique was proposed by Paul et al.[46] who excited the  $A^2\Delta \leftarrow X^2\Pi$  (1,0) band and observed resulting fluorescence from the (1,1) and (0,0) bands. These approaches provide good separation between the excitation and emission wavelengths, but are hampered by the spectroscopic properties of the CH system—which will be explored further in Section 2.2.2—which disfavor radiative transitions in the non-diagonal (0,1) or (1,0) bands. Further, Namazian et al.’s scheme suffers from interference due to Raman scattering of the excitation beam by the fuel species, which overlaps the (0,1) band fluorescence.

Carter and several others[47–55] pumped the  $B^2\Sigma^- \leftarrow X^2\Pi$  (0,0) band and utilized fast electronic transfer from the  $B^2\Sigma^-$ ,  $v = 0$  to populate the  $A^2\Delta$ ,  $v = 0, 1$  levels. This way, they could observe the strong emission from  $A^2\Delta \rightarrow X^2\Pi$  (1,1) and (0,0) bands. This method overcame the interference issues by providing sufficient spacing between the excitation and emission wavelengths, but suffered from saturation issues due to the short pulsewidth of the excitation sources. Further, at high laser irradiance, the group recorded noticeable interference from fuel LIF.

Li et al.[13, 56, 57] investigated the use of an alexandrite laser[58] to improve upon the previous excitation scheme by targeting the R-bandhead of the  $B^2\Sigma^- \leftarrow X^2\Pi$  (0,0) transition with an excitation beam having a much longer pulse duration than Nd:YAG pumped dye lasers. This excitation scheme offers several advantages over previous implementations. First, it inherits the large spacing between the excitation and emission wavelengths and reduced interference issues from Carter et al.’s implementation. Next, by using a long pulsed laser beam, it overcomes saturation issues.

In fact, the researchers note that the pulsewidth is long enough to allow the same CH molecule to go through the excitation-deexcitation sequence several times, boosting signal output. This aspect of the implementation is further enhanced if the laser is operated in multimode, with a large spectral bandwidth, allowing the laser to target several lines near the R-bandhead. The resultant improvement in signal-to-noise makes this technique suitable to study even low equivalence ratio hydrocarbon flames. This is the excitation scheme that is used in this study.

### 1.3 Objectives and Overview

To summarize, this thesis aims to investigate the behavior of the LSB flame at gas turbine-like conditions by studying its characteristics and quantifying their dependence on various flow and geometric parameters. Flame characteristics of interest to this study include the flame location, shape and structure. The investigated parameters are combustor pressure, preheat temperature, reference velocity, equivalence ratio and the swirler vane angle. Studying the effect of these parameters on the LSB flame will allow us to reexamine atmospheric pressure/low preheat models of LSB flame stabilization at conditions more relevant to gas turbine operation. Further, investigating the sensitivity of the flame characteristics to flow and geometric parameters will extend our understanding of the physical processes responsible for LSB flame stabilization. The results will also aid in designing more robust LSB configurations for use in future gas turbine engines.

Parallel to this, the current work will detail the development of a CH PLIF imaging system to study the structure of lean hydrocarbon flames in preheated combustors. As a planar imaging technique, this will improve significantly on the spatial and temporal resolution capabilities of other flame imaging techniques like chemiluminescence imaging. The imaging system will be demonstrated on a laminar flame setup, as well as on the LSB. The intensity of the CH LIF signal will be modeled to predict its vari-

ation with pressure, temperature, and reactant composition. While the thesis retains 264  
its focus on methane-air combustion, mixtures of alkanes and syngases will also be 265  
examined by the model for the feasibility of studying the flame with CH PLIF. 266

The first half of Chapter 2 provides a brief background discussing previously re- 267  
ported results from LSB investigations conducted by other researchers. The second 268  
half of the chapter discusses the CH PLIF process and explores simple and complex 269  
models for CH PLIF intensity. Details of the experimental facility and apparatus 270  
used to study the LSB and develop the CH PLIF imaging system are presented in 271  
Chapter 3. Chapter 4 presents the results and validation of the CH PLIF signal 272  
models developed in this thesis. Chapter 5 presents results and discussion of the flame 273  
characteristics of the LSB acquired at high pressure conditions, along with flame 274  
structure images acquired at atmospheric conditions using CH PLIF. Finally, conclu- 275  
sions drawn from the discussions in Chapters 4–5 and suggestions for future work are 276  
presented in Chapter 6. 277

## CHAPTER 2

278

## BACKGROUND

279

This is a two-part chapter. The first section focuses on the LSB and discusses the current understanding of factors affecting the LSB reacting flow field. The second section explores efforts to model the CH PLIF signal intensity as a function of local composition and thermodynamic conditions in a flame.

### 2.1 LSB Reacting Flow Field

284

This section describes the salient features of the LSB flow field that will play an important part in the discussions to follow in this thesis. As discussed in Section 1.2.1, there have been multiple variations of the LSB design used by researchers in the past. Broadly, they can be classified into jet-LSB and vane-LSB, based on the means used to produce the weak swirl in the flow field. This thesis, and thus the following background material, focuses on the vane-LSB design.

The vane-LSB—or simply *LSB* from here on—uses a vaned swirler with a central

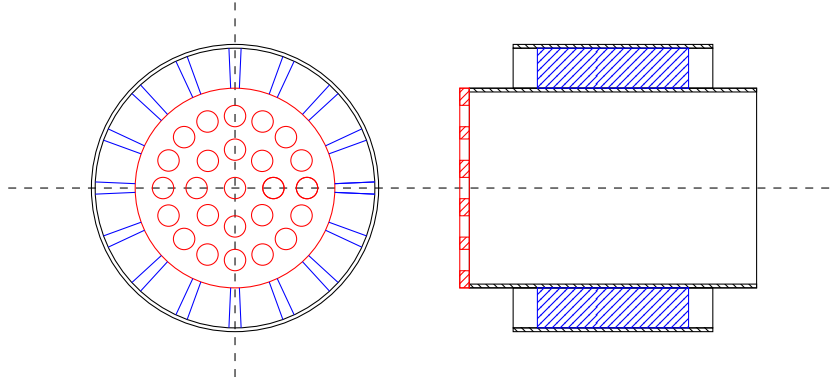


Figure 2.1: The figure shows a bottom and side cross-sectional view of the vaned swirler design used in this study. The perforated plate used to control the relative mass flow split is highlighted in red, while the vanes used to generate swirl are highlighted in blue.

open section. A typical design of such a swirler is shown in Figure 2.1. The swirler splits the flow into two streams, imparting swirl only to the outer annular flow. A perforated plate covers the open central section of the swirler and controls the relative mass flow split between the central unswirled flow and the annular swirling flow. The swirled flow and the central flow are allowed to mix after passing the swirler in a constant area nozzle. The length of this constant area nozzle is called the swirler recess length and is typically about one or two swirler (outer) diameters. The flow leaves the constant area nozzle and abruptly expands into the combustion zone.

### 2.1.1 Role of swirl and recirculation zones

The amount of swirl present in the resulting flow is characterized by a theoretical swirl number,  $S$ , which represents the ratio of angular momentum to axial momentum in the flow field. Cheng et al.[29] and later, Littlejohn et al.[30] reduced this to the following equation.

$$S = \frac{2}{3} \tan \alpha \frac{1 - R^3}{1 - R^2 + \left[ M^2 \left( \frac{1}{R^2} - 1 \right)^2 \right] R^2} \quad (2.1)$$

In Equation 2.1,  $R$  is the ratio of the diameter of the central section to the outer diameter of the swirler. Similarly,  $M$  is the ratio of the mass flow rate through the central portion to the mass flow rate through the outer (vaned) portion of the swirler. Finally,  $\alpha$  is the angle of the vanes of the swirler.

Along with the recess length of the swirler, the theoretical swirl number was identified to be a key parameter that determines the LSB operating regime.[30] Typical values of  $S$  in low swirl combustion range from 0.4–0.6.

Figure 2.2 shows the locations of the notable recirculation zones in the LSB flow field. The toroidal recirculation zone (TRZ) forms near the inlet, while the central recirculation zone (CRZ) forms within a recirculation bubble along the centerline. In

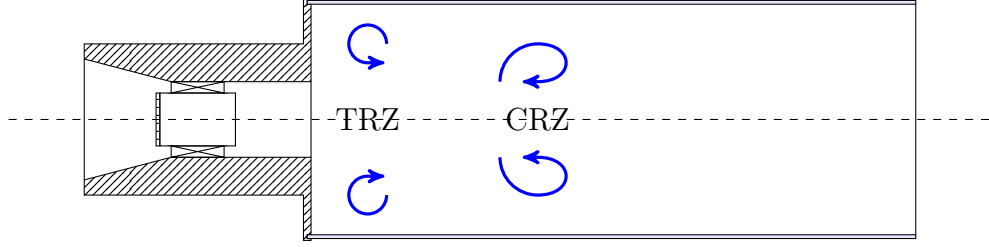


Figure 2.2: The figure shows the locations of the recirculation zones in the LSB flow field. The Toroidal Recirculation Zone (TRZ) forms near the abrupt area expansion. The Central Recirculation Zone (CRZ) forms within a recirculation bubble along the centerline of the combustor.

conventional swirl combustion, the function of the swirl is to induce these recirculation zones that help stabilize the flame by causing a feedback of heat and radicals from the products into the reactants. In particular, the toroidal recirculation zone traps hot combustion products and continually ignites the reactants at the base of the flame.[\[31\]](#)

In the LSB flow field, these recirculation zones are not only much weaker, but also, are not intended to play any part in the stabilization of the flame. Instead, the LSB flame is a freely propagating turbulent flame that is stabilized by the divergent flow coming from the inlet nozzle. The function of the swirl in the LSB flow field is merely to enhance this divergence. This purely aerodynamic means of stabilizing the flame differentiates the LSB regime from conventional swirl combustion.

### 2.1.2 Axial velocity profile and self-similarity

The mean axial velocity profile along the centerline of the LSB has been found[\[33,34\]](#) to exhibit a characteristic linear profile in the near field of the inlet. Two parameters can be used to characterize this linear profile. First, extrapolating the velocity profile to the point upstream where the axial velocity equals the reference velocity, one can obtain the location of the virtual origin. The virtual origin represents the point upstream from which the divergence seemingly originates. The second parameter is the axial stretch rate, which is the slope of the linear region of the axial velocity profile.

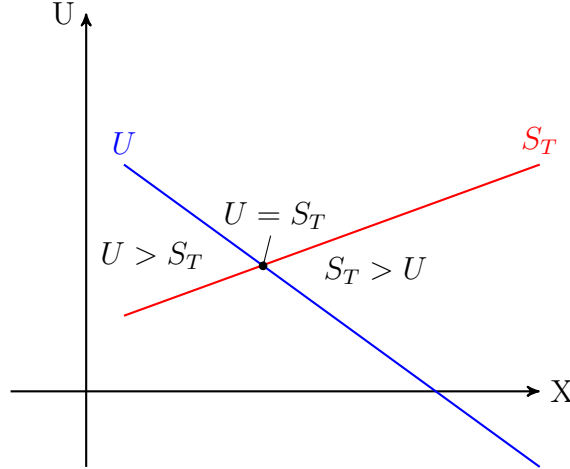


Figure 2.3: The figure above illustrates the robustness of the LSB flame stabilization mechanism. The flame is stabilized at the point where the reactant velocity,  $U$ , and the turbulent flame speed,  $S_T$ , are equal. Perturbations to the flame standoff distance to the left or the right are counteracted by either  $U$  or  $S_T$  respectively making this a stable equilibrium.

Cheng et al.[33,34] investigated these two parameters using a non-preheated setup at atmospheric pressure. They found that the virtual origin for reacting LSB flow fields asymptotically translates upstream at low/moderate Reynolds numbers, while the mean axial stretch rate, when normalized by the reference velocity, is nearly independent of the same parameter. This means that at moderately increasing Reynolds numbers, the divergent flow structure shifts upstream into the injector. This upstream shift ceases for high Reynolds numbers (above 70,000).

Since this shift does not affect the slope of the velocity profile, the researchers plotted the mean axial velocity profiles for different operating conditions, shifted to have a common virtual origin. Further, the velocity profiles were normalized by the mass-averaged inlet velocity (called the reference velocity). The resultant plot showed that the linear section of the divergent flow was self-similar at all the velocities tested. This self-similarity of the mean axial velocity profile was used to explain other observations regarding the flame characteristics, as described in the following sections.



### 2.1.3 Flame stabilization mechanism

The flame stabilization mechanism in the LSB is purely aerodynamic. The turbulent flame is not anchored in the sense of an attached flame, but freely propagates into the reactants. Conventionally, attached flames are preferred in combustion systems as lifted flames are associated with unstable/undesirable characteristics like blow off. However, previous studies[31] indicate the LSB flame is robustly stabilized and not prone to blow off.

The location where the LSB flame is stabilized is found from the equilibrium condition for flame stabilization—the local reactant velocity,  $U$  equals the local turbulent flame propagation velocity,  $S_T$ . In the LSB, the decrease in the local reactant velocity along the centerline of the combustor is accompanied by an increase in the local turbulence level. In other words, along the axis of the combustor, at the location where the flame is stabilized, the reactant velocity is decreasing, while the turbulent flame propagation velocity (which scales with the local turbulence) is increasing.

This sets up a stable equilibrium for the flame as shown in Figure 2.3. Small perturbations causing the flame to move upstream are offset by the increased reactant velocity, while similar perturbations downstream are counteracted by the increased turbulent flame speed. This is the mechanism behind the robust stabilization of the LSB flame.

### 2.1.4 Effect of Flow Parameters on Flame Characteristics

The operating conditions of the LSB combustor are fully described by four fundamental flow parameters; the combustor pressure,  $p$ , the combustor temperature,  $T$ , the mixture equivalence ratio,  $\phi$ , and the reference velocity,  $U_0$ . The reference velocity represents the mass-averaged velocity of the reactants entering the LSB and is defined after Cheng et al.[29] as a function of several variables such as the mass flow rates of the air and fuel,  $\dot{m}$ , their densities at the swirler,  $\rho$  and the area of the swirler

calculated from its outer diameter,  $d_s$ .

374

$$U_0 = \frac{\left(\frac{\dot{m}_{air}}{\rho_{air}}\right) + \left(\frac{\dot{m}_{fuel}}{\rho_{fuel}}\right)}{\frac{\pi d_s^2}{4}} \quad (2.2)$$

In this section, we will briefly discuss the effect of flow parameters have on the flame characteristics of interest. By way of an example, and as a means to introduce a few basic concepts, the following discussion will examine the effect of increasing the reference velocity on the flame location, shape and structure. In-depth discussion of the dependence of each flame characteristic on all the flow parameters of interest will be deferred till Chapter 5.

375  
376  
377  
378  
379  
380

#### 2.1.4.1 Effect on Flame Standoff Distance

381

As described earlier in Section 2.1.3, the LSB flame is stabilized where the local reactant velocity and turbulent flame speed are equal.

382  
383

Unlike the laminar flame speed,  $S_L$ , the turbulent flame speed is not uniquely determined by the reactant composition and thermodynamic conditions. Instead, it is a function of the flow characteristics and the burner geometry.

384  
385  
386

A simple model proposed by Damköhler[59] treats the turbulent flame as a wrinkled laminar flame. The presence of these wrinkles vastly increases the surface area of the flame, increasing the rate at which the reactants can be consumed through the flame. The size of these wrinkles can be related to the rms of the local reactant velocity,  $u'$ . Expressed mathematically, this leads to Equation 2.3.

387  
388  
389  
390  
391

$$\frac{S_T}{S_L} = 1 + \frac{u'}{S_L} \quad (2.3)$$

Cheng et al.[23, 38, 39] observed that the slope of this linear relationship was dependent on the fuel mixture being used. This idea is encapsulated in Equation 2.4

392  
393

that presents a modified version of Equation 2.3.

394

$$\frac{S_T}{S_L} = 1 + K \frac{u'}{S_L} \quad (2.4)$$

The constant  $K$  has a value of around 1.73 for methane-air mixtures and a somewhat higher value—3.15—for hydrogen-air mixtures,[38] suggesting that the turbulent flame speed is affected strongly by the thermo-diffusive properties of the fuel.

395

396

397

In order to predict the expected effect of increasing the reference velocity, consider the following analysis at the flame standoff location where  $U=S_T$ .

398

399

$$\begin{aligned} \frac{S_T}{S_L} &= 1 + K \frac{u'}{S_L} \\ S_T &= S_L + K u' \\ \implies U &= S_L + K u' \\ U_0 - \frac{dU}{dx}(X_f - X_0) &= S_L + K u' \\ \therefore X_f &= X_0 + \frac{1 - \left( \frac{S_L}{U_0} + K \frac{u'}{U_0} \right)}{\frac{1}{U_0} \frac{dU}{dx}} \end{aligned} \quad (2.5)$$

Consider the terms on the RHS of Equation 2.5. As described in Section 2.1.2, the virtual origin location is invariant for moderate to high values of reference velocity. In the same section, the normalized slope of the velocity profile,  $\frac{1}{U_0} \frac{dU}{dx}$ , was also noted as being invariant with reference velocity. In the numerator of the second term, the local turbulence intensity,  $\frac{u'}{U_0}$ , can also be expected to be a constant, since  $u'$  should scale with the reference velocity in the same manner as long as the burner geometry does not change. The turbulence intensity,  $\frac{u'}{U_0}$  in the LSB increases from the inlet along the centerline reaching values on the order of 0.1–1.0 near the flame standoff location.[34] That leaves only the term  $\frac{S_L}{U_0}$  as a function of  $U_0$ . Typically, the laminar

400

401

402

403

404

405

406

407

408

flame speeds are at least an order of magnitude, if not more, lower ( $\approx O(1)$  m/s) 409  
than the reference velocities at which the LSBs are operated ( $\approx O(10)$  m/s). As a 410  
result, variations in this term are a vanishingly small portion of the sum, leaving the 411  
entire RHS independent of  $U_0$ . In other words, the flame location,  $X_f$  is expected to 412  
be invariant with the reference velocity at which the LSB is operated. 413

#### 2.1.4.2 Effect on Flame Shape 414

Now, consider the effect of increasing the reference velocity on the angle of the flame 415  
cone. Again, the stabilization condition is equality between the local velocity and 416  
the turbulent flame speed. However, along the flame cone, the reactant velocities are 417  
much higher and the flame propagation can only occur at an angle to the reactant 418  
velocity. Increasing the reference velocity does not affect any of these factors and thus, 419  
the flame angle can also be expected to be unchanged at higher reference velocities. 420

#### 2.1.4.3 Effect on Flame Structure 421

Finally, the effect of the reference velocity on the structure of the turbulent flame 422  
should be considered. Depending on the characteristics of the flame structure, the 423  
operation point can be placed on a Borghi diagram, as shown in Figure 2.4. The 424  
Borghi diagram[60] is a phase diagram used to classify and delineate regimes of pre- 425  
mixed turbulent combustion. The double-log plot is drawn using properties of the 426  
reacting mixture and its turbulence-related quantities. It is partitioned into various 427  
regimes by different straight lines representing the locus of non-dimensional parame- 428  
ters. It is useful to examine the effect of various parameters on the flame structure 429  
by examining the tendency of the operating point to shift on the Borghi diagram. 430

Several versions of the Borghi diagram exist that use different variables to plot 431  
the combustion regimes. In the current study, we use a diagram based on  $\frac{u'}{S_L}$  and  $\frac{L}{\delta_f}$ . 432  
The key parameters to be considered here are the rms velocity,  $u'$ , the laminar flame 433

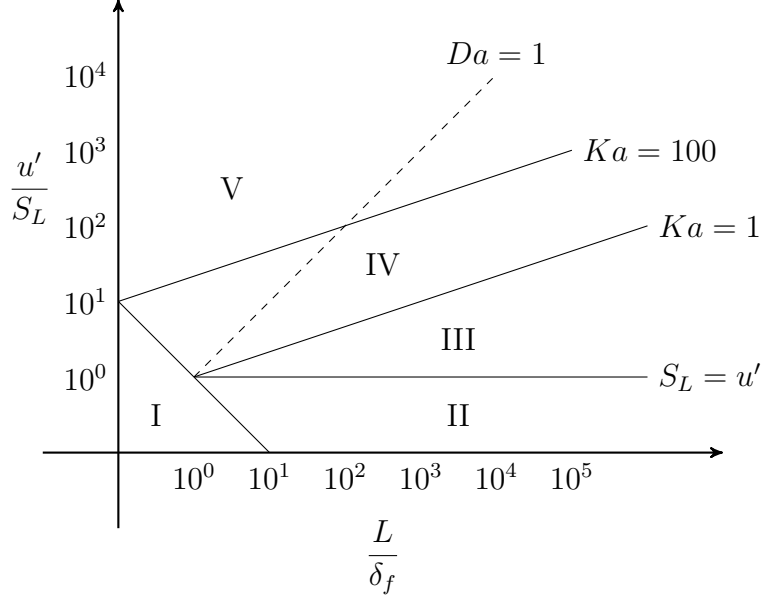


Figure 2.4: The figure shows the Borghi diagram marking the various regimes of premixed turbulent combustion—I. laminar flames, II. wrinkled flamelets, III. corrugated flamelets, IV. thin flame zones, and V. broken reaction zones—separated by contours of Karlovitz number.

speed,  $S_L$ , the integral length scale of the flow,  $L$ , and the flame thickness,  $\delta_f$ .

Increasing the reference velocity will be accompanied with a concomitant increase in the level of turbulence in the flow, but it changes none of the other parameters. As a result, the operating point will traverse vertically on the Borghi diagram. If the LSB operates in the wrinkled flamelets regime to begin with, at very high reference velocities, it may be expected to cross over into the corrugated flamelets regime. This will be marked by the formation of holes and pockets in the flame sheet.

## 2.2 CH PLIF Signal Modeling

While the intent and scope of this work is to use CH PLIF as a visualization technique to image the flame front with high fidelity, it would be extremely useful to be able to predict the CH PLIF signal intensity for different reactant mixtures and initial conditions as a means to gauge the feasibility of applying the technique to acquire high fidelity images of the flame at those conditions. To that end, this discussion

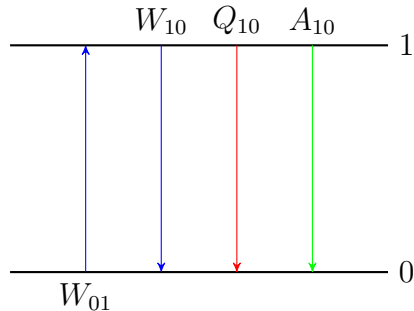


Figure 2.5: The figure shows energy levels and transitions between two levels, labeled 0 and 1, in a basic model of laser-induced fluorescence. Stimulated absorption and emission are shown in *blue*, collisional quenching is shown in *red* and spontaneous emission is shown in *green*.

will attempt to develop a mathematical model to calculate, in a semi-quantitative 447  
manner, the rate of CH PLIF photons emitted by the illuminated reaction zone. The 448  
following discussion introduces important concepts in LIF signal intensity calculation 449  
using a simple two-level model and then proceeds to apply these concepts to model 450  
the more complicated physical processes in the CH system. 451

### 2.2.1 Basic Model 452

In its most basic form, the rate at which fluorescence photons are generated in a 453  
system,  $\Phi$  is the product of the number of emitters,  $N$  and the Einstein coefficient 454  
for spontaneous emission,  $A$ . 455

$$\Phi = N \times A \quad (2.6)$$

The fluorescence photons produced are radiated in all directions and only a frac- 456  
tion of these can be recorded by a collection system in an experiment. This fraction 457  
is determined by the experimental set up, the collection angle, and the efficiency of 458  
the optics and the detector used to record the signal. For this analysis, however, this 459  
fraction is omitted to reduce complexity. 460

In a simple two-level model for the fluorescing system, as shown in Figure 2.5, 461

Equation 2.6 may be expanded in terms of the number density of the emitters,  $n$ , and the volume in which the fluorescence occurs,  $V$ .

$$\Phi = n_1 V A_{10} \quad (2.7)$$

The population of the upper state,  $n_1$  can be solved for by rate analysis. The mathematical treatment is not particularly complicated and is covered in detail by various textbooks and review papers.[61, 62] Here, we shall merely remark that the functional form of the solution has two limiting cases. The limits are decided by the relative magnitudes of the pumping rate,  $W_{01}$ , which depends on the laser intensity and the radiative transition probability, and the relaxation rate in the absence of an external field, which is given by the sum of the spontaneous emission and collisional quenching rate,  $A_{10} + Q_{10}$ . The pumping rate is the rate at which the upper energy level is populated through stimulated absorption from the lower level. The relaxation of the molecules to the lower energy state occurs either through spontaneous emission of a photon or energy transfer to other molecules through inelastic collisions.

When the pumping rate is far lower compared to the relaxation processes ( $W_{01} \ll A_{10} + Q_{10}$ ), the solution tends to the weak excitation limit. In this limit, the functional form of the solution is shown in Equation 2.8

$$\Phi = n_0 V W_{01} \overbrace{\frac{A_{10}}{A_{10} + Q_{10}}}^{\text{Fluorescence Yield}} \quad (2.8)$$

The  $n_0 V W_{01}$  term in Equation 2.8 represents the number of molecules that are excited to the upper state per second, while the fluorescence yield represents the fraction of these molecules that will produce a LIF signal. In typical combustion environments, the fluorescence yield is usually small, since the collisional quenching rate dominates the spontaneous emission rate. The rate of collisional quenching of the fluorescing species by another species in the flame is proportional to the frequency

of collisions between the two. Further, the effectiveness of such collisions is decided  
 by a collision cross-section,  $\sigma$ , which is often a function of the temperature. Equation  
 2.9 presents the calculation of the collisional quenching rate by summation over all  
 the species,  $i$ , in the flame.

$$\begin{aligned}
 Q_{10} &= \sum_i n_i \times \sigma_i \times c_i \\
 &= \sum_i n_i \sigma_i \sqrt{\frac{8kT}{\pi \mu_i}} \\
 &= \sqrt{\frac{8kT}{\pi}} \sum_i \frac{n_i \sigma_i}{\sqrt{\mu_i}}
 \end{aligned} \tag{2.9}$$

In Equation 2.9,  $k$  is the Boltzmann constant,  $T$  is the local temperature,  $n_i$  is  
 the number density of species  $i$  and  $\mu_i$  represents the reduced mass of the colliding  
 molecules, given by Equation 2.10.

$$\mu_i = \frac{m_i m}{m_i + m} \tag{2.10}$$

In Equation 2.10,  $m$  is the mass of the marker species, while  $m_i$  are the masses  
 of the colliding species. Since LIF in combustion primarily targets minor species, by  
 probability, these collisions will almost always occur with major species in the system.  
 As a result, the summation in Equation 2.9 need only be carried out over the major  
 species in the flame. The values of the local number densities of the major species can  
 be measured by techniques like Raman scattering, or can be obtained from solving  
 chemical kinetics models.

#### 2.2.1.1 Absorption Integral Calculation

Let us now briefly examine the first term in Equation 2.8 in further detail. Let  $\phi(\nu)$   
 represent the normalized lineshape of the absorption line being excited, such that



$\int \phi(\nu) d\nu = 1$ . If  $B_{01}$  is the Einstein coefficient for absorption for the line being 501  
excited, the term  $B_{01}\phi(\nu)$  represents the spectral absorptivity of the line at  $\nu$ .  $B_{01}$  502  
is usually presented in  $\text{m}^2/\text{Js}$  for LIF applications. Similarly, let  $I_\nu$  be the spectral 503  
intensity of the incident radiation, which is the intensity (power per area) of the laser 504  
beam per spectral interval. Let  $\psi(\nu)$  be the normalized spectral profile of the laser 505  
lineshape, such that  $I_\nu = I\psi(\nu)$  and  $\int \psi(\nu) d\nu = 1$ .  $I_\nu$  is usually given in  $\text{W}/\text{cm}^2/\text{cm}^{-1}$  506  
for ease of use in laser applications. 507

The product of the spectral absorptivity and the spectral intensity integrated over 508  
the spectrum, gives the pumping rate,  $W_{01}$ , as shown in Equation 2.11. The factor  $c$  509  
is the speed of light, which brings the units of  $W_{01}$  to  $\text{s}^{-1}$ . 510

$$W_{01} = \frac{I}{c} \int \psi(\nu) B_{01} \phi(\nu) d\nu \quad (2.11)$$

#### 2.2.1.2 Population Distribution 511

Once again, consider Equation 2.8, this time focusing on the term  $n_0$ , the number 512  
density of the marker species in the lower energy state that are available for excitation 513  
to the upper state. In reality, this comprises only a small subset of all the available 514  
molecules of the marker species in the system. 515

$$n_0 = n f_0 \quad (2.12)$$

In Equation 2.12,  $n$  is the number density of all marker species over all the energy 516  
levels, while the fraction,  $f_0$ , represents the proportion of the marker species that 517  
populates the lower energy level. 518

Substituting Equations 2.11 and 2.12 into 2.8, and noting that the signal produced is actually integrated over a volume,

520

521

$$\Phi = \int_V \frac{nA_{10}}{A_{10} + Q_{10}} \frac{I}{c} f_0 B_{01} \int_{\nu} \psi(\nu) \phi_j(\nu) d\nu dV \quad (2.13)$$

In Equation 2.13, the absorption integral from Equation 2.11 is highlighted in red. The outer integral is performed in space, over the portion of the flame illuminated by the laser sheet. Under the assumption that the laser intensity is uniformly distributed over the sheet thickness, it is possible to rewrite the outer integral as a 1-D integral over the thickness of the flame by replacing the laser intensity,  $I$  with the laser power,  $P$ .

522

523

524

525

526

527

$$\Phi = \frac{P}{c} \int_x \frac{nA_{10}}{A_{10} + Q_{10}} f_0 B_{01} \int_{\nu} \psi(\nu) \phi_j(\nu) d\nu dx \quad (2.14)$$

Equation 2.14 is thus, the solution to the two-level model in the weak excitation limit. Note that the LIF signal varies linearly as the incident laser power (or intensity). Consequently, the weak excitation limit is also referred to as the linear regime.

528

529

530

For the sake of completion, we will briefly mention the other limit of the two-level model solution that occurs when the rate of pumping far exceeds the relaxation rate ( $W_{01} \gg A_{10} + Q_{10}$ ). This is called the saturated limit and in this limit, the fluorescence signal ceases to change with the intensity of the incident laser beam. Operating in this regime has one major advantage for quantitative LIF measurements; the measured fluorescence signal is nearly independent of the collisional quenching rate, a parameter that can change significantly throughout the combustion. However, there are several drawbacks to operating in this regime. First, the magnitude of the LIF signal per unit incident laser intensity tends to be the maximum in the linear regime. Once the variation ceases to be linear (even before nearing the saturation limit), we

531

532

533

534

535

536

537

538

539

540

get diminishing returns for increasing the laser power. For measurements with low 541  
signal-to-noise ratio, which is often the case for PLIF imaging, this is a significant 542  
drawback. Further, the saturation criterion (maintaining a high laser intensity) is 543  
difficult to satisfy simultaneously in the spatial, temporal and spectral domains. For 544  
these reasons, we will restrict our discussion hence forward the linear regime only. 545

### 2.2.2 CH PLIF Process 546

In this section, we will examine the limitations of trying to apply the two-level model 547  
to describe the CH PLIF process. 548

Laser-Induced Fluorescence is a multi-step process. First, the marker species 549  
absorbs a photon and transitions from a lower energy state to a higher one. This 550  
is followed by several physical processes, of which only one pathway leads to the 551  
spontaneous de-excitation of the excited molecule, accompanied by the release of a 552  
photon. The de-excitation can—but does not need to—take the molecule back to 553  
the original state. If the molecule does return to its original state, the fluorescence 554  
is said to be resonant. Due to the difficulty of measuring fluorescence signals at the 555  
same wavelength as the excitation beam, most practical applications of LIF tend to 556  
be non-resonant. The choice of the spectral and temporal properties of the excitation 557  
laser source, and of the detected fluorescence emission, constitute the excitation and 558  
detection schemes. 559

The excitation scheme chosen for this study follows the work done by Li et al.[\[13\]](#) 560  
who used a ring-cavity, pulsed alexandrite laser to provide excitation in the vicinity 561  
of the R-bandhead of the CH  $B^2\Sigma^- \leftarrow X^2\Pi$  (0,0) system. This bandhead, shown in 562  
Figure [2.6](#), is found at a wavelength of about 387.2 nm and represents transitions from 563  
a ground state rotational quantum number of  $N'' = 7$ . When operated in multimode, 564  
alexandrite lasers have relatively large bandwidths (a few  $\text{cm}^{-1}$  is not uncommon) 565  
and hence make it possible to excite several of the neighboring transitions near the 566

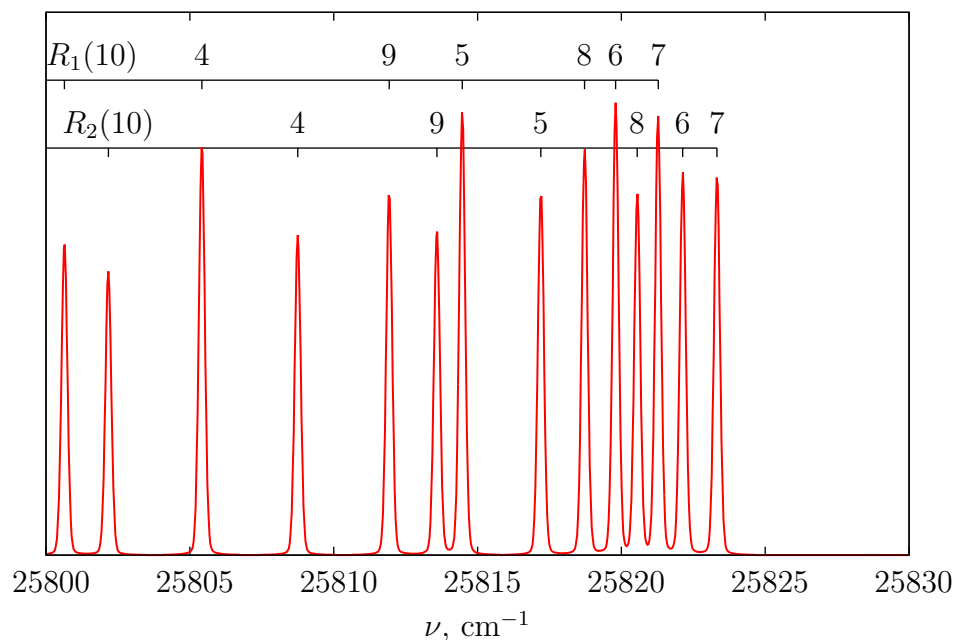


Figure 2.6: The figure shows the frequencies of the absorption lines near the R-bandhead of the  $CH\ B^2\Sigma^- \leftarrow X^2\Pi\ (0,0)$  band. The individual lines are labeled with corresponding  $N''$  quantum number.

bandhead.

Upon excitation, these molecules transition to the second electronically excited  $B^2\Sigma^-$  state and populate the lowest vibrational level, ( $v' = 0$ ). At this point, the following possibilities exist for the excited molecule:

1. The molecule can undergo inelastic collisions with other molecules, resulting in relaxation in the rotational, vibrational or electronic manifolds.
2. The molecule can spontaneously emit a photon and return to any of the lower energy states.
3. The molecule can experience stimulated emission in the presence of another photon of the appropriate frequency and return to any of the lower energy states.
4. The molecule can experience further excitation either by absorbing a photon or

through collisional means and can react chemically.

579

Now, let us examine these potential pathways in greater detail. The first pathway pertains to relaxation. The excitation and subsequent population of a higher energy state causes the CH population distribution to deviate from the equilibrium Boltzmann distribution. The degree of relaxation possible is limited by the lifetime of the energy level the excited species occupy. The maximum time possible for relaxation is given by the collision-free, radiative lifetime of the  $B$  electronic state, which is about 300 ns[63]—long enough for sufficient rotational relaxation to occur, but too short for complete vibrational relaxation. Based on experiments conducted by Garland et al.[64], it is estimated that the vibrational energy transfer between the two bound states available to the  $B^2\Sigma^-$  state is about two orders of magnitude slower than the rotational energy transfer. As a result, we may suppose that the vibrational manifold remains relatively unaffected, while the rotational manifold can partially relax toward an equilibrium distribution. The question of the electronic relaxation will be addressed later in this discussion.

580

581

582

583

584

585

586

587

588

589

590

591

592

593

The second option available for the excited CH molecule is to spontaneously emit a photon and return to a lower energy state. Spontaneous de-excitation to the ground state primarily follows the diagonal  $B^2\Sigma^- \rightarrow X^2\Pi$  (0,0) band. The rate of such spontaneous emission between two states is given by the Einstein emission coefficient for the transition. Once again, we will defer discussion of the  $B - A$  transition until later in this discussion.

594

595

596

597

598

599

The third option is for the CH molecule to experience stimulated emission in the presence of a photon of an appropriate frequency. It is highly unlikely that the apposite photon would have a frequency other than the excitation laser. The rate of stimulated emission induced by the excitation laser beam is proportional to the Einstein absorption coefficient for the transition. Other photons that can induce stimulated emission could originate from spontaneous emission or CH\* chemilumi-

600

601

602

603

604

605

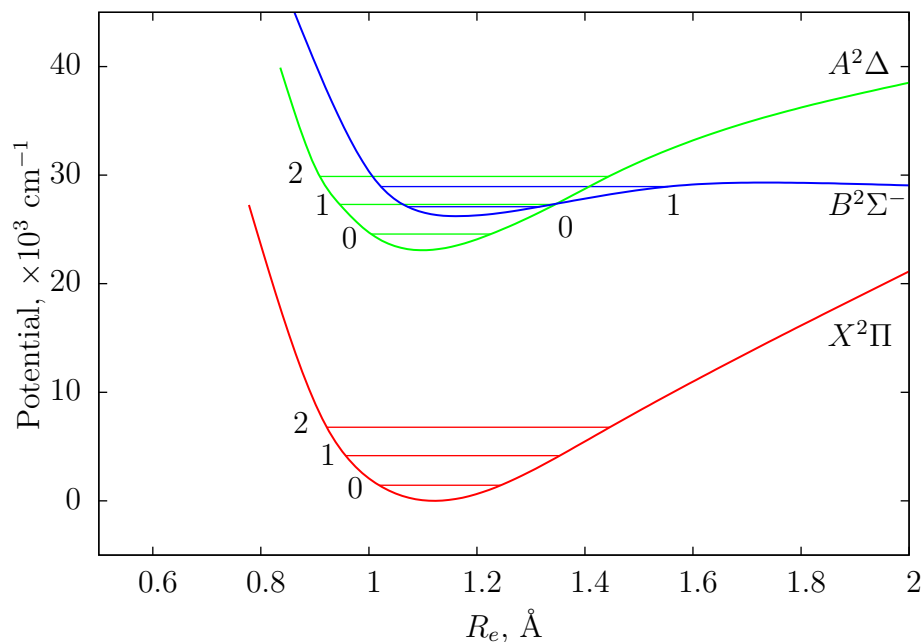


Figure 2.7: The figure shows the RKR potential curves for the  $X^2\Pi$ ,  $A^2\Delta$  and  $B^2\Sigma^-$  energy levels in the CH system. A few vibrational levels are indicated for the  $X^2\Pi$  and  $A^2\Delta$  states. The  $B^2\Sigma^-$  state has only two bound vibrational levels. The diagram is reproduced from Richmond et al.[65] who based it on ab initio calculations by van Dishoeck[66]

nescence, however they would be negligible in intensity compared to the laser. 606

The fourth option is for the molecule to experience further excitation by absorbing 607  
multiple photons or through collisions with other energetic molecules in the system. 608  
Since most available photons do not match any transitions from the  $B^2\Sigma^-$ ,  $v = 0$  state, 609  
it is unlikely to experience multi-photon excitation. However, collisional removal of 610  
CH molecules from the  $B$  state is certainly possible. 611

Having listed all the options, let us resume the discussion on the possibility of 612  
electronic energy transfer from the excited  $B^2\Sigma^-$ ,  $v' = 0$  state. The spacing of the 613  
energy levels in the CH system, shown in Figure 2.7, is such that the  $B^2\Sigma^-$ ,  $v' = 0$  614  
state is found to be near-degenerate with the  $A^2\Delta$ ,  $v = 1$  energy level. Consequently, 615  
the  $B^2\Sigma^- \leftrightarrow A^2\Delta$  (0,1) transition is reversible. Due to this, collisional population of 616  
the  $A^2\Delta$   $v = 0, 1$  states from the  $B^2\Sigma^-$   $v = 0$  state occurs rapidly. Garland et al.[64] 617  
measured that these transfers account for almost a quarter of all collisional depletion 618

of the  $B^2\Sigma^-$ ,  $v = 0$  level. Theoretical calculations using overlap integrals between the involved energy levels predict that a majority of these transfers will be along the diagonal (0,0) transition.[67]. Instead, experimental data indicates that the number is closer to a fifth, with almost 80% of the transfers following the near-degenerate (0,1) pathway.

It is this electronic energy transfer mechanism that enables our excitation scheme to record high quality CH PLIF images. Having now populated the  $A^2\Delta$  states, the resulting spontaneous emission from the  $A^2\Delta \rightarrow X^2\Pi$  (0,0) and (1,1) transitions can be easily observed between 420–440 nm. A small portion of the fluorescence in this wavelength range also occurs from the  $B^2\Sigma^- \rightarrow X^2\Pi$ , (0,1) transition. Since these emission wavelengths are located far from the excitation wavelength, a simple glass filter is sufficient to suppress any elastic scattering from the laser beam.

### 2.2.3 Improved Model

While the two-level model is conceptually simple, applying it to describe the complicated physical process of CH PLIF is challenging. Daily[62] notes, for example, that significant errors can result from using the two-level model to describe even a three-level system. Hence, it is worthwhile to investigate a more complicated model that can describe the CH system with higher fidelity.

Figure 2.8 shows the relevant pathways that lead to the fluorescence emission as discussed in Section 2.2.2. An accurate model of the CH system should involve at least five energy levels, namely the  $B^2\Sigma^-$ ,  $v = 0$ ,  $A^2\Delta$ ,  $v = 0, 1$ , and  $X^2\Pi$ ,  $v = 0, 1$  levels. The model will need to account for collisional transfers between each of these levels, in addition to spontaneous and stimulated transitions. By limiting the model to five levels, we are assuming that the distributions within the rotational manifolds associated with each vibrational level do not play a significant role in altering the net rate of transfer between vibration levels. Even for just five levels, the mathematical



Figure 2.8: Some of the important transitions between energy levels in a CH molecule are shown. The excitation of the CH molecules (blue) is followed by collisional energy transfer processes (red) which populate additional energy levels. Spontaneous emission from some of these energy levels (green) is collected.

solution quickly becomes tedious and complicated. Further, it involves several rate coefficients that have not yet been measured experimentally.

Fortunately, this can be significantly simplified. Previous studies[63, 67] have indicated that the off-diagonal  $B \rightarrow X$  (0,1) transition plays a relatively minor role accounting for only 3.5% of the total fluorescence. Further, the radiative  $A \rightarrow X$  transitions are known[68] to be strongly diagonal, with little or no interaction between the two states. The net result of these two assertions is that we can treat the two  $B \rightarrow A \rightarrow X$  pathways to be disjoint and parallel. The resulting model involving four energy levels is shown in Figure 2.9.

According to this model, the lower state of the CH system is treated as a single pool from which CH molecules are excited from or de-excited to. This not only neglects the rotational manifold, but also the vibrational manifold of the ground state. This assumption would be valid as long as most of the CH molecules occupy the  $v = 0$  state and the fraction of molecules in the  $v = 1$  state can be safely neglected. At flame temperatures of about 2200 K, this assumption is somewhat questionable as only about 83% of the ground state CH molecules occupy the  $v = 0$  level and as much as 14% are found at the  $v = 1$  state. However, in light of the simplifications afforded



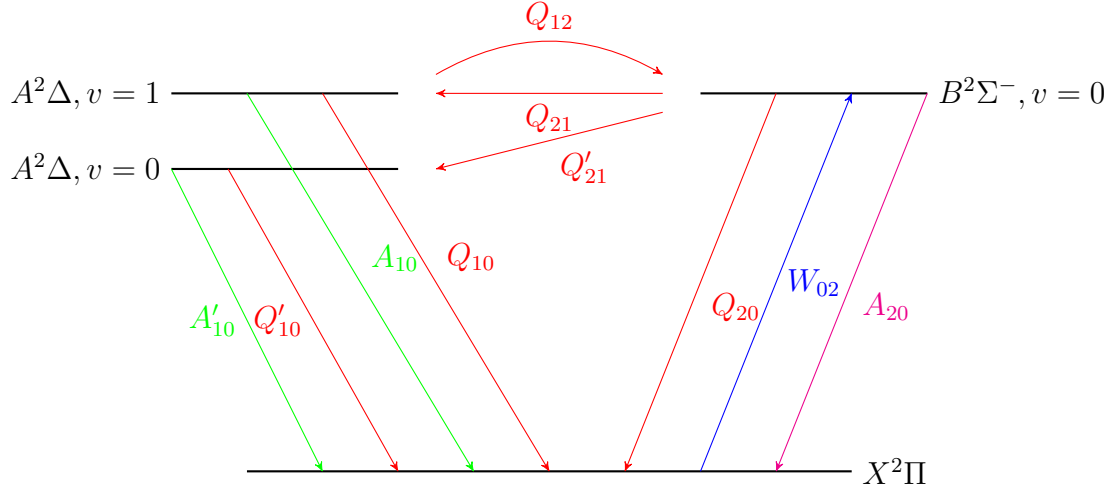


Figure 2.9: A simplified model of the transitions between the energy levels in a CH system. Excitation (blue) of ground state CH molecules to the upper electronic state is followed by several collisional energy transfer processes (red). A small portion of these molecules spontaneously emit a photon (green) and return to ground state. The spontaneous emission corresponding to resonant PLIF (magenta) is not collected.

to our semi-quantitative model by this assumption, we retain it.

The rates of the various transition processes are indicated in Figure 2.9.  $W_{02}$  is the pumping process that populates the  $B(0)$  state.  $Q_{ij}$  are collisional energy transfer processes that transfer CH molecules from the  $i$  level to the  $j$  level. The subscripts 0, 1 and 2 represent the electronic energy levels  $X$ ,  $A$  and  $B$ . Processes involving the  $A(v=0)$  state are differentiated from those involving the  $A(v=1)$  state by a prime ( $'$ ). Finally,  $A_{ij}$  represents the spontaneous emission coefficients between the  $i$  and  $j$  levels.

Applying Equation 2.6 to this case, we can write an expression for the LIF signal intensity as follows,

$$\Phi = (n_1 A_{10} + n'_1 A'_{10})V \quad (2.15)$$

Our task is to solve for the values of  $n_1$  and  $n'_1$  in terms of  $n_0$ . To do this we need to write rate equations describing the variation of the populations of the three upper states with time.

$$\frac{dn_1}{dt} = -(A_{10} + Q_{10} + Q_{12})n_1 + Q_{21}n_2 \quad (2.16)$$

$$\frac{dn'_1}{dt} = -(A'_{10} + Q'_{10})n'_1 + Q'_{21}n_2 \quad (2.17)$$

$$\frac{dn_2}{dt} = W_{02}n_0 + Q_{12}n_1 - (A_{20} + Q_{20} + Q_{21} + Q'_{21})n_2 \quad (2.18)$$

Under the assumption that the laser excitation time scale is much longer than the collisional time scales, we can set the LHS of Equations 2.16–2.18 to zero. This results in a closed set of linear equations, which can be expressed in matrix form as follows.

$$\begin{bmatrix} A_{10} + Q_{10} + Q_{12} & 0 & -Q_{21} \\ 0 & A'_{10} + Q'_{10} & -Q'_{21} \\ -Q_{12} & 0 & A_{20} + Q_{20} + Q_{21} + Q'_{21} \end{bmatrix} \begin{bmatrix} n_1 \\ n'_1 \\ n_2 \end{bmatrix} = \begin{bmatrix} 0 \\ 0 \\ W_{02}n_0 \end{bmatrix} \quad (2.19)$$

From Equation 2.19, we only need the solutions to  $n_1$  and  $n'_1$ . Substituting the solutions directly into Equation 2.15, we can write the solution in the following form to mirror the expression in Equation 2.8.

$$\Phi = n_0 V W_{02} (Y + Y') \quad (2.20)$$

The terms  $Y$  and  $Y'$  in Equation 2.20 are non-dimensional and represent the fluorescence yields from the two  $A^2\Delta$  states. The functional expression for the yields is more complex now, as shown in Equations 2.21–2.22.

$$Y = \frac{Q_{21}A_{10}}{(A_{10} + Q_{10} + Q_{12})(A_{20} + Q_{20} + Q_{21} + Q'_{21}) - Q_{12}Q_{21}} \quad (2.21)$$

$$Y' = \frac{(A_{10} + Q_{10} + Q_{12})Q'_{21}A'_{10}}{(A'_{10} + Q'_{10})((A_{10} + Q_{10} + Q_{12})(A_{20} + Q_{20} + Q_{21} + Q'_{21}) - Q_{12}Q_{21})} \quad (2.22)$$

### 2.2.3.1 Absorption Integral Calculation

We now focus on the first portion of Equation 2.20 and consider the rate of population of the upper  $B^2\Sigma^-$  state. As in case of the simple two-level model, this term involves the computation of the integral of the product of the laser linewidth function,  $\psi(\nu)$  and the absorption linewidth function,  $\phi(\nu)$ . However, since our excitation scheme targets multiple lines in the R-bandhead, we actually have a summation of several absorption lines in this integral.

$$\begin{aligned} W_{02} &= \frac{I}{c} \int \psi(\nu) \sum_j B_j \phi_j(\nu) d\nu \\ &= \frac{I}{c} \sum_j B_j \int \psi(\nu) \phi_j(\nu) d\nu \end{aligned} \quad (2.23)$$

In Equation 2.23, the terms  $B_j$  are the absorption coefficients,  $B_{02}$ , for each transition being excited, each of which has its own broadened linewidth,  $\phi_j(\nu)$  at the local conditions. The discussion of the various sources of line broadening that need to be considered for our case is deferred till Chapter 4.

### 2.2.3.2 Population Distribution

696

Equation 2.24 presents the expression for  $f_j$  in terms of the vibrational and rotational quantum numbers,  $(v, J)$ , of the energy level  $j$ .

697

698

$$f_j(v, J) = \frac{\exp\left(\frac{-hcE_v(v)}{kT}\right)(2J+1)\exp\left(\frac{-hcE_r(v, J)}{kT}\right)}{Q_{rv}} \quad (2.24)$$

The vibrational energy,  $E_v(v)$  of a level is calculated according to Equation 2.25, while the rotational energy,  $E_r(v, J)$  is calculated according to Equation 2.26.

699

700

$$E_v(v) = \omega_e \left(v + \frac{1}{2}\right) - \omega_e x_e \left(v + \frac{1}{2}\right)^2 + \omega_e y_e \left(v + \frac{1}{2}\right)^3 - \omega_e z_e \left(v + \frac{1}{2}\right)^4 \quad (2.25)$$

$$E_r(v, J) = \left\{B_e - \alpha_e \left(v + \frac{1}{2}\right)\right\} J(J+1) - \left\{D_e + \beta_e \left(v + \frac{1}{2}\right)\right\} J^2(J+1)^2 \quad (2.26)$$

The ground state,  $X^2\Pi$ , of the CH system is conforms to Hund's Case b[69] and hence, the appropriate rotational quantum number to use is  $N$ . For each rotational quantum number  $N$ , there are two possible values of  $J$  given by  $N \pm \frac{1}{2}$ . The rovibrational partition function,  $Q_{rv}$  is a summation over all available vibrational and rotational levels in the  $X^2\Pi$  state. In practice, this summation over the vibrational states may be truncated at  $v = 4$  and the summation over the rotational states may be truncated at  $N'' = 22$  with negligible loss in accuracy. The values of the various spectroscopic constants in the above equations will be presented in Chapter 4.

701

702

703

704

705

706

707

708

The solution for the rate of production of fluorescence photons can be written in the following form that mirrors Equation 2.14.

710  
711

$$\Phi = \frac{P}{c} \int_x n_{CH}(Y + Y') \sum_j f_j B_j \int_\nu \psi(\nu) \phi_j(\nu) d\nu dx \quad (2.27)$$

The expressions for the fluorescence yields,  $Y$  and  $Y'$ , still have many variables that have not been tabulated conveniently in literature. As a result, further simplifications will need to be made on the basis of reported experimental observations. These simplifications are outside the scope of this chapter and will be introduced in Chapter 4 along with the results of applying this model to various reactant mixtures.

712

713

714

715

716

## CHAPTER 3

717

### EXPERIMENTAL METHODS AND CONSIDERATIONS

718

The current chapter describes the experimental apparatus and the diagnostic approaches used in this work. The first section presents a detailed description of the LSB configurations that were tested, along with the testing facilities used for the experimental work. The second section focuses on the selection and implementation of the diagnostic techniques that were used to study flames and flow fields. Data reduction techniques used to process the acquired raw data are also described.

719

720

721

722

723

724

#### 3.1 LSB Configurations

725

Two configurations of the Low Swirl Burner were tested for this study. These are referred to in what follows as Configurations A and B. Each configuration consists of the reactant flow inlet, the swirler device, the conduit to the combustion zone and the combustion zone itself. Figure 2.1 shows the design of the swirlers used for this study. Each swirler has an outer diameter,  $d_s$ , of 38 mm (1.5 in) and divides the flow into a central and annular portion. One of these configurations used swirlers with a perforated plate that had a concentric hole pattern as shown in the figure. The perforated plate induces a blockage in the central channel and controls the relative mass flow split between the two portions of the swirler. The key dimensions of the swirlers tested are presented in Table 3.1.

726

727

728

729

730

731

732

733

734

735

Each configuration is housed in a high pressure testing facility. The testing facility consists of an air and fuel supply system, a pressure vessel with adequate optical access and an exhaust system for the products. Each testing facility is instrumented to measure temperatures and pressures which are then used to calculate various flow

736

737

738

739

Table 3.1: *The dimensions of the swirlers used and the respective perforated plates are presented. Each swirler is referred to by its vane angle (as in “ $S_{37^\circ}$ ”).*

Geometric parameter	Swirlers		
	Configuration A $S_{37^\circ}$	$S_{45^\circ}$	Configuration B $S_{40^\circ}$
<b>Swirler data</b>			
Outer diameter, $d_s$ , mm	38	38	38
Diameter ratio, $\frac{d_i}{d_s}$	0.66	0.66	0.66
Vane angle, $\alpha$	$37^\circ$	$45^\circ$	$40^\circ$
Theoretical Swirl Number, $S$	0.48	0.64	variable
<b>Perforated plate data</b>			N/A
Open area, $\text{mm}^2$	155.97	156.98	-
Blockage, %	71.54	71.36	-
Plate thickness, mm	1.27	1.27	-
Hole pattern	1 - 8 - 16	1 - 8 - 16	-
Hole location (dia), mm	0 - 10.2 - 19.1	0 - 10.2 - 19.1	-
Hole diameter, mm	2.79 - 2.79 - 2.84	2.82 - 2.82 - 2.83	-

parameters of interest.

The design of the configurations tested, along with that of their respective test facilities are discussed in detail in this section.

### 3.1.1 Configuration A

Preliminary experiments involving velocity field mapping and flame imaging were performed using this configuration. The schematic of the high pressure test facility housing this configuration is shown in Figure 3.1, while the configuration itself is shown in greater detail in Figure 3.2.

#### 3.1.1.1 Test Facility

Pressurized air is supplied from external tanks and heated in an indirect, gas-fired heat exchanger to about 500 K. The flowrate of the air is metered using a sub-critical orifice flow meter with a 38 mm (1.5 in) bore diameter Flow-Lin orifice plate capable

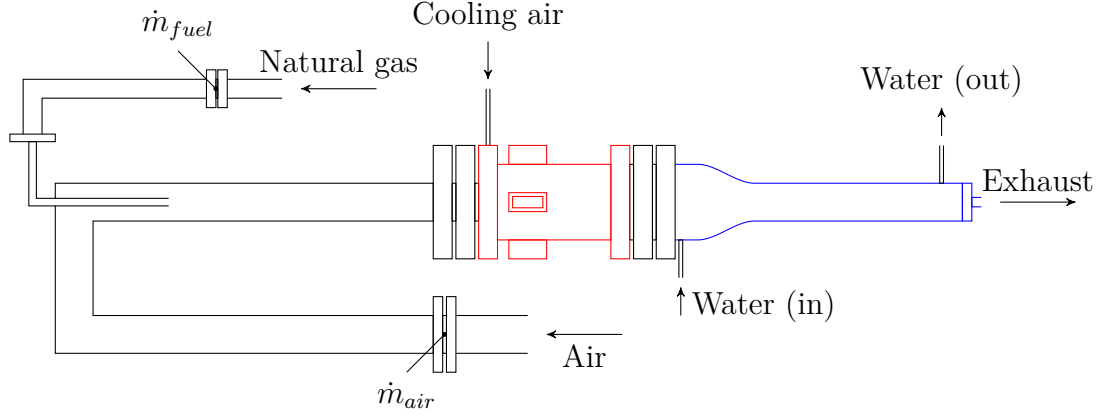


Figure 3.1: A schematic of the high pressure testing facility where Configuration A was operated is shown. The pressure vessel is outlined in red, while the water-cooled exhaust section is outlined in blue. The locations of the orifice flow meters used to measure the mass flow rates of the preheated air and natural gas fuel are indicated.

of metering a maximum flow rate of 2.2 kg/s (1 lb/s). The orifice flow meter is instru- 752  
 mented with an Omega PX725A-1KGI pressure transmitter calibrated to a reduced 753  
 pressure range of 0–2.758 MPa (0–400 psi), a shielded K-type thermocouple and an 754  
 Omega PX771A-025GI differential pressure transmitter, calibrated to a reduced dif- 755  
 ferential pressure range of 0–68.948 kPa (0–10 psid). The fuel (natural gas) is metered 756  
 using a similar set up as the air line, with a sub-critical orifice flow meter. The fuel 757  
 orifice plate is a Flow-Lin orifice plate with a bore diameter of 13.46 mm (0.53 in), 758  
 capable of metering a maximum flow rate of 0.22 kg/s (0.1 lb/s). The upstream pres- 759  
 sure is measured using an Omega PX725A-1KGI pressure transmitter (same as the 760  
 air line) and the differential pressure is measured using a PX771A-100WDC differ- 761  
 ential pressure transmitter with a pressure range of 0–2.489 kPa (100 in H<sub>2</sub>O). The 762  
 temperature of the fuel is assumed to be the same as the nominal room temperature 763  
 (300 K). 764

The air enters the inlet nozzle of the LSB through a 1.8 m (6 ft) long, 102 mm (4 765  
 in) diameter straight pipe section. The fuel flow is choked prior to mixing with the 766  
 flow at the head of the straight pipe section. The straight pipe section allows for the 767  
 flow to be fully developed, and fully premixed before the reactants enter the burner. 768



The combustor pressure and temperature are measured at the head of the inlet nozzle. 769

The pressure is measured by an Omega PX181B-500G5V pressure transducer with a 770

pressure range of 0–3.45 MPa (0–500 psi), while the temperature is measured using 771

a K-type thermocouple. 772

The pressure and temperature measurements are used to calculate the four pri- 773

mary flow parameters (combustor pressure, preheat temperature, reference velocity 774

and equivalence ratio) for the LSB in real time. All measurements are monitored and 775

recorded during the course of the experiment by a LabView VI. 776

The pressure vessel enclosing the combustor is designed to withstand pressures of 777

up to 30 atm and is insulated from the combustor by a ceramic liner. Cooling for the 778

pressure vessel and the quartz tube is provided by a flow of cold air introduced at the 779

head of the pressure vessel. The cold air is drawn from the same external tanks as 780

the main air line, but bypasses the heating system. The cold air flow is not metered, 781

but its upstream pressure is coupled to the main air line so as to ensure a steady flow 782

of cold air into the pressure vessel at all operating conditions. Optical access to the 783

combustor is provided through four 25 mm (1 in) thick, 150 mm (6 in)×75 mm (3 in) 784

quartz windows located 90° apart azimuthally. The view ports allow the combustor 785

to be imaged from the dump plane to an axial distance of 150 mm (6 in) downstream. 786

The exhaust from the combustor is cooled by cold water circulated through a 787

water jacket enclosing each section of the exhaust pipe. The length of the exhaust 788

pipe sections is about 1.8 m (6 ft). The exhaust pipe section terminates in an orifice 789

plug that provides back pressure to the combustion chamber. A different diameter 790

orifice is used for each reference velocity condition tested. The exiting products finally 791

pass through the building exhaust system. 792

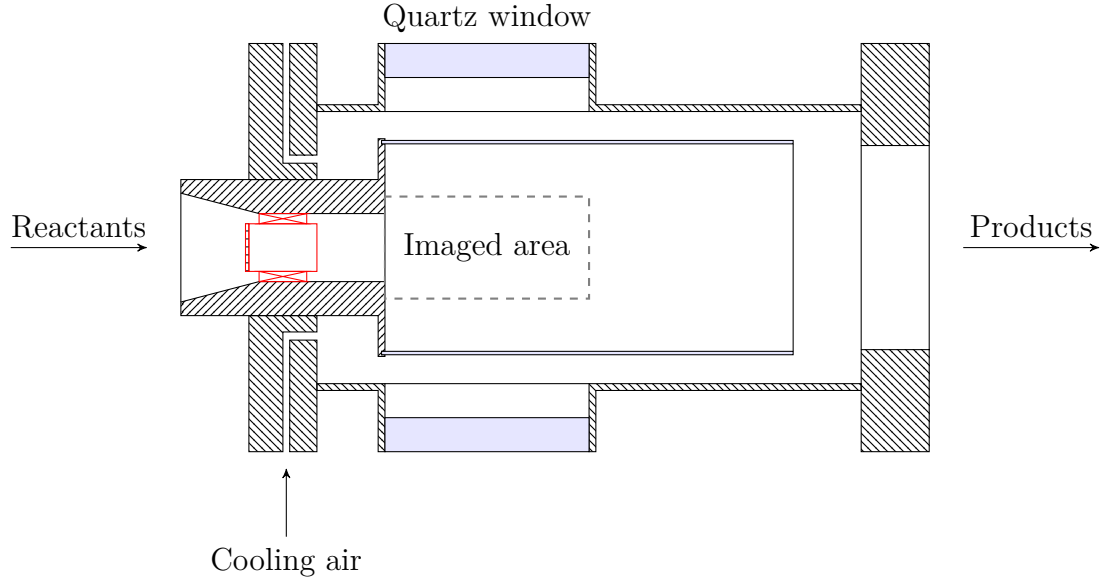


Figure 3.2: A cross-sectional view of Configuration A in the pressure vessel is shown. The reactants enter from the left. The products mix with the cooling air and leave on the right. The location of the swirler in the inlet nozzle is highlighted in red. Also shown is the region of the combustion zone that can be imaged through the quartz windows.

### 3.1.1.2 Low Swirl Burner

A detailed schematic of the LSB configuration is shown in Figure 3.2. The premixed, preheated reactants reach the swirler through a converging nozzle that decreases linearly in diameter from the inlet diameter of 102 mm (4 in) to the outer diameter of the swirler, 38 mm (1.5 in). At the swirler, the flow splits into two streams—one passing through the central section and another picking up swirl by flowing over the vanes in the annular region. The relative flow split between the two streams is controlled by inducing blockage into the central flow by means of a perforated plate. The swirler leads to a constant area nozzle, and is located one diameter upstream of an abrupt area change. At the area change, the reactants expand from the 38 mm (1.5 in) diameter nozzle into a 115 mm (4.5 in) diameter combustion zone. This expansion ratio is chosen so as to avoid confinement effects on the centerline flame flow field.[28]

The main combustion zone begins at the dump plane and is enclosed by a GE

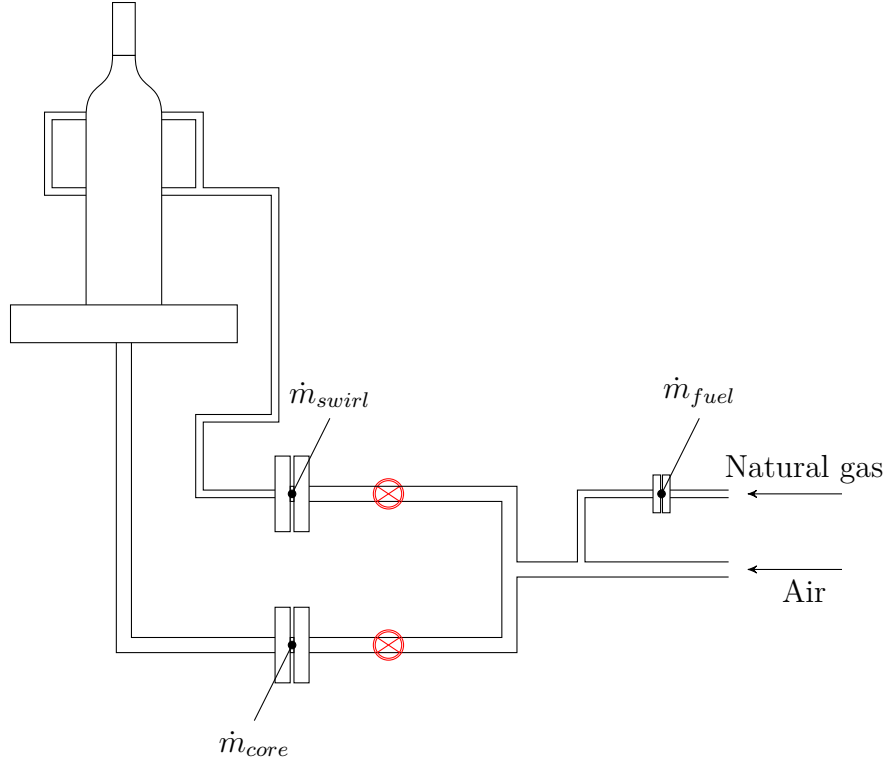


Figure 3.3: A schematic of the high pressure testing facility where Configuration B was operated is shown. The locations of the orifice flow meters on the reactant streams and fuel lines are shown. Valves (shown in red) on the swirl and core flow lines allow for the relative mass flow split to be varied between the two reactant streams. The upstream orifice flow meter on the preheated air line is not shown here. All preheated air lines are insulated.

214 quartz tube. The quartz tube is 300 mm (12 in) long and 115 mm (4.5 in) in diameter. The thickness of the quartz tube is 2.5 mm (0.1 in).

### 3.1.2 Configuration B

This configuration is used to image the flame structure of the LSB flame using CH PLIF. A schematic of the flow system of the test facility is shown in Figure 3.3, while the LSB combustor itself is shown in greater detail in Figure 3.4.

#### 3.1.2.1 Test Facility

This test facility shares the upstream supply of preheated air and natural gas with the one used in Configuration A. The flow rate of the preheated air stream is mea-

sured using the same orifice flow meter system used in Configuration A—albeit with a smaller 12.921 mm (0.5087 in) diameter bore Flow-Lin orifice plate. The fuel system pressure is regulated from the building supply pressure to a lower required pressure by an adjustable TESCOM regulator and metered using a critical orifice flow meter. The critical orifice on the fuel line has a bore diameter of 0.8128 mm (0.032 in). The pressure upstream of the critical orifice is measured using an Omegadyne PX409-1.5KGI pressure transmitter with a range of 0–10.34 MPa (0–1500 psig) and the pressure downstream of the critical orifice is measured using a Dwyer 626 series pressure transmitter with a range of 0–3.45 MPa (0–500 psig). The downstream pressure can be used to verify if the critical orifice is choked during operation. The temperature of the fuel is measured upstream by a K-type thermocouple.

The air system is choked with a 5.41 mm (0.213 in) diameter critical orifice before mixing with the fuel. A short distance after mixing, the reactants are split into two separate streams for the central flow and the swirl flow. The central flow rate is measured using a 9.271 mm (0.365 in) diameter sub-critical orifice, instrumented with a Dwyer 626 series pressure transmitter with a range of 0–4.14 MPa (0–600 psig) for measuring the upstream pressure, a K-type thermocouple for measuring the upstream temperature and an Omega PX771-300WCDI differential pressure transducer with a range of 0–74.65 kPa (0–300 in H<sub>2</sub>O). The swirl flow rate is measured similarly, using a 11.68 mm (0.46 in) diameter sub-critical orifice, a Dwyer 626 series pressure transmitter with a range of 0–5.52 MPa (0–800 psig), a K-type thermocouple and another Omega PX771A-300WCDI with a differential pressure range of 0–74.65 kPa (0–300 in H<sub>2</sub>O). The relative flow split between the two reactant streams is controlled by partially closing gate valves on the two lines. All measurements are monitored and recorded by a LabView VI.

The test rig is designed to be operated with a pressure vessel and is rated for pressures as high as 30 atm. Unfortunately, the rig could not be operated at high

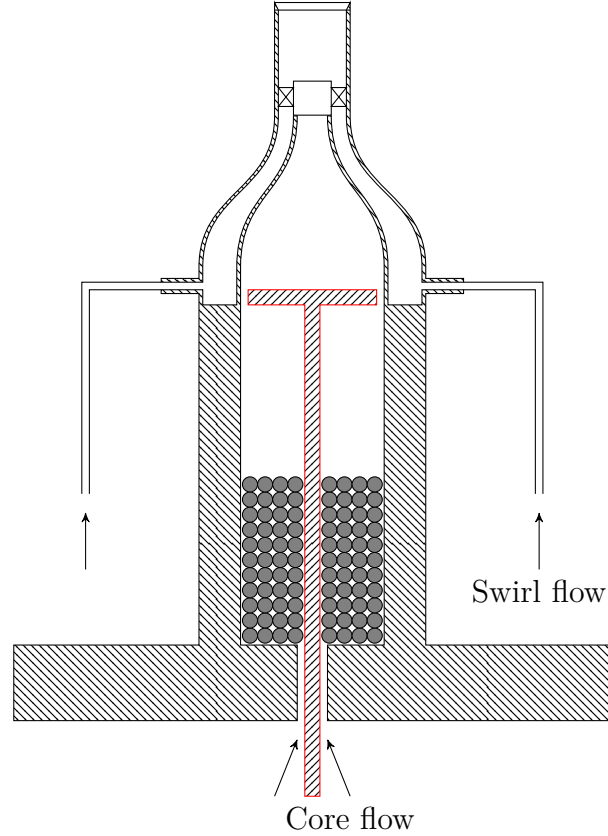


Figure 3.4: A cross-sectional view of Configuration B is shown. The core flow reactants enter through ports in the base flange. Stainless steel ball bearings partially fill the plenum chamber and render the core flow spatially uniform. The turbulence generator is located within the plenum and is outlined in red. The swirl flow reactants enter through separate pipes and are injected into the contoured nozzle through four ports.

pressure for the experiments performed in this study. The original design of the rig, 843  
developed for a separate program of research investigating turbulent flame speeds, 844  
was found to be incapable of successful operation at high pressure. As a result, the 845  
combustor was operated without a pressure vessel in the present work. The products 846  
are vented into the same building exhaust system as Configuration A. 847

### 3.1.2.2 Low Swirl Burner 848

The design of this LSB configuration is presented in Figure 3.4. As described ear- 849  
lier, the reactants reach the LSB swirler device through two separate streams. The 850  
core/central stream passes through a plenum chamber that is filled with steel ball 851

bearings before approaching the swirler through a smoothly contoured nozzle with a high contraction ratio. The annular/swirl stream reaches the swirler directly through a separate contoured nozzle. The contraction ratio is chosen to inhibit the formation of thick boundary layers in the reactant streams. The core stream passes through the central portion of the swirler, while the annular stream picks up swirl by passing through the vanes of the swirler. The swirler lacks a perforated plate covering the central region as the primary function of the plate—regulating the relative mass flow split—is performed by the test facility itself.

The swirler device is located at the beginning of a constant area nozzle which is 57.2 mm (2.25 in) in length. Following this, the reactants expand into the combustion zone.

Unlike Configuration A, there is no dump plane or quartz tube to provide confinement to the combustion zone. The co-flow of cold air provides insulation to the walls of the pressure vessel. Also, as mentioned earlier, the relative mass flow split between the central and annular flows can be controlled directly. Finally, the level of turbulence in the central flow can be adjusted by use of a turbulence generator[70] located upstream in the plenum chamber.

## 3.2 Diagnostics

### 3.2.1 Laser Doppler Velocimetry

The velocity field of the LSB is mapped using a TSI 3-component LDV system. Three wavelengths (514 nm, 488 nm and 476 nm) are separated from the output of a 5 W Argon ion laser by an FBL-3 multicolor beam generator. The individual beams are split into two coherent beams, which are then focused to intersect and produce interference fringes within an ellipsoidal measurement volume with dimensions of the order of 100  $\mu\text{m}$ . For this purpose, two transceiver probes are mounted 90° apart

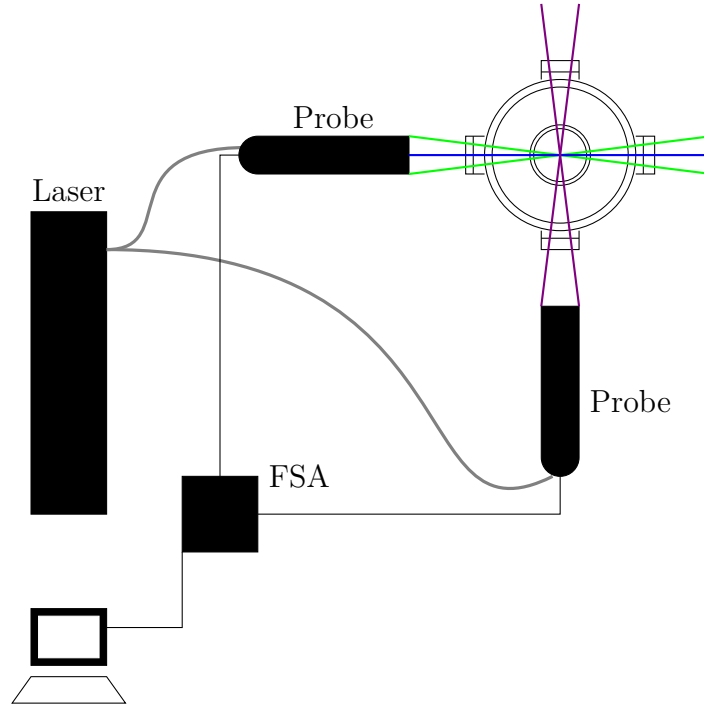


Figure 3.5: The schematic shows the setup employed to map the velocity field of the LSB combustor using Laser Doppler Velocimetry. Three pairs of orthogonal beams are separated from the Argon Ion Laser output and conveyed by fiber optic cables (gray) to optical probes mounted  $90^\circ$  apart about the axis of the LSB combustor. The green, blue, and violet beams in the schematic represent the 514 nm, 488 nm and 476 nm wavelengths. The signal is collected by the transceiver probes and analyzed by the FSA module. The results are saved for further analysis.

about the axis of the LSB. The setup is illustrated in Figure 3.5. One transceiver probe focuses the 514 nm and 488 nm beams in planes perpendicular to each other, while the second probe focuses the 476 nm beams orthogonal to the other two beams. Particles in the flow field crossing the interference fringes scatter the laser light elastically and produce a sinusoidal signal whose frequency is proportional to the velocity of the particle. The transceiver probes collect this scattered light and each wavelength is detected separately by a PDM-1000-3 three-channel photodetector module. The output from the photodetector is processed by an FSA-3500-3 signal processor. The resulting three components of the particle/flow velocity are recorded by the FlowSizer software.

Since the concentration of particulate matter (primarily dust particles) in the airflow is very low, the flow needs to be artificially seeded to facilitate LDV measurements in a reasonable amount of time. The choice of seeding particles to be used and their mean diameter are decided by the characteristics of the flow to be imaged.[71] Since the LSB flow field is a reacting one, the particles need to have high melting points. Further, the particles need to be small enough to follow the flow closely and large enough or reflective enough to scatter light efficiently in the measurement volume. Based on these requirements, commercially available alumina particles with a mean particle diameter of 5  $\mu\text{m}$  were chosen for this study. In order to uniformly seed the flow, a novel seeding generator was designed as described in Appendix A. The seeding particles were introduced slightly upstream of the 1.8 m (6 ft) long straight pipe section in Test Rig A.

LDV data is only acquired at atmospheric pressure conditions. At high pressure conditions, the reacting LSB flow field produces sharp refractive index gradients that rapidly shift in the turbulent flow field. This causes strong beam steering effects making it very difficult for the laser beams to reliably intersect within such a small measurement volume.[72] The long distance traveled by the beams in the test rig



further exacerbate this problem, making LDV data nearly impossible to acquire at such conditions.

### 3.2.2 CH\* Chemiluminescence

The LSB flame is imaged using one of two 16-bit intensified CCD cameras—PI Acton 1024×256 or 512×512 pixels—with a 28 mm f/2.8 camera lens. The quantum efficiency of the 18 mm Gen III HB filmless intensifier used by the 512×512 camera is about 45% at 430 nm, while the 25 mm Gen II intensifier used by the 1024×256 camera manages about half that at the same wavelength. CH\* chemiluminescence is filtered using a bandpass filter centered on 430 nm with a FWHM of 10 nm. At each operating condition, 100 instantaneous images are acquired with an exposure of 1 ms. An additional 100 instantaneous images are acquired with no flame and averaged to yield the background for correcting the flame images.

#### 3.2.2.1 Image Processing

The acquired flame chemiluminescence images are background-corrected and averaged. The resulting mean is the line-of-sight integrated, time-averaged image of the flame. Strictly speaking, this is not the same as a real average obtained from a long exposure image as the instantaneous images are obtained through a periodic sampling process and hence, are prone to statistical errors. However, the behaviour of the flame can be assumed to be sufficiently random that the mean obtained is adequately representative of the true average. Figure 3.6a shows a typical mean CH\* chemiluminescence image prepared in this manner.

Even when background-corrected, the walls of the combustor are not at zero intensity in the average chemiluminescence image. This is particularly noticeable near the dump plane where there is no flame present and yet the walls are clearly illuminated. The source of this background illumination is mostly the chemiluminescence



(a) *Average  $CH^*$  chemiluminescence image*



(b) *Centerline  $CH^*$  chemiluminescence intensity*



(c) *Abel deconvoluted half-image*

Figure 3.6: *These images illustrate the processing of a typical  $CH^*$  chemiluminescence dataset. The top image is the mean of 100 frames and shows the LSB flame at 9 atm. The flame standoff distance is calculated by locating the inflection point in the smoothed intensity profile (middle). An Abel deconvolution (bottom) can be used to highlight the flame brush and measure the angle of the flame.*

from the flame scattering off the combustor and pressure vessel walls. The contribu- 929  
tion from blackbody radiation from the heated walls is less significant in the narrow 930  
wavelength range imaged. This is evident from images acquired immediately after a 931  
flame blowout, which show the walls to be nearly dark even though they should still 932  
be hot. 933

The averaged chemiluminescence image allows us to measure the flame stand- 934  
off distance by following the intensity profile along the centerline of the combustor. 935  
The intensity profile rises sharply when passing the flame standoff location. Thus, 936  
the flame standoff location can be ascertained by finding the inflection point in the 937  
intensity profile. 938

The profile of the average chemiluminescence intensity along the centerline of the 939  
sample case from Figure 3.6a is shown in Figure 3.6b, showing the flame standoff 940  
distance. The distance from the dump plane, measured in number of pixels on the 941  
image and scaled by the appropriate magnification factor yields the flame standoff 942  
distance,  $X_f$ . The determination of the flame standoff location by this method pro- 943  
vides a suitable and deterministic means to locating the leading edge of the flame 944  
front. 945

The average image can be processed further to yield more spatially resolved in- 946  
formation about the flame brush. Under the reasonable assumption that the average 947  
LSB flame is axially symmetric about the centerline of the combustor, a tomographic 948  
deconvolution technique called an Abel deconvolution[73] can be used to convert the 949  
line-of-sight integrated image to a radial map of chemiluminescence intensity. In 950  
effect, this shows the shape and structure of the average flame brush. The Abel 951  
deconvolution of the sample data from Figure 3.6a is shown in Figure 3.6c. 952

The Abel-deconvoluted image provides a relatively easy means of determining the 953  
flame brush angle. A straight line joining two points located at the center of the 954  
flame brush intersects the axis of the combustor at this angle. The angle of the flame 955



Figure 3.7: A schematic of the components of the PAL 101 Alexandrite laser is shown. The resonator formed by a High Reflection (HR) mirror and an output coupler is built around an alexandrite rod (red) pumped by flashlamps. The frequency of the output is selected by a tuner mechanism. Only one of the two Q-switches was used for this study. The laser beam is reduced in diameter by a collimating telescope (blue) before passing through the Second Harmonic Generator (SHG). The UV beam is separated from the fundamental by a dichroic mirror and exits the laser. The fundamental beam terminates within the laser in a beam dump.

is denoted by  $\theta_f$ .

Using the Abel deconvolution to study the flame brush suffers from two main drawbacks. First, the system of equations describing the Abel deconvolution is only valid as long as the entirety of the flame is visible. This is only satisfied in the initial region of the LSB where the diameter of the flame brush is smaller than the height of the optical viewport. At further downstream locations, the flame is not imaged in its entirety. This causes the spurious bright regions near the top of the window in Figure 3.6c. The second limitation of the Abel deconvolution technique stems from the high incidence of errors along the centerline (where  $r \rightarrow 0$ ). Due to this, any study of the flame brush thickness at the flame stabilization point—a metric of considerable importance—is all but impossible using this tomographic technique.

### 3.2.3 CH Planar Laser-Induced Fluorescence

The CH PLIF setup uses the frequency-doubled output of a Light Age PAL 101 alexandrite laser tuned to  $\lambda \approx 387.2$  nm. The design of the laser is shown schematically in Figure 3.7. The active medium is a 150 mm (6 in) long, 5 mm (0.197 in) diameter alexandrite rod. The rod is placed between two flashlamps within the

resonator cavity formed by two spherical mirrors. A birefringent tuning element is placed within the resonator to allow the user to select the frequency of the output beam. The tuning element is coupled to a micrometer whose reading relates linearly to the output wavelength. The birefringent filter allows the fundamental wavelength to be varied between 720–780 nm, with peak gain at about 755 nm. The resonator cavity also contains two Q-switches, which allow the laser to optionally operate in double-pulsed mode. For this study, however, only one Q-switch is used and the laser is operated in single-pulsed mode only.

The diameter of the fundamental beam exiting the output coupler is reduced by a collimating telescope. This is done in order to increase the efficiency of conversion of the frequency-doubling crystal. The second harmonic portion of the beam is separated from the fundamental by a dichroic mirror and exits the laser. The fundamental beam is terminated at a beam dump within the laser. The exit beam diameter is about 1 mm.

The alexandrite laser is capable of operating at frequencies of up to 15 Hz. Laser power is controlled primarily by varying the voltage applied to the flash lamps. When operating with a high flash lamp voltage, it is recommended that the frequency of pulsing be reduced to allow more time to dissipate the heat build up within the alexandrite rod. All experiments conducted as part of this study operated the laser at 10.0 Hz.

The typical power output of the laser is about 15 mJ/pulse. The pulsewidth of the laser is about 60-80 ns, as measured by a fast photodiode, and the pulsewidth decreases with increasing flash lamp voltage. The linewidth of the fundamental beam, as reported by the manufacturer, is 150 GHz at  $\lambda = 775$  nm. Assuming the spectral profile of the laser to be a Gaussian, the linewidth of the frequency-doubled beam can be determined. The Full Width at Half Max (FWHM) of a Gaussian curve scales linearly with the standard deviation of the curve. When convoluted with itself, the

new standard deviation is  $\sqrt{\sigma^2 + \sigma^2}$  or  $\sqrt{2}$  times that of the original curve. Thus, the  
linewidth of the frequency doubled output is  $150 \times \sqrt{2} = 212$  GHz or  $7.07 \text{ cm}^{-1}$ . In  
wavelength units, this represents a spread of about  $1.06 \text{ \AA}$ .

### 3.2.3.1 Imaging System

All of the PLIF imaging is performed with an intensified PI Acton  $512 \times 512$  camera.  
The intensified camera is equipped with an 18 mm Gen III HB filmless intensifier  
with a quantum efficiency of about 45% in the 420–440 nm range. The lens is chosen  
depending on imaging requirements of each experiment. In all imaging experiments,  
elastic scattering from the laser beam is attenuated by a 3 mm thick GG 420 Schott  
Glass filter.

### 3.2.3.2 Laminar Flame Setup

Preliminary experiments to evaluate the CH PLIF technique are performed on a  
laminar flame. The choice of a laminar flame as the subject allows us to neglect  
effects of strain and turbulence on the flame. Further, laminar flames are more readily  
simulated by reaction kinetics packages like Chemkin with high fidelity, allowing us  
to model the LIF signal easily.

These experiments are conducted on a laminar, methane-air flame stabilized on  
an unpiloted Bunsen burner with an inner diameter of 10.16 mm (0.4 in). The air  
flow rate is measured and regulated using a Dwyer rotameter with a range of 0–20  
SCFH calibrated using a Ritter drum-type gas meter. The natural gas flow rate is  
metered using a Matheson FM 1050 602 rotameter with a range from 0–1230 SCCM.  
This flowmeter is calibrated using a Sensidyne Gilibrator 2 bubble flow meter system.



Figure 3.8: The figure above shows the schematic of the experiment performed to calibrate the wavelength of the laser output. The laser output (containing mostly UV, but also a small portion of the fundamental frequency) is glanced off a steel optical post. The scattered light is gathered by a fiber optic cable (gray) and sent to a spectrometer. The spectrum is analyzed to track the location of the fundamental frequency with tuner position. The UV peak is not tracked as the spectrometer is not calibrated for that wavelength.

### 3.2.3.3 Laser Wavelength Calibration

1021

As described earlier, the output wavelength of the PAL 101 alexandrite laser is 1022 controlled using a micrometer-coupled birefringent tuning mechanism. The wave- 1023 length of the laser beam varies linearly with the micrometer reading. Initially, the 1024 manufacturer-supplied calibration for the micrometer was found to be inaccurate. 1025 This required an experiment to calibrate the laser output wavelength against the mi- 1026 crometer reading in order to determine the slope and offset of the calibration curve 1027 accurately. 1028

A schematic of this experiment is shown in Figure 3.8. The laser beam is glanced 1029 off a steel optical post and the scattered light is collected using a fiber-optic cable cou- 1030 pled to an Ocean Optics HR 2000 spectrometer. The spectrometer is pre-calibrated 1031 using 50 wavelengths in the 400–850 nm range from the output of a neon discharge 1032 lamp source. The spectrometer is also intensity-corrected over this range using a 1033 black body source. The estimated error in the resolution of the device is about 0.1 1034 nm (1 Å). 1035

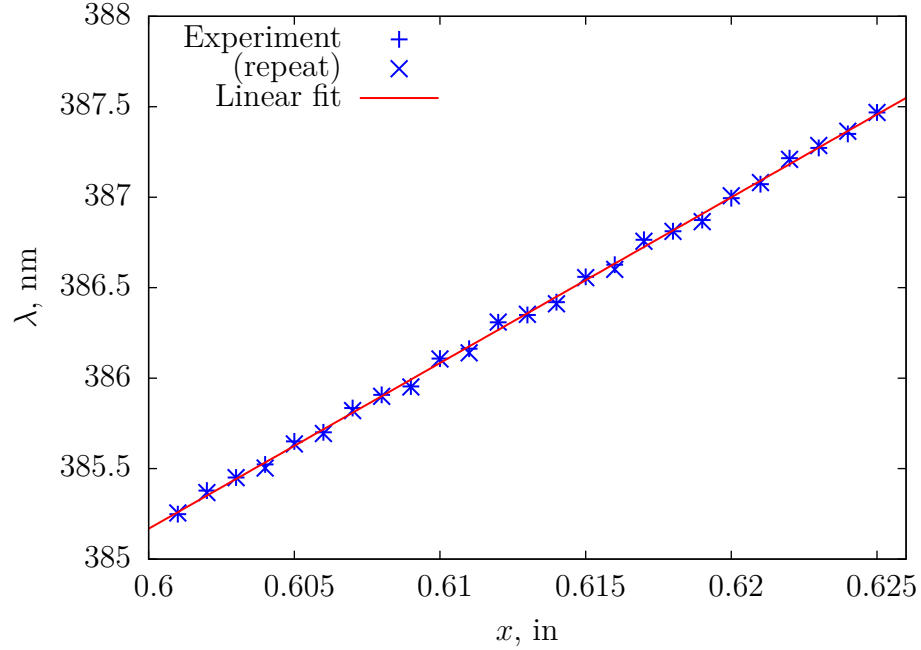


Figure 3.9: The wavelength of the second harmonic beam of the laser is plotted above against the tuner position( $x$ ). The data shows excellent repeatability and falls on a linear trend. The equation for the linear curve fit is  $\lambda = 330.213 + 91.5908x$ , where the units of  $\lambda$  and  $x$  are nm and in, respectively.

The laser micrometer is traversed from 0.600 in to 0.625 in in steps of 0.001 in. 1036  
The experiment is repeated by traversing the micrometer from 0.625 in back to 0.600 1037  
in along the same points to ensure repeatability and estimate the variation due to 1038  
hysteresis. The calibration is performed using at the fundamental wavelength of the 1039  
laser as the second harmonic wavelength falls outside the spectrometer's range. Each 1040  
spectrum recorded is integrated over 512 ms and averaged over 10 such acquisitions. 1041  
The background-corrected peak of the spectrum is then modeled as a Gaussian and 1042  
the location of the center of the Gaussian waveform is recorded. 1043

The results from this experiment are shown in Figure 3.9. The plot demonstrates 1044  
that the variation of the second harmonic wavelength (obtained by halving the fun- 1045  
damental wavelength) with the position of the tuner micrometer is linear. Further, 1046  
there is little difference between the measurements taken while increasing and de- 1047  
creasing the micrometer position. This indicates that any effects of hysteresis in the 1048



micrometer position are minimal. The calibration equation relating the micrometer 1049  
position to the output wavelength is obtained by applying a linear curve fit to the 1050  
data points on the graph as shown in Figure 3.9. 1051

## CHAPTER 4

1052

### CH PLIF SIGNAL MODELING AND VALIDATION

1053

This chapter deals with the evaluation of CH PLIF as a diagnostic technique. Preliminary experiments to evaluate the optimal use of the CH PLIF imaging system are detailed. This is followed by a discussion of some detailed aspects of modeling the LIF signal. The results of applying the model to a reference laminar flame are compared with experimental results. Finally, the model is used to predict the feasibility of using CH PLIF to study various hydrocarbon flames.

1054

1055

1056

1057

1058

1059

#### 4.1 CH PLIF Preliminary Experiments

1060

The CH PLIF imaging system was evaluated for use in imaging hydrocarbon flames by performing three preliminary experiments. First, an excitation scan was performed to confirm the location of the optimal wavelength to excite the CH radicals in a typical hydrocarbon flame. Second, a test of the linearity of the LIF signal with respect to the incident laser intensity was performed. Finally, a spectrum of the LIF emission was recorded and compared to calculations. The setup and results of these experiments are described in the following subsections.

1061

1062

1063

1064

1065

1066

1067

##### 4.1.1 Excitation Scan

1068

An excitation scan is performed by tuning the output of the alexandrite laser from  $\lambda = 387.077$  nm to 387.260 nm. This serves two purposes. First, it locates the optimal wavelength to excite the CH radicals that results in the highest fluorescence yield. Second, the variation of the signal intensity can be compared with simulated profiles from LIFBASE or other spectroscopic calculations and our estimation of the laser

1069

1070

1071

1072

1073

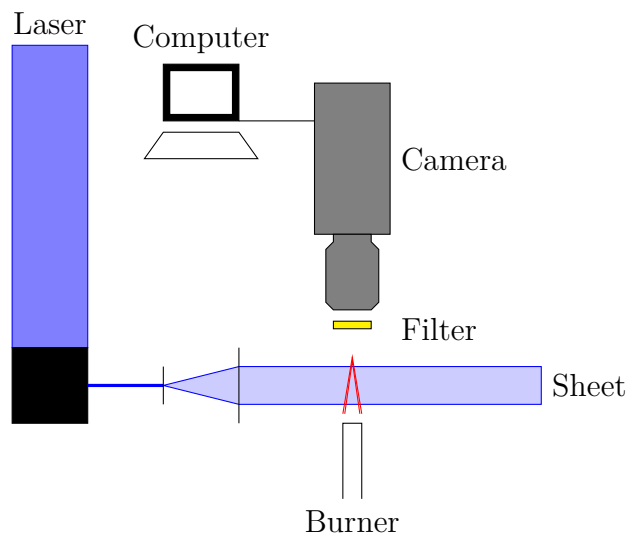


Figure 4.1: The figure above shows the schematic of the excitation scan experiment. A collimating pair of lenses form the laser beam into a sheet focused over a laminar Bunsen burner. The fluorescence is imaged perpendicularly by an intensified camera synchronized to the laser pulse. A 3 mm GG 420 filter is used to reject elastic scattering.

linewidth can be validated. The laser linewidth is an integral parameter and appears  
in the absorption integral used by the models developed in Chapter 2.

A schematic of the excitation scan experiment is shown in Figure 4.1. The intensified PI Acton 512×512 camera described in Section 3.2.2 is used to image a premixed, laminar methane-air flame operating at close to stoichiometric conditions. The laminar flame is stabilized on the Bunsen burner described in Section 3.2.3.2. The alexandrite laser is operated at a power of 16 mJ/pulse in the second harmonic. The sheet forming optics consist of a +50 mm cylindrical lens and a +250 mm spherical lens placed 300 mm apart. The optics form the beam into a collimated sheet about 25 mm (1 in) tall, focused to a thickness on the order of 250  $\mu\text{m}$  at the flame location. The sheet passes through the center of the flame and the edges of the sheet are blocked by razor blades to prevent reflections from the burner from saturating the camera.

The induced fluorescence in the flame sheet is imaged perpendicularly by the intensified camera using an 85 mm f/1.8 Nikon AF Nikkor lens. A 3 mm thick 50

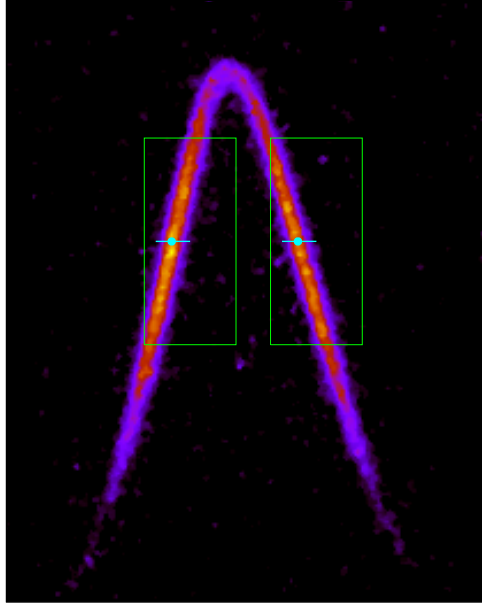


Figure 4.2: The image above shows a typical instantaneous laminar flame from the excitation scan experiment. Regions of interest are identified on the image corresponding to the window method (green) and the line method (cyan). The midpoint of the flame sheet is also indicated on the image.

mm×50 mm square GG 420 Schott glass filter is used to reject elastic scattering 1089  
at the excitation wavelength. This setup gives a magnification of approximately 62 1090  
 $\mu\text{m}/\text{pixel}$ . The camera is triggered by the flash lamp sync signal from the laser sys- 1091  
tem and the intensifier is gated over 300 ns, encompassing the 70 ns laser pulse. The 1092  
long gate width gives the intensifier enough time to prepare to receive the fluores- 1093  
cence, preventing signal loss due to iris-ing. The gate width is still short enough that 1094  
minimal flame chemiluminescence or ambient lighting is recorded in the images. 100 1095  
instantaneous images are acquired for each excitation wavelength to acquire a good 1096  
estimate of the mean fluorescence signal,  $\mu_{sig}$ . 1097

Figure 4.2 shows a sample CH PLIF image from this dataset. The images are 1098  
background-corrected by subtracting the laser scattering (recorded without the flame). 1099  
The fluorescence signal is calculated from these images using three alternate ap- 1100  
proaches. 1101

In Method I, two windows are identified that include the straight sections of the laminar flame. The average fluorescence signal in each frame is calculated by taking the average of all the emitting pixels in the two windows. A pixel is designated as an emitting pixel if its intensity exceeds the standard deviation of a typical background pixel by at least a factor of five. The average of this value over all the frames is designated as the mean fluorescence signal,  $\mu_{sig}$ . In Method II, the intensity of the pixels is integrated over a straight line connecting the inner and outer edges of the flame. The straight line is chosen along the beam so that the beam intensity does not vary along the integration path. The integration is performed on the left and right arms of the flame, giving two readings per frame. The mean of these values over all the frames is recorded as the mean fluorescence signal,  $\mu_{sig}$ . In Method III, the midpoints of the flame along the straight lines from Method II are located and the average of their intensities, over all the frames is recorded as the mean fluorescence signal,  $\mu_{sig}$ . The regions of interest for each of these methods are highlighted in Figure 4.2.

The result of this investigation is shown in Figure 4.3. The calculated mean fluorescence signals from the three methods are plotted against a LIFBASE simulation of the absorption spectrum of the CH  $B-X$  transition. The profiles are appropriately scaled to match the LIFBASE simulation at the maximum value and at the minimum value. The LIFBASE simulation is performed for a thermalized system at 1800 K, at atmospheric pressure. Further, the instrument linewidth is specified to be the same as our estimate of the laser linewidth (1.06 Å).

The line and midpoint methods use fewer pixels to calculate the mean and show minor deviations from the predicted results. The window method uses more pixels and shows much smoother agreement with the simulated profile. In general, the agreement between the measurements and the calculations is excellent. The agreement is in fact so good that a minor adjustment to the calibration of the laser wavelength could be

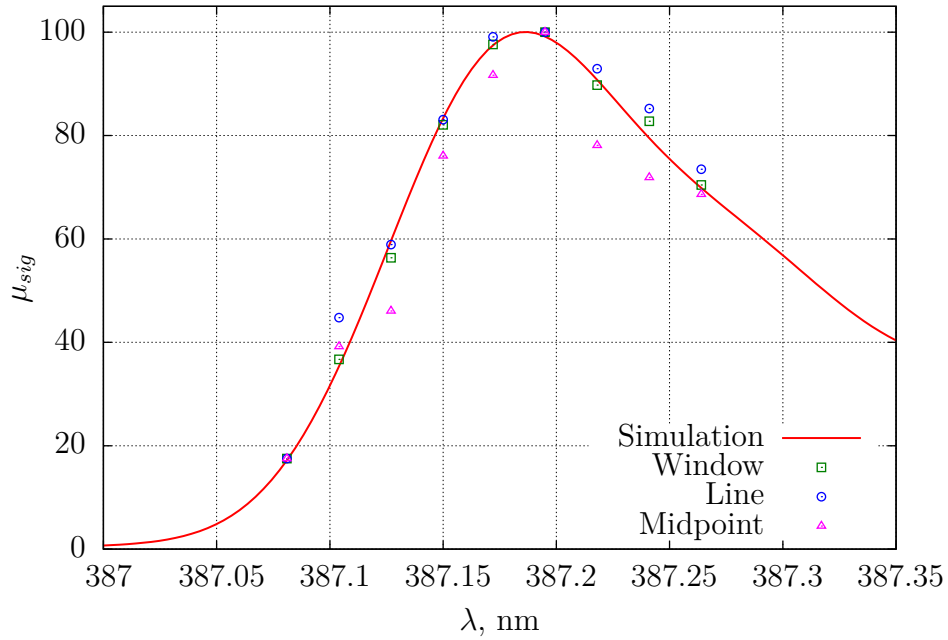


Figure 4.3: The plot above shows the mean signal level of an emitting pixel determined by three separate analysis methods. They are compared to a simulated excitation scan from LIFBASE.

made using these results.

The results indicate that the optimal excitation wavelength, corresponding to the highest mean fluorescence signal, is about 387.2 nm. For the rest of the experiments performed in this work, the laser is operated at this wavelength. The results also help fine tune the calibration of the micrometer over this small region of the spectrum. Finally, the results validate that our estimated laser linewidth, 1.06 Å, is accurate. This value can now be used in subsequent calculations of the LIF signal levels.

#### 4.1.2 Linearity Test

As explained in Chapter 2, the variation of the fluorescence signal with the excitation laser intensity exhibits a saturation curve. For reasons mentioned in that discussion, we prefer to operate in the weak excitation limit where the fluorescence signal scales linearly with the input laser energy. Further, the models developed in Section 2.2 use fluorescence yield expressions that are only valid in the linear regime. Hence, an

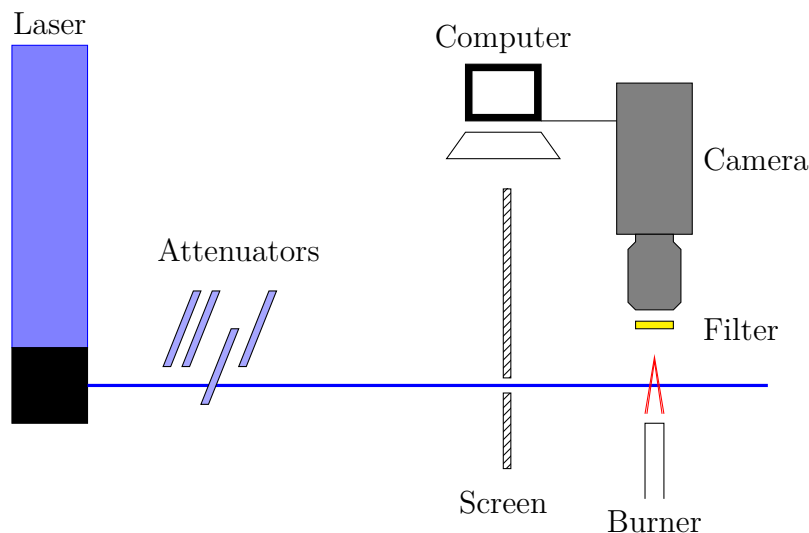


Figure 4.4: A schematic of the experimental setup used to perform the linearity experiment is shown. An unrefracted beam from the laser is directed at a laminar flame and imaged perpendicularly. The beam energy is progressively attenuated by introducing multiple quartz blocks and disks. The drift in the beam is minimized by using attenuating elements in pairs so that any beam deviation is compensated.

experiment is performed to verify the linearity of the system response at the intensities 1142  
at which the flames are imaged for this work. 1143

The schematic of the setup is shown in Figure 4.4. The laser is tuned to the 1144  
optimal wavelength as determined in Section 4.1.1, and operated at 10 Hz. The 1145  
frequency-doubled beam is directed at a steady, laminar, methane-air Bunsen flame 1146  
operating at a slightly rich stoichiometry. The edges of the beam are clipped by 1147  
an aperture to produce a sharp edge and to avoid unnecessary reflections from the 1148  
burner. No optics are used to refract the beam in any way. 1149

The flame is imaged by the PI Acton 512×512 intensified camera equipped with a 1150  
50 mm, f/1.8 AF Nikkor lens. Elastic scattering is attenuated by a 3 mm thick GG 420 1151  
Schott glass filter. The magnification achieved by this set up is about 44  $\mu\text{m}/\text{pixel}$ . 1152  
The LIF signal from the flame is recorded in 300 ns gates and accumulated 150 times 1153  
before being read out. For each case, a corresponding laser scattering image is also 1154  
recorded for estimating the background. The flame chemiluminescence and ambient 1155  
background are also recorded for the same purpose. 1156

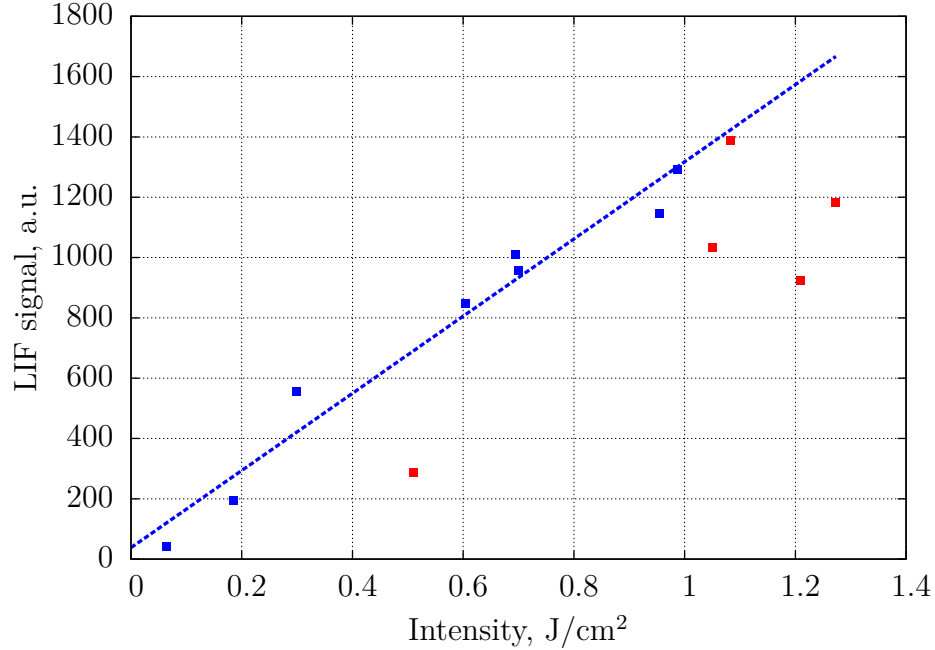


Figure 4.5: The plot above shows the results of the linearity experiment. The LIF signal intensity is measured for a range of input laser energies (expressed here as an intensity). The data points below 1 J/cm<sup>2</sup> are marked in blue and fitted to a linear curve. One outlier (red), along with data points at high laser intensities are not included in the linear fit.

For this experiment, varying the intensity of the laser beam by changing the flash lamp voltage or even the Q-switch timing is not preferred as either would alter the pulse width of the beam. Instead, beam intensity attenuators—quartz disks and blocks of varying thickness—are introduced into the beam to produce an intensity loss, while preserving all other characteristics of the beam. The quartz elements decrease the intensity of the laser beam through reflection, scattering and absorption. The stray reflections and scattering from the quartz elements are kept from contaminating the flame image by using a screen. In this manner, the laser power is varied from 10 mJ/pulse to 0.5 mJ/pulse and back.

The acquired images are background-corrected and the intensity is conditionally averaged over pixels with a non-zero intensity in the region where the fluorescence occurs. The average fluorescence intensity values thus obtained are plotted against the corresponding laser intensity and shown in Figure 4.5.



The LIF signal is observed to increase monotonically with increasing laser intensity. At the lower intensities, the variation is very nearly linear, with marginal scatter and only one significant outlier. At intensities above  $1 \text{ J/cm}^2$  however, there is significant scatter in the data and any linear trends from the low intensity cases cannot be reliably extended over this region. Figure 4.5 shows a linear fit over the low intensity points that indicates that as long as the intensity of the laser sheet is kept below  $1 \text{ J/cm}^2$ , the assumption of operating in the linear regime is valid. All CH PLIF images that were acquired for this study were acquired at laser intensities below this threshold.

#### 4.1.3 LIF Emission Spectrum

The CH LIF spectrum is recorded experimentally. This serves two purposes. First, by verifying that the recorded spectrum matches the calculated one from LIFBASE, we can be reasonably sure of the source of the emission. Second, other sources of emission of comparable or greater intensity, if any, can be located on the spectrum. If such sources are discovered, they need to be blocked using filters.

The experiment is again performed on the laminar flame set up, operating a methane-air flame at an equivalence ratio slightly richer than stoichiometry. The CH layer in the laminar flame is excited by an unrefracted beam from the alexandrite laser. The resulting emissions are collected using a fiber optic cable. No filter is used to block any wavelengths for this experiment. The fiber optic cable is aligned with a  $100 \text{ }\mu\text{m}$  wide slit of a 0.3 m, f/4 SpectraPro 300i spectrometer which separates the light into its spectrum using a 600 lines/mm grating. The spectrum is imaged using the PI-MAX  $512 \times 512$  camera and accumulated over 1000 gates of 300 ns each. The flame chemiluminescence background collected using identical gates is found to be negligible.

The portion of the measured spectrum is shown in Figure 4.6. The simulated

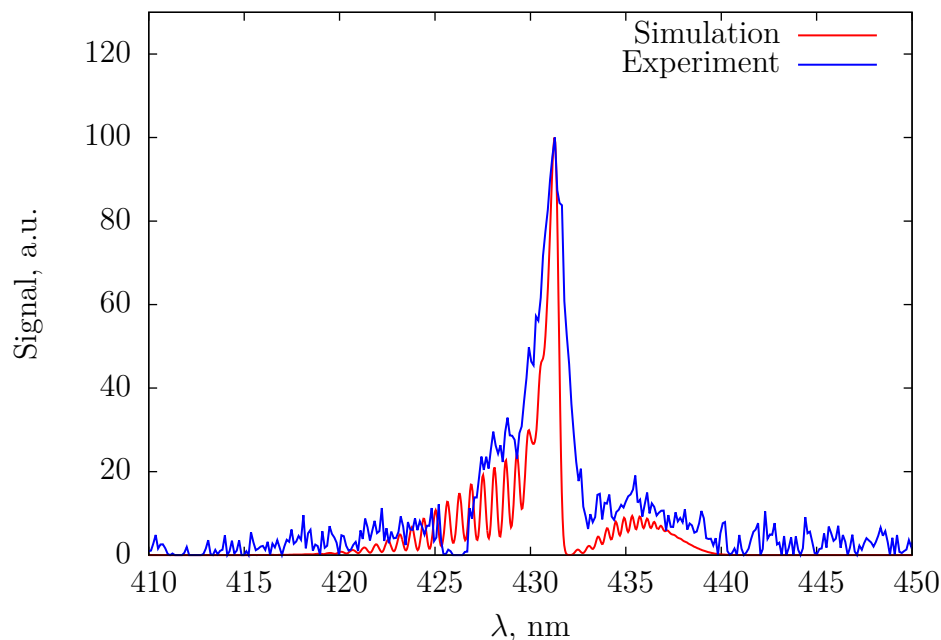


Figure 4.6: The plot above shows the experimentally measured spectrum of the LIF emission (blue) from a Bunsen flame averaged over 1000 exposures. This is compared to a simulated LIF emission spectrum (red) generated by LIFBASE.

spectrum is from LIFBASE for a 1 atm, thermalized CH system at 1800 K. The reso- 1196  
 lution of the simulation is set to match that of the spectrometer (about 0.3 nm). The 1197  
 peaks agree well with the simulated result. Further, no other emissions of comparable 1198  
 intensity are found up to 520 nm. 1199

## 4.2 Fluorescence Signal Modeling 1200

Chapter 2 presented analysis of LIF signal calculation as a function of thermodynamic 1201  
 conditions and the local composition in a flame. Expressions derived using a basic 1202  
 model (Equation 2.14) and a more complex model (Equation 2.27) were presented. 1203  
 The expressions rely on knowledge of several physical values and specific spectroscopic 1204  
 constants pertaining to the CH system. This section lists several of these constants 1205  
 along with further simplifications that need to be made in order to computationally 1206  
 evaluate the predicted signal through a flame. 1207

Table 4.1: *The coefficients of spontaneous emission for transitions in the CH system are provided.*

Transition	Symbol	A, s <sup>-1</sup>
$B^2\Sigma^- \rightarrow X^2\Pi(0, 0)$	$A_{20}$	$2.963 \times 10^6$
$A^2\Delta \rightarrow X^2\Pi(1, 1)$	$A_{10}$	$1.676 \times 10^6$
$A^2\Delta \rightarrow X^2\Pi(0, 0)$	$A'_{10}$	$1.832 \times 10^6$

#### 4.2.1 Fluorescence Yield

1208

The fluorescence yield expressions in Equations 2.21–2.22 are in terms of the Einstein 1209  
coefficients of spontaneous emission,  $A_{ij}$  and the rates of collisional quenching,  $Q_{ij}$ . 1210  
The values for the Einstein spontaneous emission coefficients used in this study are 1211  
collated from literature[68, 74] and tabulated in Table 4.1. 1212

The quenching rates between various energy levels are harder to calculate. As 1213  
shown in Equation 2.9, the rates calculated as a function of the local composi- 1214  
tion, thermodynamic conditions and the quenching cross-section,  $\sigma_i$ , of the colliding 1215  
species. CH is a minor species in typical hydrocarbon flames, with its concentration 1216  
rarely exceeding a few ppm. Consequently, most of its collisions will occur with the 1217  
major species in the flame. Thus, it is only required to know the quenching cross- 1218  
sections of major species to estimate the collisional quenching rate within acceptable 1219  
uncertainty. 1220

Quenching cross-sections are typically functions of temperature, but vary little 1221  
with pressure. Several researchers have reported experimentally measured collisional 1222  
cross-sections for many species in hydrocarbon-air flames, modeling their temperature 1223  
dependence over an increasingly wide range of temperatures[64, 67, 74–93] relevant to 1224  
combustion. Of these, the current study uses functional forms for several species in 1225  
methane-air flames from Tamura et al.[91], some of which were updated by Renfro et 1226  
al.[93]. Quenching cross-sections for higher alkanes are taken from Chen et al.[85, 87, 1227

Table 4.2: *The functional form of the quenching cross-sections of various species with CH are provided.*

Species	$\sigma, \text{\AA}^2$
H <sub>2</sub>	$6.1 \exp(-686/T)$
H	$221T^{-0.5} \exp(-686/T)$
O <sub>2</sub>	$8.61 \times 10^{-6} T^{1.64} \exp(867/T)$
OH	$221T^{-0.5} \exp(-686/T)$
H <sub>2</sub> O	9.6
CH <sub>4</sub>	$52.8T^{-0.5} \exp(-84/T)$
CO	8.31
CO <sub>2</sub>	$8.67 \times 10^{-13} T^{3.8} \exp(854/T)$
C <sub>2</sub> H <sub>6</sub>	13.4
N <sub>2</sub>	$1.53 \times 10^{-4} T^{1.23} \exp(-522.1/T)$
C <sub>3</sub> H <sub>8</sub>	22

88] These functional forms are tabulated in Table 4.2.

1228

The fluorescence yield expressions also involve several collisional transfer rates between the energy levels of interest. There have been efforts[65, 94] to measure and/or model these rates, but the energy level models used for these studies is more complicated and cannot be easily reconciled with our model of the CH system. Hence, it is preferable to make some simplifying assumptions so that these collisional transfer rates can be reduced in terms of known quenching rates.

1229

1230

1231

1232

1233

1234

Cool et al.[77] and Garland et al.[64] report that excited CH molecules in the  $B^2\Sigma^-$  electronic state are about 30% more likely to be quenched than molecules in the  $A^2\Delta$  states. The researchers observe that the quenching rates do not vary appreciably over the vibrational manifold. This observation lets us make the following assumptions eliminating  $Q'_{10}$  and  $Q_{20}$  in terms of  $Q_{10}$ .

1235

1236

1237

1238

1239

$$Q'_{10} = Q_{10} = Q$$

$$Q_{20} = 1.3Q \tag{4.1}$$

Next, Garland et al.[64] and later, Luque et al.[67] report that the rate of transfer following the  $B^2\Sigma^- \rightarrow A^2\Delta$  (0,1) transition accounts for almost 24% of the collisional removal of CH from the upper electronic state. This allows us to formulate one more equation as shown below.

$$\begin{aligned} \frac{Q_{21} + Q'_{21} - Q_{12}}{Q_{20} + Q_{21} + Q'_{21} - Q_{12}} &= 0.24 \\ \therefore \frac{Q_{21} + Q'_{21} - Q_{12}}{Q} &= 0.4105 \end{aligned} \quad (4.2)$$

The same authors also report that the collisional transfer from  $B^2\Sigma^-$ ,  $v = 1$  populates the  $A^2\Delta$ ,  $v = 1$  level four times faster than the  $A^2\Delta$ ,  $v = 0$  level.

$$\frac{Q_{21} - Q_{12}}{Q'_{21}} = 4 \quad (4.3)$$

Finally, Garland et al.[64] note that the rate of forward transfer in the  $B^2\Sigma \rightarrow A^2\Delta$  (0,1) transition is about 60% faster than the reverse process.

$$\frac{Q_{21}}{Q_{12}} = 1.6 \quad (4.4)$$

Equations 4.2–4.4 form a closed set of linear equations that can be written out in matrix form and solved. Equation 4.5 presents this solution, eliminating  $Q_{21}$ ,  $Q'_{21}$  and  $Q_{12}$  in terms of  $Q$ .

$$\begin{bmatrix} Q_{21} \\ Q'_{21} \\ Q_{12} \end{bmatrix} = \begin{bmatrix} 0.8758 \\ 0.0821 \\ 0.5474 \end{bmatrix} Q \quad (4.5)$$

Substituting Equations 4.1 and 4.5 into Equations 2.21–2.22 leads to simplified expressions for the two fluorescence yields as shown in Equations 4.6–4.7. More

importantly, they are now functionally dependent on only the Einstein coefficients 1253  
and the rates of collisional quenching from  $A^2\Delta \rightarrow X^2\Pi$ , which are known. 1254

$$Y_1 = \frac{0.8758A_{10}Q}{(A_{10} + 1.5474Q)(A_{20} + 2.2579Q) - 0.4794Q^2} \quad (4.6)$$

$$Y_1' = \frac{0.0821(A_{10} + 1.5474Q)A_{10}'Q}{(A_{10}' + Q)((A_{10} + 1.5474Q)(A_{20} + 2.2579Q) - 0.4794Q^2)} \quad (4.7)$$

The final unknowns are the number densities of the major species in the flame 1255  
zone. The profile of the local mole fraction of the various species through a 1-D, 1256  
freely propagating, laminar flame can be obtained from Chemkin calculations using 1257  
the Flame-Speed Calculator reactor model. Results presented in this chapter cover 1258  
laminar flames burning a range of reactant mixtures at various inlet conditions. Ad- 1259  
ditional results are presented for strained, laminar, methane-air flames which are 1260  
calculated using the Opposed flow flame reactor model. 1261

The Chemkin results provide mole fractions and thermodynamic conditions, which 1262  
can be used to solve for the number density using the following equation. 1263

$$n_i = \frac{pN_A X_i}{RT} \quad (4.8)$$

In Equation 4.8,  $N_A$  is Avogadro's number,  $X_i$  is the mole fraction of species  $i$ ,  $R$  1264  
is the universal gas constant and  $p$ ,  $T$  are the local pressure and temperature in the 1265  
flame. 1266

## 4.2.2 Absorption Integral 1267

The absorption term in Equation 2.27 requires us to calculate the Boltzmann fractions 1268  
for the energy levels involved and the absorption integral over each transition line 1269  
being excited by the laser. First, we focus on the Boltzmann fraction expression 1270  
from Equation 2.24. The vibration energy expression from Equation 2.25 needs the 1271

Table 4.3: Spectroscopic constants for the CH  $X^2\Pi$  state are presented.

Constant	Value, $\text{cm}^{-1}$
$\omega_e$	2860.7508
$\omega_e x_e$	64.4387
$\omega_e y_e$	0.36345
$\omega_e z_e$	$-1.5378 \times 10^{-2}$
$B_e$	14.459883
$\alpha_e$	0.536541
$D_e$	$1.47436 \times 10^{-3}$
$\beta_e$	$-2.530 \times 10^{-5}$

spectroscopic constants  $\omega_e$ ,  $\omega_e x_e$ ,  $\omega_e y_e$  and  $\omega_e z_e$ . Simultaneously, the expression for  
the rotational energy in Equation 2.26 requires knowing  $B_e$ ,  $\alpha_e$ ,  $D_e$  and  $\beta_e$  values for  
the levels being excited. Accurate values of these constants for the  $X^2\Pi$  state are  
tabulated in Zachwieja's[95] paper. These are tabulated in Table 4.3.

Next, we discuss the calculation of the absorption integral, which requires the  
following;

- line positions in the  $B^2\Sigma^- \leftarrow X^2\Pi$  (0,0) transition that are being excited by  
the laser,
- Einstein coefficients for stimulated absorption for these transitions,
- Laser center wavelength,
- Laser line shape, and
- Absorption line shapes for each of the excited transitions

The line positions in the R-branch of the  $B^2\Sigma^- \leftarrow X^2\Pi$  (0,0) transition along  
with the respective Einstein B-coefficients are obtained from LIFBASE's database  
and are tabulated in Table 4.4.

The linewidth of the alexandrite laser is of the order of a few wavenumbers and its  
line shape,  $\psi(\nu)$ , can be approximated by a Gaussian profile without loss of generality.

Table 4.4: *The line positions and the corresponding Einstein coefficients for stimulated absorption for transitions in the  $B^2\Sigma^- \leftarrow X^2\Pi$  (0,0) R branch are presented below.*

$N''$	$J_1''$	$\nu_1$ $\text{cm}^{-1}$	$B \times 10^{-9}$ $\text{m}^2\text{J}^{-1}\text{s}^{-1}$	$J_2''$	$\nu_2$ $\text{cm}^{-1}$	$B \times 10^{-9}$ $\text{m}^2\text{J}^{-1}\text{s}^{-1}$
1	0.5	25756.08	6.511	1.5	25774.03	5.823
2	1.5	25776.42	7.225	2.5	25782.72	6.489
3	2.5	25792.74	7.532	3.5	25797.06	7.174
4	3.5	25805.42	7.671	4.5	25808.75	7.460
5	4.5	25814.47	7.719	5.5	25817.20	7.581
6	5.5	25819.80	7.708	6.5	25822.13	7.610
7	6.5	25821.28	7.652	7.5	25823.32	7.581
8	7.5	25818.72	7.561	8.5	25820.55	7.506
9	8.5	25811.93	7.439	9.5	25813.59	7.396
10	9.5	25800.64	7.288	10.5	25802.17	7.254
11	10.5	25784.57	7.111	11.5	25785.98	7.083
12	11.5	25763.38	6.907	12.5	25764.70	6.884
13	12.5	25736.65	6.676	13.5	25737.88	6.657
14	13.5	25703.90	6.418	14.5	25705.06	6.402
15	14.5	25664.54	6.129	15.5	25665.64	6.116
16	15.5	25617.87	5.815	16.5	25618.92	5.804
17	16.5	25563.03	5.472	17.5	25564.03	5.463
18	17.5	25499.00	5.101	18.5	25499.95	5.094
19	18.5	25424.52	4.624	19.5	25425.42	4.618
20	19.5	25338.08	4.161	20.5	25338.93	4.156
21	20.5	25237.84	3.674	21.5	25238.64	3.670
22	21.5	25121.60	3.183	22.5	25122.36	3.180



As a result, the effect of line broadening mechanisms such as natural broadening, 1289  
 inhomogeneous broadening, etc that are commonly encountered in solid state lasers 1290  
 are negligible in comparison and do not affect the line shape appreciably. 1291

$$\psi(\nu) = \frac{1}{\sigma_l \sqrt{2\pi}} \exp\left(-\frac{(\nu - \nu_l)^2}{2\sigma_l^2}\right) \quad (4.9)$$

The mean of the line shape profile,  $\nu_l$ , is set by tuning the center wavelength of 1292  
 the laser. The Full Width at Half Max (FWHM) of the laser,  $\Delta\nu_l$ , is known to us 1293  
 and can be used to calculate the standard deviation of the Gaussian as follows. 1294

$$\sigma_l = \frac{\Delta\nu_l}{2\sqrt{2\ln 2}} \quad (4.10)$$

The line shape of the absorption line being excited, on the other hand, is primar- 1295  
 ily dictated by mechanisms associated with gas-phase media—collisional broadening 1296  
 and Doppler broadening being the most important ones. Collisional broadening is 1297  
 a homogeneous mechanism and produces a Lorentzian broadened line shape. The 1298  
 FWHM of the Lorentzian profile is related to the thermodynamic conditions by the 1299  
 following empirical formula. 1300

$$\Delta\nu_c = 0.1 \left(\frac{p}{p_0}\right) \left(\frac{T_0}{T}\right)^{0.6} \quad (4.11)$$

In Equation 4.11,  $p_0$  and  $T_0$  represent standard conditions of pressure and tem- 1301  
 perature (101325 Pa and 300 K) respectively. By contrast, Doppler broadening is an 1302  
 inhomogeneous mechanism that results in a Gaussian line shape. Its effect depends 1303  
 on the frequency (wavenumber) of the line being broadened,  $\nu_a$ , and on the molecule's 1304  
 velocity. The FWHM of the resulting broadened line shape is given by, 1305

$$\Delta\nu_d = \nu_a \frac{\sqrt{\ln 2}}{c} \sqrt{\frac{8kT}{m_{CH}}} \quad (4.12)$$

The combined effect of these two broadening mechanisms can be calculated by convoluting the two broadened line shapes. In this case, a Lorentzian convoluted with a Gaussian results in a Voigt profile. The computational expense of the convolution that needs to be performed for each absorption line at each point along the flame is prohibitively high. Further, the absorption integral needs to be evaluated by multiplying the Voigt profile with the Gaussian profile of the laser. In order to simplify this without losing too much accuracy, we replace the collision broadened Lorentzian with a Gaussian of equal FWHM. The convoluted profile is now a Gaussian, too and the product of two Gaussians can be easily integrated to get the absorption integral.

The limits of this assumption leading to replacing the Voigt profile with a Gaussian profile need to be stated. If the dominant broadening mechanism were Doppler broadening, the resulting Voigt profile would approximate a Gaussian much closer. However, in combustion systems, particularly at pressure, the dominant line broadening mechanism is in fact, collisional broadening. Hence, the resulting Voigt shape is expected to be much closer to a Lorentzian shape. Lorentzian profiles differ from Gaussian profiles by having a shorter peak and relatively more area in the “wings” of the curve. In the absorption integral, this would lead to increased absorption of the laser energy by transitions near the edge of the laser line shape. Fortunately, when the laser line position is tuned to optimally excite the R-bandhead spanning the lines  $N'' = 5$  to  $N'' = 9$ , the next nearest transition ( $N'' = 4$ ) is far enough away that even with increased absorption, contribution from these lines remains insignificant even at very high pressures.

Returning to the calculation of the absorption integral, we now replace the collision-broadened Lorentzian profile by a Gaussian profile with the same FWHM. Now, the convolution of the collision-broadened and Doppler-broadened line shapes results in

another Gaussian with the same mean and a new FWHM given by,

1331

$$\Delta\nu_a = \sqrt{\Delta\nu_c^2 + \Delta\nu_d^2} \quad (4.13)$$

Thus, the Gaussian line shape of the broadened absorption line can be written as, 1332

$$\phi(\nu) = \frac{1}{\sigma_a \sqrt{2\pi}} \exp\left(-\frac{(\nu - \nu_a)^2}{2\sigma_a^2}\right) \quad (4.14)$$

In Equation 4.14,  $\nu_a$  is the frequency (wavenumber) of the absorption peak being 1333  
excited. The standard deviation of the lineshape,  $\sigma_a$ , is related to the broadened 1334  
FWHM,  $\Delta\nu_a$ , by the following equation. 1335

$$\sigma_a = \frac{\Delta\nu_a}{2\sqrt{2\ln 2}} \quad (4.15)$$

With the above information, the integral in Equation 2.23 can be solved analyti- 1336  
cally as follows. 1337

$$\int \psi(\nu)\phi(\nu)d\nu = \frac{1}{\sqrt{2\pi(\sigma_a^2 + \sigma_l^2)}} \exp\left(-\frac{(\nu_l - \nu_a)^2}{2(\sigma_a^2 + \sigma_l^2)}\right) \quad (4.16)$$

Having discussed the means to calculate the absorption integral in a cost-effective 1338  
manner, it is now possible to calculate the optimal laser location that results in the 1339  
highest value of the absorption integral for a given temperature and pressure. The 1340  
resulting value depends on both the pressure and the temperature at the flame. The 1341  
optimal laser wavelength is found to steadily increase with pressure. With temper- 1342  
ature, the value initially decreases, reaching a minimum around 1800 K and then 1343  
increases again. However, these variations are so small (less than 0.0003 nm) over the 1344  
range of temperatures and pressures encountered in combustion that we may opti- 1345  
mize the wavelength using an atmospheric flame and leave it untouched while imaging 1346  
flames at pressure and/or with preheat. 1347

### 4.3 Chemkin modeling

1348

To restate the goals of this exercise, the aim is to predict the intensity of the LIF signal across operating conditions to test the feasibility of using CH PLIF as a technique to visualize the flame sheet in a combustor. While the primary reactant mixture of interest is methane-air, the analysis can be extended to other alkane-air mixtures and even syngase-alkane-air mixtures. The choice of the kinetics model to calculate the species profiles across flames is thus decided by how well it applies to all the reacting mixtures being considered.

1355

GRI Mech is a chemical kinetics mechanism that uses 53 chemical species and 325 reactions to accurately simulate natural gas-air combustion with emphasis on pollutant formation. As CH is a key species in the formation of  $\text{NO}_x$ , several CH data sets are used as optimization targets for fine tuning the mechanism. Berg et al.[96] report that the results agree well near stoichiometry, but are too low for lean flames and too high for rich flames. Since GRI Mech is developed to solve methane-air problems, its applicability to higher-order alkanes is not well validated. As a result, only the methane-air case is solved using GRI Mech in this study.

1363

For specialized application to higher-order combustion, USC's  $\text{C}_1\text{-C}_3$  mechanism builds upon a  $\text{CO-H}_2$  chemistry base and seeks to optimize more than 250 parameters to sufficiently cover  $\text{C}_3$  chemistry, at the expense of decreased accuracy for  $\text{C}_1$  and  $\text{C}_2$  cases. On the other hand, their Syngas mechanism extends GRI Mech to cover  $\text{H}_2\text{-CO}$  mixtures, retaining its limitations for  $\text{C}_3\text{-alkane}$  mixtures. USC also publishes the USC Mech version II which is specifically targeted at  $\text{H}_2\text{-CO-C}_1\text{-C}_4$  compounds that draws upon several models including GRI Mech. It uses 111 species and 784 reactions to model the chemistry, making it computationally expensive to use over a large parametric sweep.

1372

USCD's San Diego Mechanism is designed with a more minimalist intent of sim-

1373

ulating combustion using the least number of species and reaction rate parameters. 1374  
Subsequent updates to the mechanism have extended its applicability to an increas- 1375  
ing number of combustion and detonation processes. The 2011-11-22 release uses 1376  
235 reactions, with additional data available for extending it to cover heptane and 1377  
even JP10 chemistry. Due to its wide applicability, low computational cost and good 1378  
accuracy, most of the results presented in this chapter use this mechanism. 1379

## 4.4 Results 1380

In this section, the CH signal intensity model is used to predict the LIF photon count 1381  
emitted by the flame in a few selected reactant mixtures. 1382

### 4.4.1 Unstrained Laminar Flames 1383

The LIF photon count is related to many parameters in a flame. It is directly de- 1384  
pendent on the temperature profile through a flame, as well as on the concentrations 1385  
of all major species. In order to reduce the complexity of relating the signal to too 1386  
many parameters at once, we restrict our attention to a simple unstrained, laminar 1387  
flame and study LIF signal variation with reactant composition and inlet conditions. 1388

#### 4.4.1.1 Methane-air flames 1389

We begin by validating the predictions from two mechanisms—GRI Mech 3.0 and 1390  
San Diego—against experimental data acquired from a non-preheated, atmospheric, 1391  
methane-air Bunsen flame. The laminar flame setup from Section 3.2.3.2 is used for 1392  
this purpose. The laser beam is formed into a 25 mm tall sheet bisecting the laminar 1393  
flame and is imaged perpendicularly using the intensified PI-MAX 512×512 camera 1394  
with a 50 mm f/1.4 lens. The images are background-corrected and averaged over 1395  
a window encompassing the PLIF signal from the flame sheet. The experiment is 1396

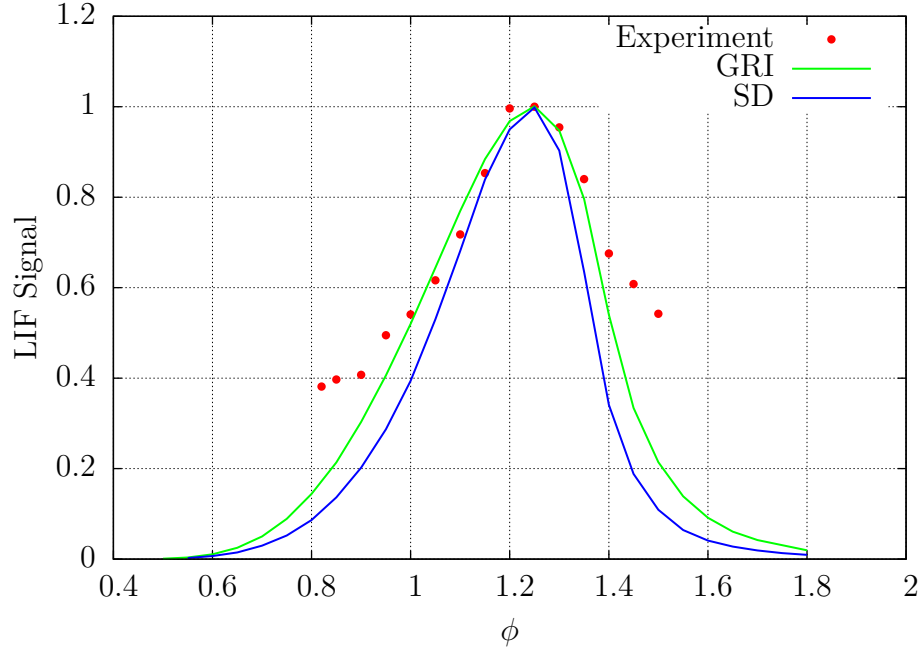


Figure 4.7: The plot above compares the experimentally measured LIF signal to those predicted by the signal model. The experiment is conducted at 1 atm, 300 K on a laminar Bunsen flame burning a methane-air mixture. Two reaction mechanisms are used to generate the relevant data used by the signal model. All three datasets are normalized at the peak value.

repeated over a range of equivalence ratios ranging from 1.55 on the rich side to 0.82  
on the lean side, below which the unpiloted Bunsen flame could not be stabilized.

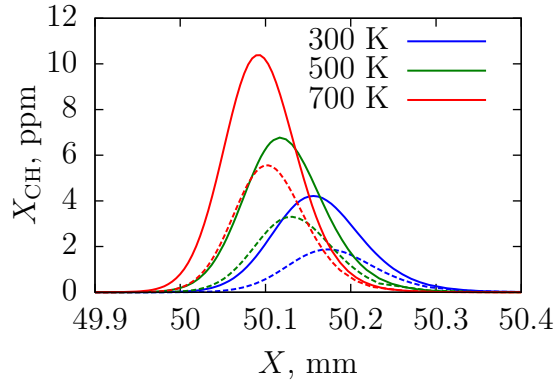
The results are compared to the modeled signal intensity from the GRI Mech and  
San Diego results for a 1-D, freely propagating laminar flame. The three profiles are  
normalized and plotted in Figure 4.7.

The maximum signal predicted by both mechanisms agree with the experimental  
value and is seen to occur at about  $\phi = 1.25$ . Further, both methods predict a  
decrease in the LIF signal as the equivalence ratio increases or decreases away from  
the maximum. This is also in agreement with the experimental results. At the low  
signal levels encountered at both the leanest and richest conditions at which the flame  
is imaged, the experimental results are seen to diverge from the model predictions.  
At these conditions, the models predict a precipitous drop in the signal levels, while

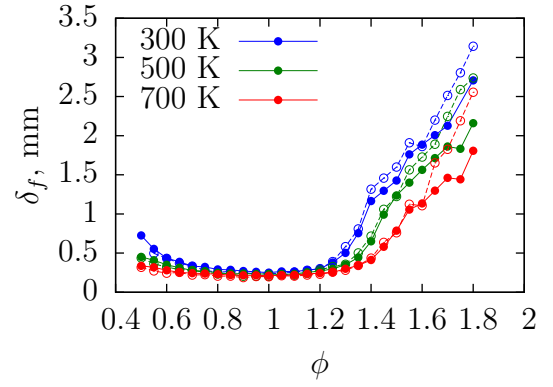
the experimental results show a more gradual drop. This could partly be due to 1409  
insufficient background-correction on the PLIF images, causing the background noise 1410  
to be relatively high compared to the LIF signal. Nevertheless, the systemic profile 1411  
from the experiments agrees with the model predictions. 1412

We then proceed to compare the predictions from the GRI Mech 3.0 and San 1413  
Diego mechanisms for an unstrained, freely propagating, 1-D, methane-air laminar 1414  
flame against each other. Figure 4.8a shows the calculated CH profile across a stoi- 1415  
chiometric flame at atmospheric pressure and three preheat temperatures. At these 1416  
conditions, the San Diego mechanism predicts almost 50% less CH concentration 1417  
compared to the GRI Mech 3.0 mechanism. Both mechanisms predict the increased 1418  
CH concentration at higher preheat conditions, along with the thinning of the flame 1419  
zone. Figure 4.8b shows the flame thickness predicted by the two mechanisms which 1420  
agree quite well, diverging only at rich equivalence ratios. The predicted laminar 1421  
flame speeds and flame temperatures are shown in Figures 4.8c and 4.8d respectively 1422  
and the differences between the two mechanisms are again quite minimal. The re- 1423  
sults of this investigation indicate that other than the nearly consistent discrepancy 1424  
of about 50% in the predicted CH concentration, the results from the two mechanisms 1425  
scale identically. Since we are not concerned with the accurate prediction of the CH 1426  
concentration, but merely the relative variation across conditions, this discrepancy 1427  
will not affect our conclusions. For the rest of the results, calculations are performed 1428  
using only the San Diego mechanism. 1429

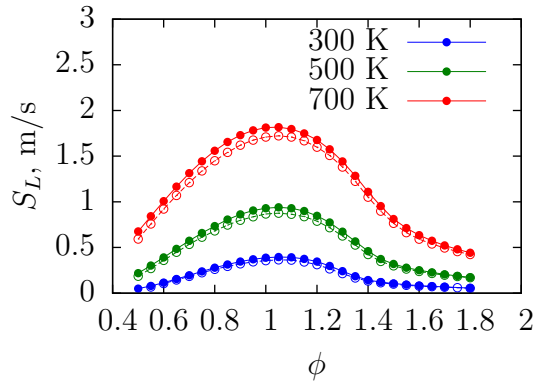
Next, we explore the predicted CH LIF signal intensity variation with pressure 1430  
using the San Diego mechanism. Figure 4.9 shows the predicted signal intensities over 1431  
a range of pressures for a non-preheated case. Since this is the condition at which the 1432  
laminar flame was imaged, the data from the validation experiment is appropriately 1433  
scaled and plotted as well. Two immediate conclusions can be drawn from this plot. 1434  
First, increasing pressure causes the LIF signal to drop rapidly. The drop is so fast 1435



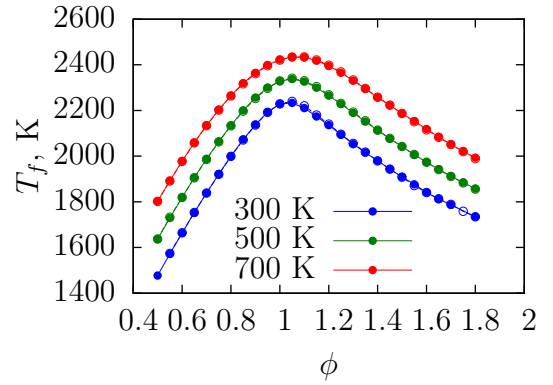
(a) *CH concentration*



(b) *Flame thickness*



(c) *Laminar flame speed*



(d) *Flame temperature*

Figure 4.8: The plots above compares various predicted parameters of an atmospheric pressure, laminar methane-air flame at three preheat temperatures from GRI Mech 3.0 and San Diego mechanisms.



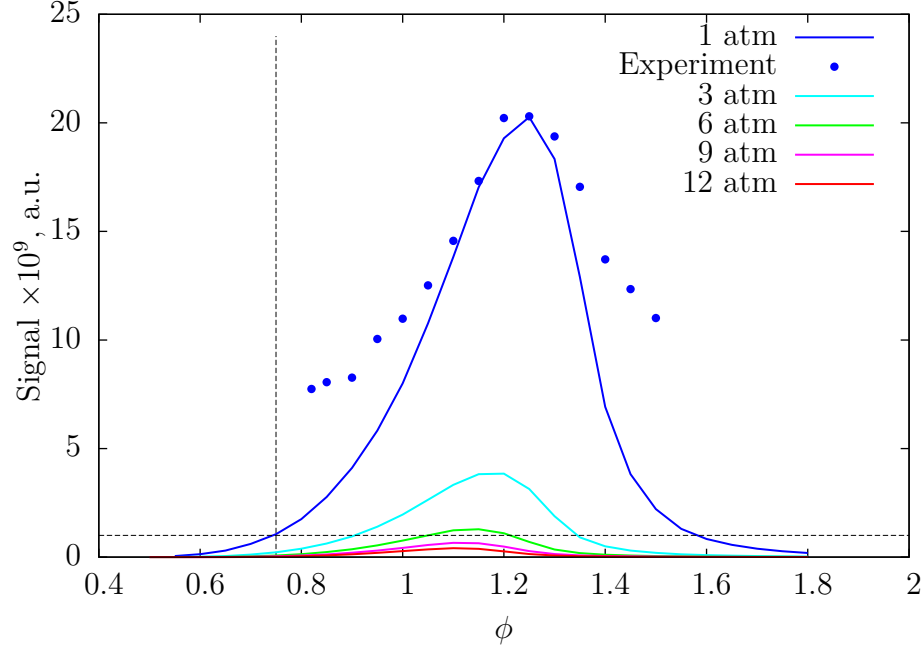


Figure 4.9: The plot above shows calculated LIF signal for non-preheated (300 K) methane-air mixtures over a range of equivalence ratios and pressures. Results from an experiment performed at similar conditions are appropriately scaled and shown.

that linear scale of the Y axis is no longer useful. Second, we can establish a threshold level for the signal based on our validation experiment. Although the flame was still imaged with a reasonable signal-to-noise ratio at the lowest equivalence ratio in the experimental data, it serves as a good indicator for a conservative estimate of the minimum signal level needed. At  $\phi = 0.8$ , the predicted signal count works out to be  $1.75 \times 10^9$ . Based on this, we set the threshold at a value of  $1 \times 10^9$ . Below this threshold, the flame cannot be imaged at all, or with a very poor signal-to-noise ratio that will make post-processing quite difficult. This threshold is indicated on the figure by dashed lines.

Using this threshold, we can reinterpret Figure 4.9. When the pressure is increased to 3 atm, the flame cannot be imaged unless the equivalence ratio is between 0.9–1.3. At 6 atm, the range is even narrower and restricts the feasibility of this experiment to between 1.1–1.2. With no preheat, the flame cannot be imaged at 9 atm and above.

Increasing the preheat temperature to 500 K and plotting using a log scale, Figure

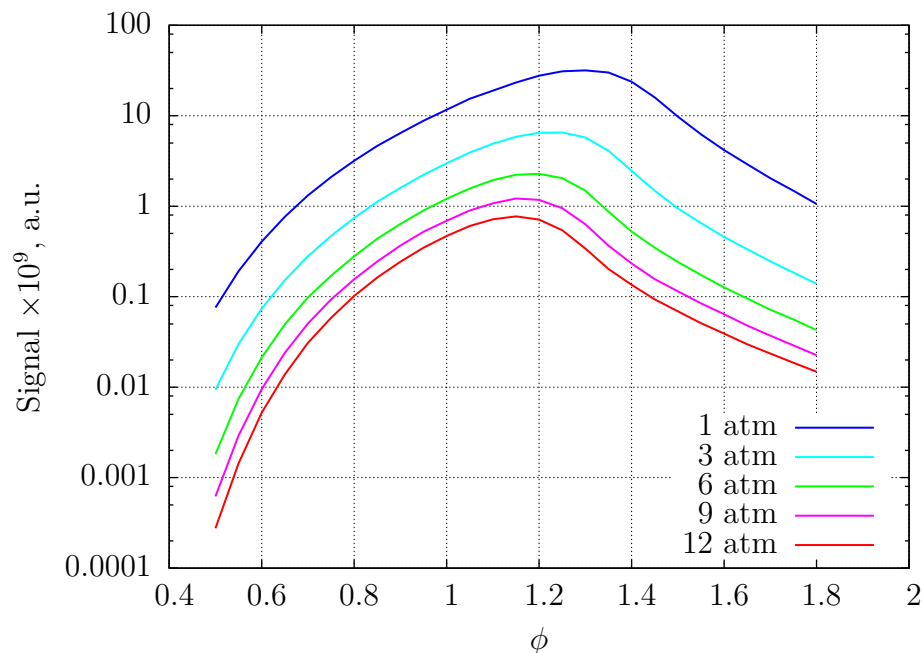


Figure 4.10: The plot above shows calculated signal intensities for a methane-air flame with a preheat of 500 K. The ordinate  $1 \times 10^9$  serves as a minimum threshold to get images with usable signal-to-noise ratios.

4.10 shows the effect of preheat is beneficial to CH PLIF. The range of equivalence ratios at which the flame can be imaged is now broader at all pressures. Lean flames at less than 0.7 can now be imaged at atmospheric pressure. Going up in pressure, post-stoichiometric flames at 9 atm can now be imaged. Simultaneously, the peak signal levels are higher, as well. At atmospheric pressure, the peak signal is nearly 50% higher.

Figure 4.11 shows this plot for a preheat temperature of 700 K. At this high preheat, ultra lean flames with equivalence ratios of 0.6 can be imaged at atmospheric pressure. Beyond 6 atm, the range of applicability of CH PLIF remains poor and is confined only to very rich flames.

#### 4.4.1.2 Higher-order alkane flames

Now, we turn our attention to higher-order alkane-air flames. Our interest in these fuels is motivated by two reasons. First, these are viable fuels in their own right

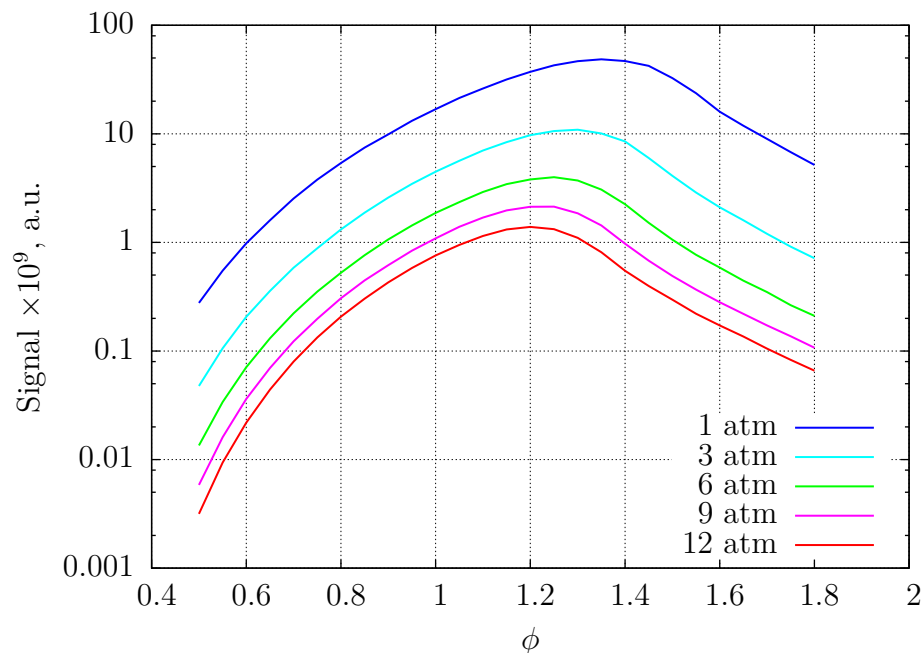


Figure 4.11: This plot shows the calculated signal intensities for methane-air flames with a preheat of 700 K.

and are used in several combustion applications. Since the combustion reactions in these flames also follow a CH pathway, these flames could be imaged using CH PLIF. Second, we are interested in exploring the possibility of using small quantities of these fuels to mix with methane in order to boost the CH LIF signal. This could allow us to acquire flame images at leaner equivalence ratios at high pressure conditions. We will explore this possibility in this section.

We begin by considering the CH LIF signal from pure alkane-air mixtures burning at atmospheric conditions without preheat. Figure 4.12 shows the variation of the LIF signal with equivalence ratio for these mixtures. Again a signal level of  $1 \times 10^9$  serves as a threshold for the feasibility of acquiring CH PLIF images of these flames. We can draw several conclusions from this plot. First, the range of equivalence ratios above the signal threshold is indeed wider for the higher alkanes (compared to methane), but not by much. Particularly, the differences between the three alkanes at the lean equivalence ratios is minimal. Most of the widening occurs at very rich equivalence

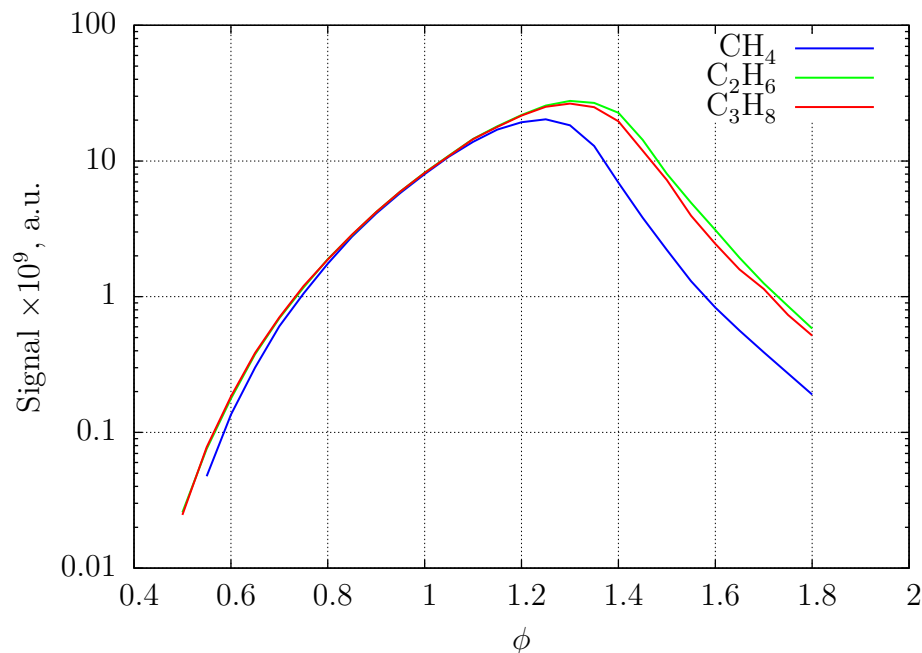


Figure 4.12: The plot above shows the calculated signal intensity from alkane-air flames burning at atmospheric pressure, without preheat (300 K). The ordinate  $1 \times 10^9$  serves as the lower threshold for images with usable signal-to-noise ratios.

ratios. Second, while the peak CH signal did increase when going from methane to ethane, a similar increase is not seen when going from ethane to propane. In fact, the San Diego mechanism actually predicts a slight fall in the peak signal. This lack of increase in the CH signal can be traced to the adiabatic flame temperature. Figure 4.13 plots the adiabatic flame temperature for these mixtures and shows that the increase in the flame temperature going from ethane to propane is minimal. While the CH signal does not correlate with the flame temperature at all conditions, it is strongly affected by it. Hence, the CH signal does not vary appreciably between the higher alkanes.

Since the CH signal in ethane- and propane-air flames are not much different from methane-air flames, adding small amounts of these alkanes should not have a very significant effect on the signal. This is borne out by Figure 4.14 which plots the signal variation for a 700 K preheat, atmospheric flame with and without higher-order alkane doping.

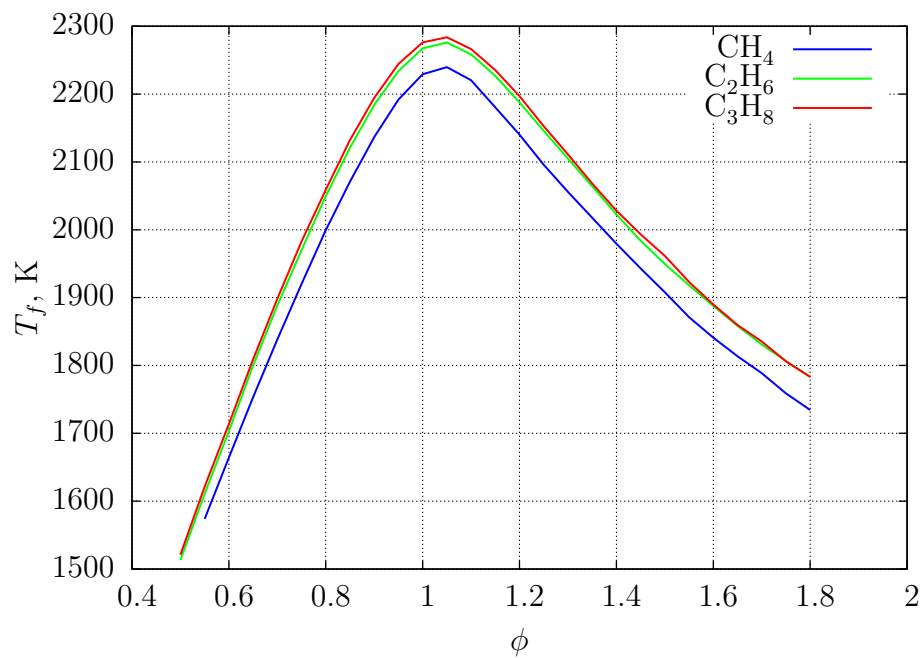


Figure 4.13: The plot above shows the adiabatic flame temperature for alkane-air flames burning at atmospheric pressure, without preheat (300 K).

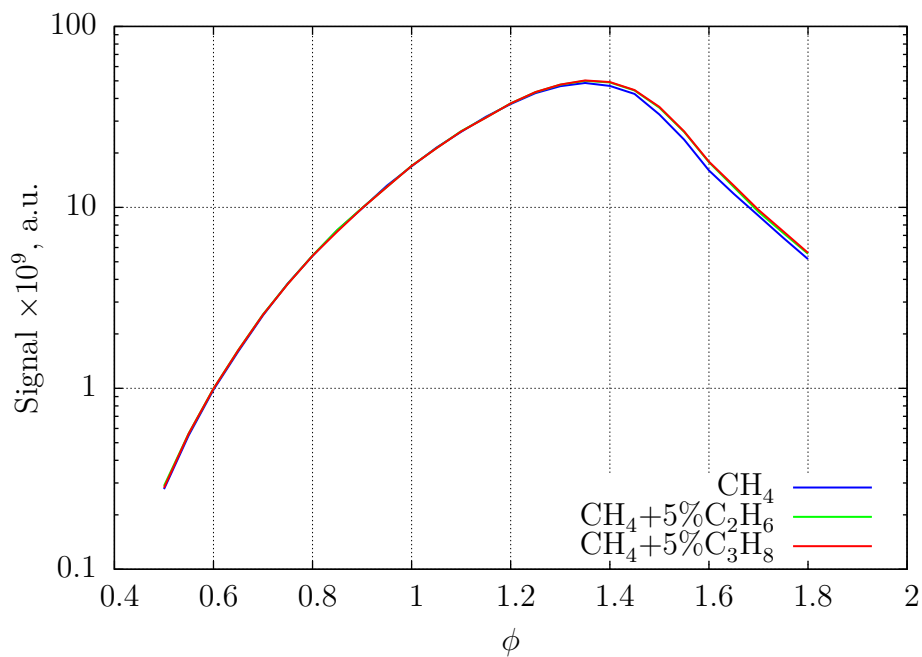


Figure 4.14: The plot shows the effect of adding a small quantity of a higher-order alkane to a methane-air mixture at atmospheric pressure with a preheat of 700 K. The effect of the doping at lean conditions is negligible.

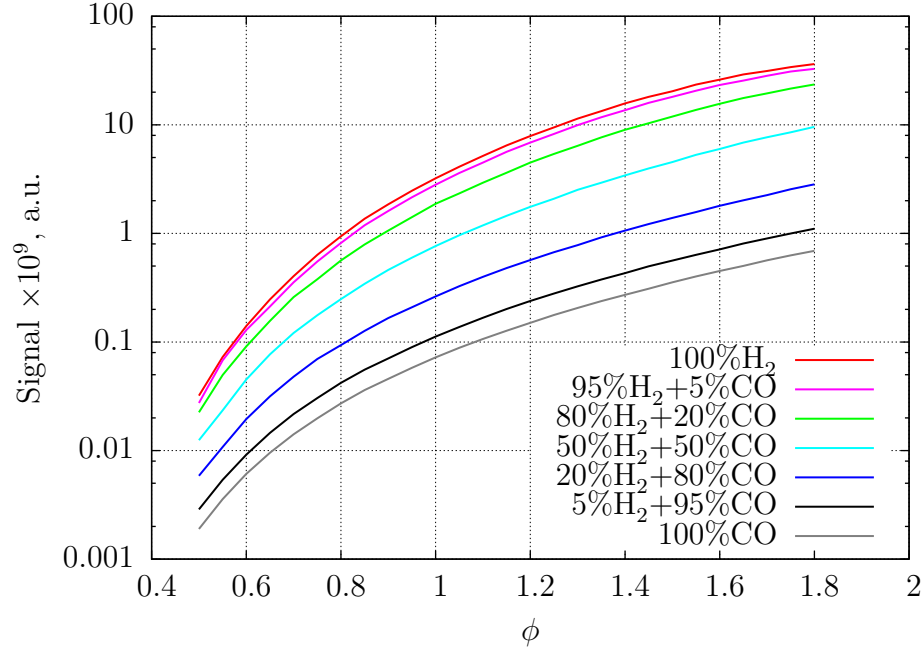


Figure 4.15: The plot above shows the effect of doping various syngas mixtures at atmospheric pressure and no preheat (300 K) with a small amount (5%) of methane. The ordinate  $1 \times 10^9$  serves as the lower threshold for the signal.

#### 4.4.1.3 Syngas flames

Syngas (mixtures of CO and H<sub>2</sub>) does not follow a CH pathway when oxidized in air and hence is unsuitable for investigating with CH PLIF. As a result, most syngas flames are investigated using OH PLIF. However, since syngases are an important emerging class of fuels, it would be interesting to test the feasibility of using CH PLIF if they are doped with a small amount of alkanes to provide a CH pathway.

Figure 4.15 shows the signal levels in various non-preheated, atmospheric pressure syngas mixtures doped with 5% methane. The results are quite promising as they indicate that with a high enough H<sub>2</sub> concentration, syngas flames as lean as 0.8 can be imaged above our signal threshold. Increasing the preheat temperature to 700 K, Figure 4.16 extends this range to an equivalence ratio of 0.6. Using a higher order alkane in place of methane does lower this value further, but not significantly.

While these results do indicate the feasibility of using a spatially precise flame

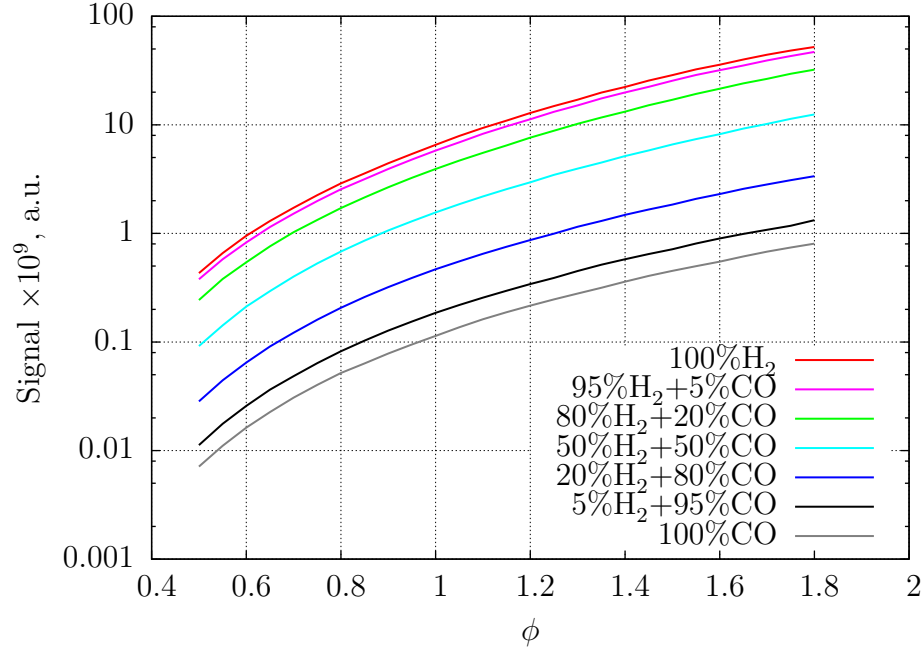


Figure 4.16: The plot above shows the calculated CH LIF signal from various syngas mixtures that have been doped with 5% methane at atmospheric pressure. The reactants have been preheated to 700 K.

imaging technique like CH PLIF to study syngas flames, the addition of a small 1504  
quantity of alkane does substantially change the properties of the flow. While the 1505  
adiabatic flame temperature of pure hydrogen only decreases by 40 K due to the 1506  
methane addition, peak flame speeds are reduced by almost 20%. This limits the 1507  
applicability of CH PLIF to study these flames. 1508

#### 4.4.2 Strained Flames 1509

In order to study the effect of strain rate on the LIF signal, a non-preheated, at- 1510  
mospheric pressure, laminar methane-air flame is simulated in a opposed flow and 1511  
the flow rate is slowly increased till extinction. The separation between the two flow 1512  
inlets in the simulation is 2 cm. The system is solved using the Opposed flow flame 1513  
reactor model in Chemkin. The simulation is carried out for two equivalence ratios 1514  
and the results are plotted in Figure 4.17. 1515

The LIF signal increases slightly due to stretch effects and upon encountering 1516

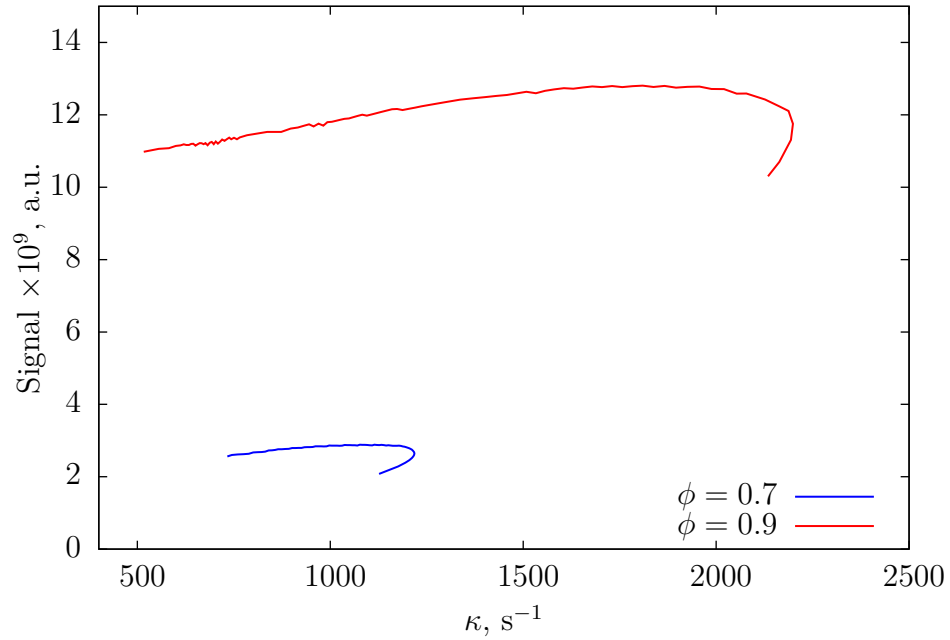


Figure 4.17: The plot above shows the calculated CH LIF signal from a strained, laminar, methane-air flame at atmospheric pressure. The signal is calculated from Chemkin simulations using the Opposed flow flame reactor model.

extinction, decreases, exhibiting hysteresis. This behavior mirrors the variation of the flame temperature for  $Le < 1$  flows where increasing stretch results in an elevated flame temperature.

## 4.5 Summary of Results

The following is a summary of the key results from this chapter.

1. The CH PLIF imaging system is tuned to the optimal wavelength and demonstrated on a simple, laminar Bunsen flame.
2. The details of computing the signal intensity using the signal model from Chapter 2 are explained.
3. The experimental results are compared to modeling results which behave in much the same manner with equivalence ratio.



4. The model is used to study the variation of the LIF signal with pressure, tem- 1528  
perature and equivalence ratio for a host of reactant mixtures. 1529
5. In general, increasing the flame temperature enhances the CH LIF signal, while 1530  
increasing the combustor pressure decreases it. 1531
6. Hydrogen-rich syngas flames can be imaged with CH PLIF if the reactants are 1532  
doped with a small amount of an alkane. However, this also causes noticeable 1533  
changes in the flame speed of the reactant mixture. 1534
7. Strained flames produce a slightly higher LIF signal as long as the strain rate 1535  
is not close to extinction. 1536

## CHAPTER 5

1537

### LSB FLAME CHARACTERISTICS

1538

Chapter 2 introduced the salient features of the LSB flow field and discussed the mechanisms that enable the LSB to stabilize a flame. Four flow parameters were introduced that sufficiently describe an operating condition of the LSB—the combustor pressure,  $p$ , the preheat temperature,  $T$ , the reference velocity,  $U_0$ , and the equivalence ratio of the premixed reactants,  $\phi$ . The angle of the swirler vanes,  $\alpha$ —a geometric parameter—was also identified as a variable of interest. The effect of varying these parameters on the flame characteristics constitutes the subject of this chapter. The LSB flame was characterized by its location, its shape and its structure. The first two of these are quantified by the flame standoff distance,  $X_f$ , and the flame cone angle,  $\theta_f$  respectively.

In the same chapter, the existing theories explaining LSB operation were outlined. These theories were developed based on observations of the LSB flame and flow field from experiments conducted at atmospheric pressure, using low velocity, non-preheated reactants. To recapitulate one of the objective of this thesis, our goal is to reexamine the validity of these theories at conditions closer to the ones at which gas turbines may be expected to operate.

Finally, Chapter 2 examined key parameters that affect each of the flame characteristics, using the case of varying the reference velocity as an example. The flame location and shape were controlled by factors affecting the axial velocity profile and the turbulent flame speed. A Borghi diagram based on turbulence and laminar flame properties was introduced to designate the regime of premixed turbulent combustion that best describes the flame structure.

The following sections examine the results of experimental investigation of the

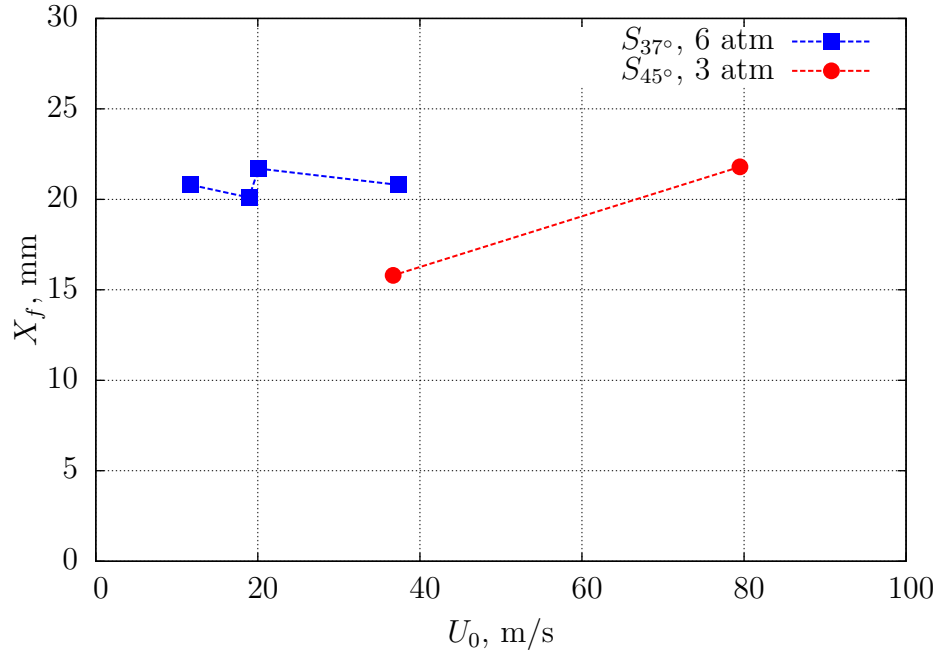
Table 5.1: *The following table presents the cases at which the LSB configurations were tested to study the effects of reference velocity. Chemiluminescence experiments were conducted on Configuration A, while CH PLIF experiments were conducted on Configuration B.*

Experiment	$p$ atm	$T$ K	$\phi$	$U_0$ m/s
Chemiluminescence				
	6.04	525	$0.57 \pm 0.02$	37.3
	6.03	534	$0.55 \pm 0.07$	20.1
	6.19	524	$0.55 \pm 0.07$	18.9
	6.19	493	$0.51 \pm 0.16$	11.7
	3.01	485	$0.57 \pm 0.04$	36.7
	3.02	523	$0.57 \pm 0.02$	79.5
CH PLIF				
	1.0	315	0.90	21
	1.0	443	0.90	40

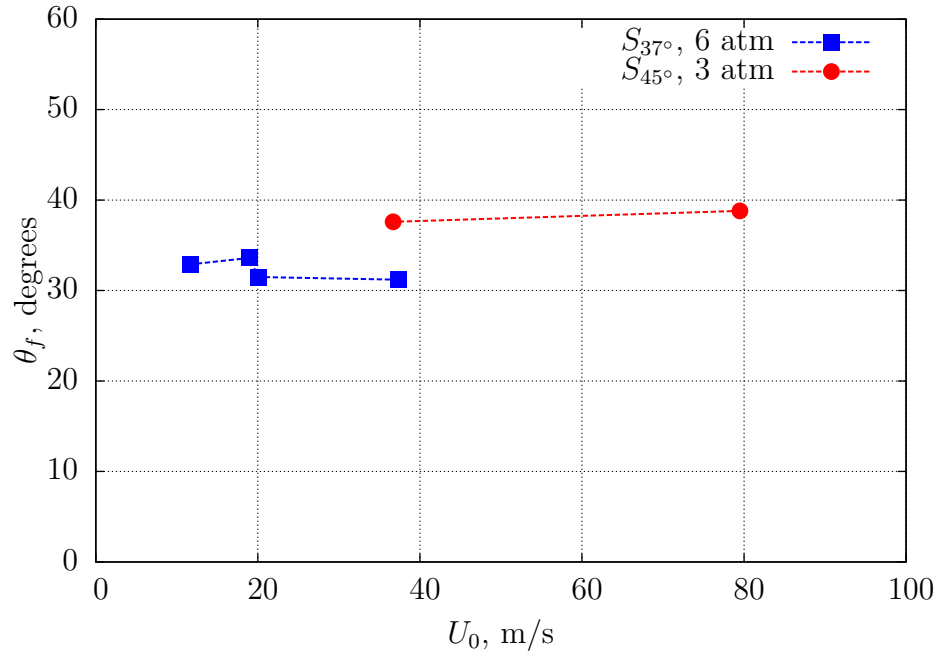
flame characteristics conducted at high preheat and high pressure conditions.

## 5.1 Effect of Reference Velocity

Section 2.1.4.1 explored how changing the reference velocity is not expected to affect the flame location or the flame shape as the balance between the local reactant velocity and the turbulent flame speed remains unaffected. This was further borne out by Equation 2.4 which outlines a simple model for the turbulent flame speed as a linear function of  $u'$  and hence,  $U_0$ . Combined with the self-similar velocity field in the LSB, this predicted that the flame shape and location will be constant over a wide range of operating conditions. Cheng et al.[34] reported no significant deviation from this model over the range of conditions at which they tested the LSB design. It is worth repeating that these experiments were confined to low flow velocities at atmospheric pressure, non-preheated conditions.



(a) Flame standoff distance as a function of the reference velocity



(b) Flame cone angle as a function of the reference velocity

Figure 5.1: The plots above show the effect of changing the reference velocity on the flame location and flame shape. The blue curves are from tests conducted using the  $S_{37^\circ}$  swirler at 6 atm, while the red curves are from tests using the  $S_{45^\circ}$  swirler at 3 atm.

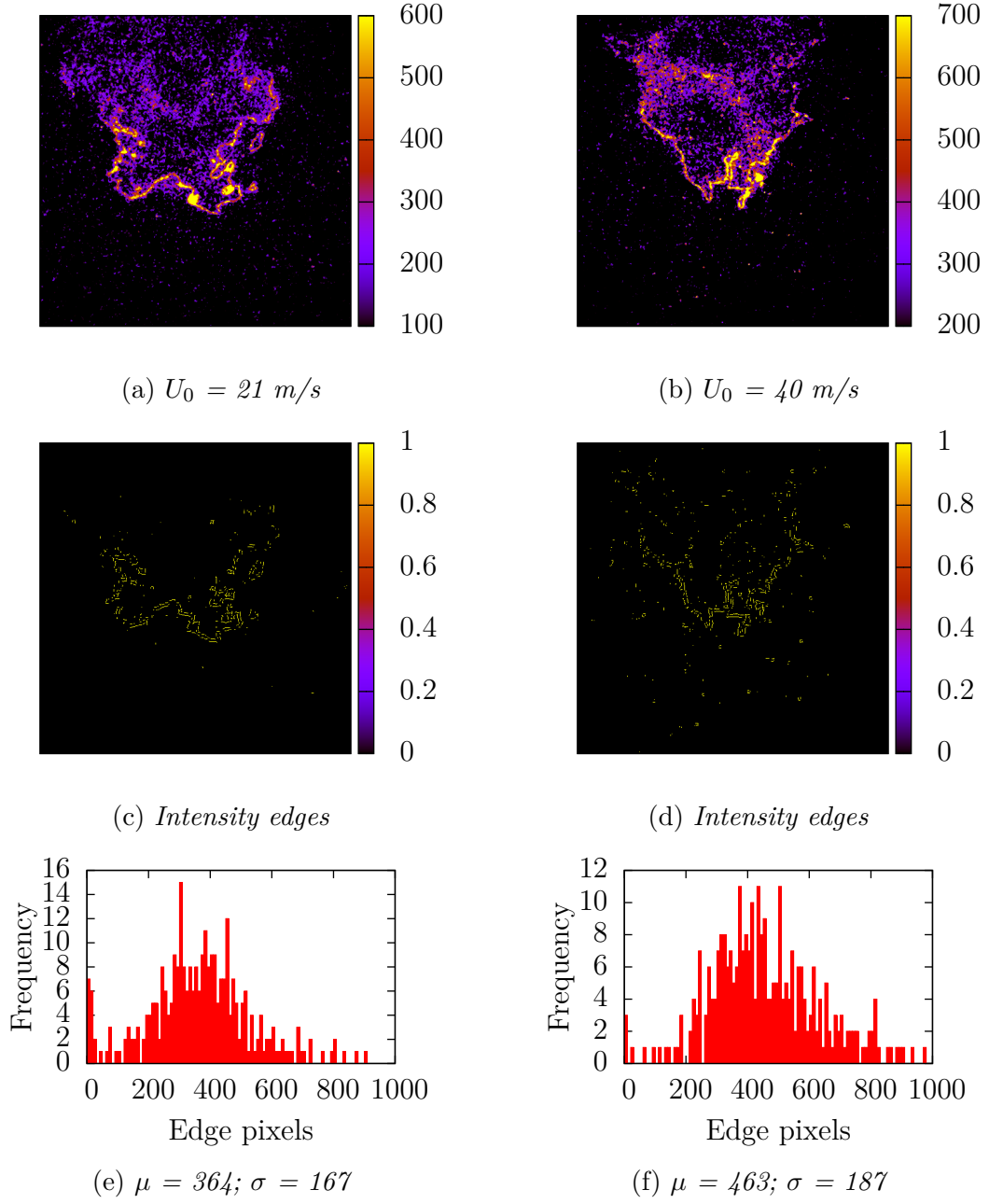


Figure 5.2: The sequence of images on the left and the right pertain to the low and high velocity cases respectively. Each instantaneous frame of PLIF data is processed to detect edges and the statistics of the edge pixels from 300 such frames in the central quarter of the image are plotted as a histogram.

In typical gas turbine applications, the reference velocity is not generally variable with engine loading. Hence, the motivation for studying its effect on the flame characteristics arises from the fact that the reference velocity is a design parameter and its effect on the flame has implications for the design of future LSB-based gas turbine engines. If the atmospheric pressure model holds at high pressure conditions and the reference velocity has no discernible effect on the flame shape and location, such behavior is desirable from the point of view of a gas turbine designer as it would simplify models for heat transfer and combustor length.

In order to verify the validity of this model at high pressure conditions in the presence of substantial preheat, the LSB was operated at a pressure of 6 atm and the reference velocity was varied from 10 m/s to 40 m/s. For these tests, the  $S_{37^\circ}$  swirler was used. In a parallel series of tests, the  $S_{45^\circ}$  swirler was tested at a pressure of 3 atm at reference velocities of 40 m/s and 80 m/s. The preheat temperature for these tests was about 500 K. The measured and calculated flow parameters for these conditions are presented in Table 5.1. The location of the flame was measured from CH\* chemiluminescence images and the results are presented in Figure 5.1.

There is essentially no systematic variation in the flame standoff distance or the flame angle for the low velocity,  $S_{37^\circ}$  tests. This is in line with Equation 2.5's prediction and confirms its applicability even at elevated pressure and preheat conditions.

When the  $S_{45^\circ}$  swirler was tested at higher reference velocities, however, the flame location shifted downstream sharply. This indicates potential limitations to the simple flame stabilization model that may not predict the behavior of the LSB flame at elevated pressures and temperatures, particularly at high reference velocities.

A possible explanation for this observation could be gleaned from considering the effect that increasing the reference velocity has on the turbulent combustion regime in which the LSB combustor operates. Previous studies have operated the LSB in regimes where Equation 2.4 predicts the variation of the turbulent flame

speed with  $u'$  with reasonably fidelity. The arguments behind the formulation of Equation 2.4 assume that a turbulent flame can be treated as a distorted/wrinkled laminar flame in the presence of large scale, low intensity turbulence. This assumption is largely true in the wrinkled flame regime and may even be extended apply to a mildly corrugated flame. However, as we approach large  $\frac{u'}{S_L}$  values and operate in the thin reaction zone—where most gas turbine combustors operate—the flame bears little resemblance to a wrinkled laminar sheet. Since increasing the reference velocity traverses the operating point along the vertical axis of the Borghi diagram, it can cause the turbulent combustion regime to change at high values of  $\frac{u'}{S_L}$ , resulting in the “bending effect” in the  $\frac{S_T}{S_L}$  vs  $\frac{u'}{S_L}$  diagram.

One way to ascertain the regimes in which the LSB is operated is to image the flame sheet and observe the flame structure. To that end, the LSB (Configuration B) was tested at atmospheric pressure with preheat temperatures ranging from 300 K to 440 K. Two of these conditions are relevant to this discussion and their operating parameters are presented in Table 5.1. In order to prevent flame blow-off, the equivalence ratio had to be increased to 0.9. The resulting flame illuminated by an 80 mm tall, 250  $\mu\text{m}$  thick laser sheet from the alexandrite laser and imaged using the PI-MAX 512 $\times$ 512 intensified camera equipped with a 50 mm, f/1.4 lens. The camera was gated to 300 ns centered on the 70 ns laser pulse. The laser was operated at 10 Hz and the pulse energy was measured to be about 14 mJ for the low velocity case and about 17 mJ for the high velocity case. A sample frame from each dataset is shown in Figure 5.2.

Both the low and high velocity cases show an essentially unbroken flame sheet that is characterized by wrinkles. This is consistent with the operating regime being in the wrinkled laminar flame region of the Borghi diagram. The level of wrinkling in these images can be estimated by gathering statistics on the number of pixels that are found on edges of intensity gradients. In order for the statistics to be affected only by the

Table 5.2: *The following table lists the conditions at which the LSB flow field was mapped using LDV. These experiments were performed on Configuration A.*

Case	$T$ K	$\phi$ m/s	$U_0$	$Re$
Cold, Non-reacting (CN)	300	-	30	72700
Hot, Non-reacting (HN)	500	-	75	75200
Hot, Reacting (HR)	465	0.55	30	39500

level of wrinkling and not by the movement of the flame, the statistics are gathered  
only from the middle quarter of the flame where the flame sheet is nearly planar.  
The edges and corresponding histograms from this investigation are also presented in  
Figure 5.2.

The level of wrinkling is predictably higher for the high velocity, high preheat case.  
The instances of disjoint packets of flame are also higher for this case. This indicates  
that the high velocity, high preheat case is approaching the boundary between the  
laminar wrinkled flame regime and the corrugated flame regime. Even accounting for  
the effects of operating this flame at a leaner equivalence ratio, at elevated pressures,  
both the laminar flame speed,  $S_L$ , and the flame thickness,  $\delta_f$ , are diminished. This  
places the operating regime higher (and more to the right) on the Borghi diagram  
where a large enough reference velocity can push the operating point from the region  
of corrugated flames into the broken flamelets regime. This would have not been  
possible for similar increases in reference velocity at atmospheric pressure conditions  
where the corresponding  $\frac{u'}{S_L}$  values would be too low. Such a transition would cause  
 $S_T$  to increase at a reduced rate with  $u'$  and  $U_0$ , resulting in the observed downstream  
shift of the high pressure LSB flame at high reference velocities.



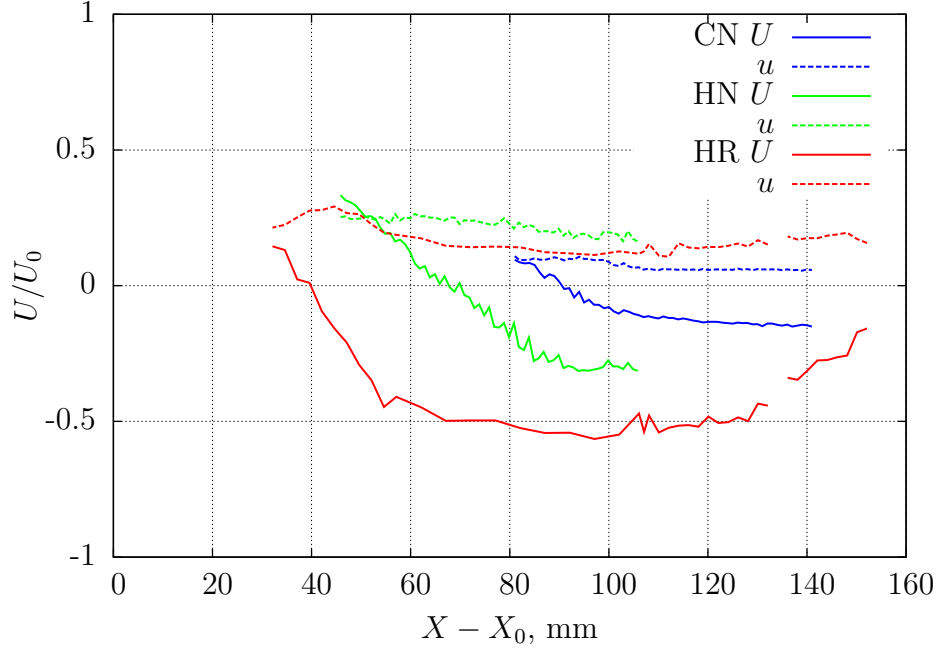


Figure 5.3: The plots above show results from LDV mapping of the flow field in the LSB. Mean and rms axial velocity profiles are shown for cold, hot, and reacting flow fields. The velocities are normalized by the reference velocity, while the abscissa is shifted to align the virtual origins of the profiles.

## 5.2 Effect of Preheat Temperature

1645

Next, we consider the effect of increasing the preheat temperature on the flame loca- 1646  
tion, shape and structure. The preheat temperature of the reactants is an important 1647  
flow parameter for gas turbine applications and impacts the reacting flow field in the 1648  
LSB in two ways. First, a higher preheat temperature increases the kinematic vis- 1649  
cosity of the flow. The mechanism that transports the axial momentum in the radial 1650  
direction and causes the flow to diverge is driven by viscous effects. Enhanced vis- 1651  
cous effects will result in a steeper decrease in the axial velocity. Simultaneously, this 1652  
causes an increased production of turbulent kinetic energy. Second, global reaction 1653  
rates increase with temperature, causing the laminar flame speed to increase. The 1654  
net result of the increased turbulence and laminar flame speed is that the turbulent 1655  
flame propagates faster. As a result of the steeper velocity decay and the increased 1656

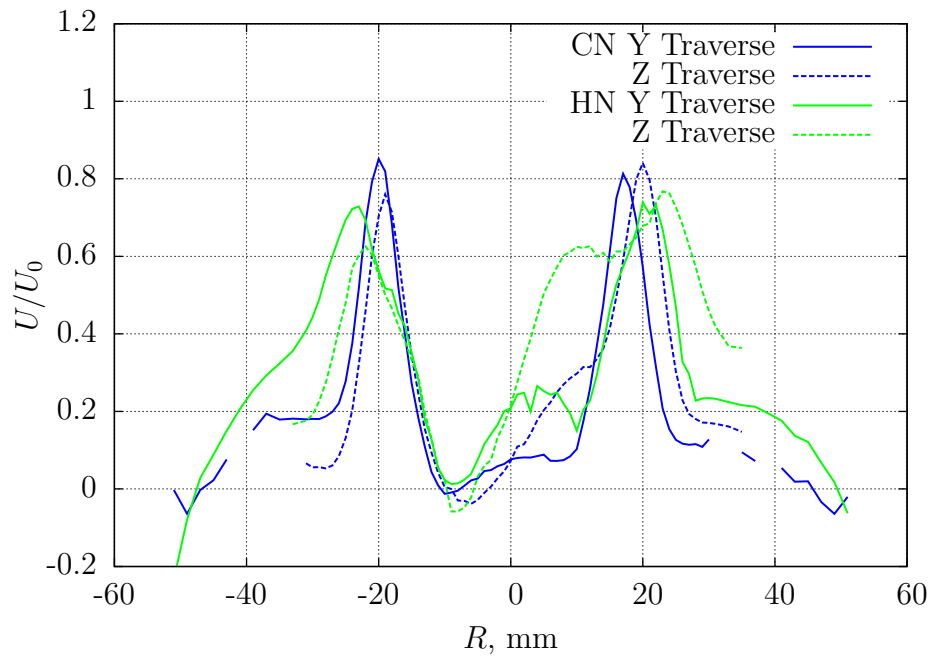


Figure 5.4: The plot above shows LDV data from two orthogonal traverses (along  $Y$  and  $Z$  axes) performed across the LSB combustor. The data is presented for cold and hot cases (both non-reacting) to highlight the effect of preheat on the mean axial velocity profile through the shear layer. The traverses are performed 15 mm downstream of the inlet and use the  $S_{45^\circ}$  swirler in Configuration A.

turbulent flame speed, the flame will be expected to stabilize closer to the inlet of the LSB.

In order to explore this in greater detail, the velocity field of the combustor was mapped using Laser Doppler Velocimetry (LDV). The conditions were chosen to study the effect of increasing the preheat temperature on both reacting and non-reacting LSB flow fields. Further, the study includes both low and high reference velocity cases. The relevant flow parameters relating to these tests are presented in Table 5.2. The test cases are named CN (Cold, Non-reacting), HN (Hot, Non-reacting) and HR (Hot, Reacting) based on their preheat and presence of a flame. All LDV tests were limited to atmospheric pressure conditions. Implementing the LDV technique at elevated pressures proved difficult due to beam steering issues, coupled with impractical turnaround times between the successive runs that would be required to obtain sufficient LDV data points for analysis.

The normalized centerline mean and rms axial velocity profiles for the three cases are presented in Figure 5.3. The abscissa represents the distance from the virtual origin as defined in Section 2.1.2.

The results show that increasing the preheat temperature causes the normalized velocity slope to increase. As noted in Chapter 2, Cheng et al.[34] reported that this slope is unaffected by the Reynolds number,  $Re$ , of the operating condition. The results in Figure 5.3 however, show that even though the cases CN and HN have similar  $Re$ , their mean velocity profiles have very different slopes. This indicates that the mean axial stretch in the near field of the LSB flow field is a stronger function of the preheat temperature than  $Re$ .

Even assuming that  $S_T$  is constant, these results suggest that at higher preheat temperatures, the flame would stabilize closer to the dump plane because of the faster reactant velocity decay. In fact, the faster velocity decay produces a higher  $u'$  and would increase  $S_T$ , further causing the flame standoff location to shift upstream.

This affects the stability of the flame in two ways. First, the flame is closer to the inlet, resulting in more effective heat transfer from the flame zone into the reactants. Second, the steeper profiles of  $U$  and  $S_T$  limit any movement of the flame in response to perturbations in the local flow field. These two characteristics of the preheated flame lead to an intuitive result—the LSB flame behaves more stably at high preheat conditions.

The effect of increasing the preheat temperature on the flame cone angle is harder to predict. The increased divergence drives more axial momentum into the shear layer, increasing the local velocity of the reactants. At the same time, the increased  $u'$  and  $S_L$  drive up the turbulent flame speed. The competing effects of the two parameters on the flame angle can be explored by propagating a change in the parameters as follows.

$$\begin{aligned} U \sin \theta_f &= S_T \\ \therefore \frac{\delta \sin \theta_f}{\sin \theta_f} &= \frac{\delta S_T}{S_T} - \frac{\delta U}{U} \end{aligned} \quad (5.1)$$

Figure 5.4 shows LDV results for the axial velocity measured 15 mm downstream of the inlet. These measurements are taken from two orthogonal traverses across the flow field and show the profiles for the CN and HN cases. While the increased momentum transport has certainly thickened the shear layer, the peak axial velocity remains the same for the two cases. As a result, changes in the turbulent flame speed would be expected to dominate and cause the flame angle to increase.

Finally, we return to the Borghi diagram to consider the effect of a higher preheat temperature on the flame structure. On the Y-axis, the exponential dependence of  $S_L$  on temperature will decrease the ordinate of the operating point, while on the X-axis, a slight decrease in the flame thickness will move the point to the right. The

Table 5.3: *The following table lists the conditions at which CH PLIF images were acquired of a low and high swirl case at atmospheric pressure. These experiments were performed on Configuration B.*

Case	$T$ K	$\phi$ m/s	$U_0$	$S$
Low Swirl	443	0.90	40	0.57
High Swirl	434	0.91	40	0.62

net down-and-right movement of the operating point drives the flame regime away  
from broken flamelets and closer towards wrinkled flames. Since our flame structure  
data was already in the wrinkled flame regime, this change could not be imaged by  
CH PLIF.

### 5.3 Effect of Swirl

As described in Chapter 2, the amount of swirl in the LSB flow field is quantified  
by a swirl number as defined in Equation 2.1. Even though there is no tangential  
momentum in the core of the LSB flow field where the flame is stabilized, the swirl  
still exerts influence on the flame characteristics.

The LSB utilizes swirl to enhance the divergence of the flow near the inlet. Con-  
sequently, an increased swirl number results in a sharper deceleration of the reactants  
and a more upstream stabilization point for the turbulent flame. This is corroborated  
by past research[19,97] which reported shorter, wider (higher flame cone angle) flames  
when the amount of swirl in a combustor was increased.

The results of the present investigation are in agreement with this observation.  
Operated at identical inlet conditions, the  $S_{45^\circ}$  swirler stabilizes a flame closer to the  
inlet and with a larger flame angle compared to the  $S_{37^\circ}$  swirler.

This result highlights an interesting trade-off for the designers of LSB-based gas

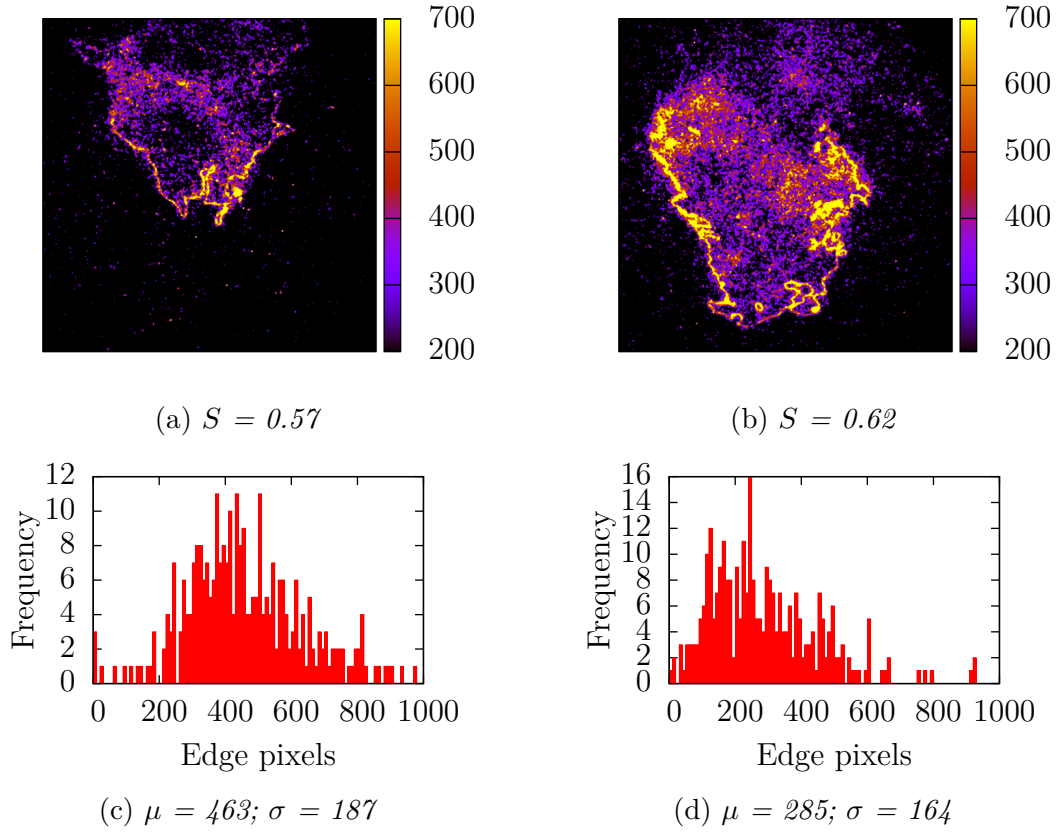


Figure 5.5: The images above show a low and high swirl flame imaged by CH PLIF. These experiments are performed on Configuration B under preheated, atmospheric pressure conditions.

turbine engines. The  $S_{45^\circ}$  flame is located in a sharply decelerating flow field and as we discussed in Section 5.2, this results in a more stable flame resistant to perturbations in the flow field. Simultaneously, the presence of the concentrated heat release near the inlet increases the strength of the toroidal recirculation zone present there. As we shall see in Section 5.4, this recirculation zone can become powerful enough to even cause the flame to attach itself to the lip of the inlet. Such a strong recirculation zone entrains hot products and retains them longer near the zone of heat release. This is a recipe for the production of thermal  $\text{NO}_x$ . While no emission measurements were made as part of this study, it may be reasonably anticipated that the  $\text{NO}_x$  performance of the  $S_{45^\circ}$  swirler will be degraded compared to the  $S_{37^\circ}$  swirler. The trade-off for gas turbine engine designers is thus between flame stability and emissions performance.

In Configuration A, the theoretical swirl number of the flow field is varied by switching out the swirlers. The mass flow split of each swirler is estimated from the blockage of the perforated plates covering the central portion of the swirler. On the other hand, Configuration B not only allows precise knowledge of this mass flow split, but also allows one to vary it in operation. This offers an alternate way to study the effect of swirl by changing the mass flow split. Figure 5.5 shows CH PLIF images of the flame sheet for a low and high swirl case. Also shown are the corresponding histograms measuring the statistics of the edge pixels in the central one-fourth of the flame. The test conditions for these two cases are presented in Table 5.3.

The results of this investigation show that the flame position is strongly affected by changing the swirl number in this manner. The reduced flow of reactants through the central portion, coupled with the enhanced divergence induced by the increased swirl flow causes the flame to shift much further upstream. The reduction in the local reactant velocity also decreases the local turbulence level and accounts for a less convoluted flame sheet.

Table 5.4: *The following table lists the conditions at which the equivalence ratio was varied to study its effects on the flame characteristics. The chemiluminescence experiments were performed on Configuration A, while the CH PLIF experiments were performed on Configuration B.*

Experiment	$p$ atm	$T$ K	$\phi$	$U_0$ m/s
Chemiluminescence				
	12.4	570	$0.53 \pm 0.01$	39.42
	12.6	583	$0.58 \pm 0.01$	39.42
CH PLIF				
	1.0	443	0.90	40
	1.0	438	1.05	40

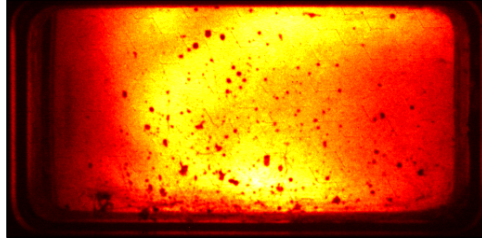
To conclude, changing the amount of swirl in the LSB flow field affects the flame stabilization point and the flame cone angle. This is primarily the effect of swirl changing the divergence of the core flow. In the limit, this behavior causes the LSB to behave like a conventional swirl-stabilized combustor.

## 5.4 Effect of Equivalence Ratio

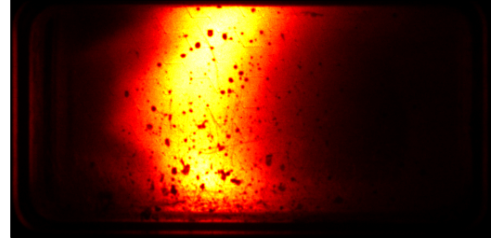
The LSB is primarily intended for fuel-lean operation in order to utilize its low  $\text{NO}_x$  emission performance. As a result, most of the high pressure testing was done as close as possible to a target  $\phi$  of 0.56. Limited testing was carried out at 12 atm for two off-target conditions: a slightly richer ( $\phi \approx 0.58$ ) and a slightly leaner ( $\phi \approx 0.53$ ) mixture, in order to explore the sensitivity of the LSB flame to limited changes in equivalence ratio. The  $S_{45^\circ}$  swirler was used for these tests. The conditions are presented in Table 5.4, while the corresponding averaged and Abel-deconvoluted flame images are presented in Figure 5.6.

Two characteristics of the flame are immediately obvious from these images. First, the zone of heat release, marked by the region from which  $\text{CH}^*$  chemiluminescence is

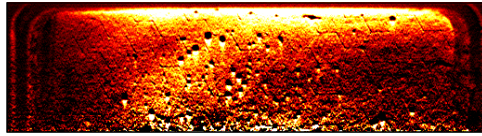




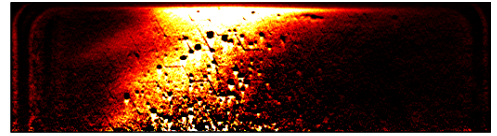
(a)  $\phi = 0.53$



(b)  $\phi = 0.58$

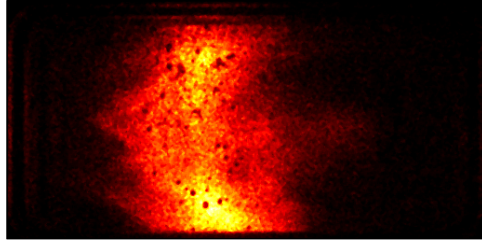


(c) *Abel-deconvoluted image*

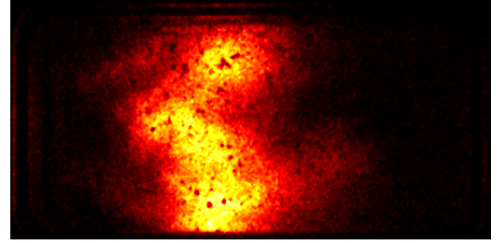


(d) *Abel-deconvoluted image*

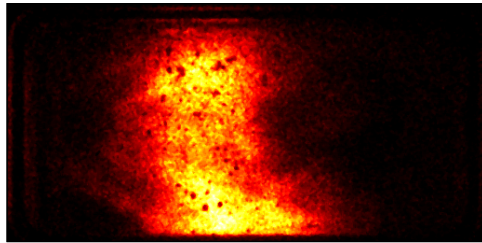
Figure 5.6: Figures 5.6a–5.6b show mean  $CH^*$  chemiluminescence images of the LSB flame taken at high pressure for two equivalence ratios. Figures 5.6c–5.6d show the Abel-deconvolution of the average image highlighting the flame brush. The centerline of the combustor is along the lower edge of the Abel half-images.



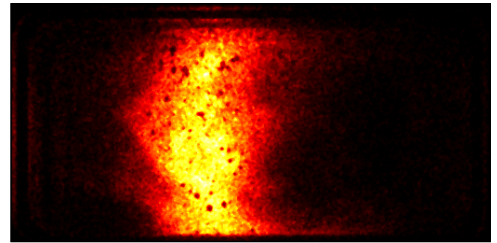
(a) *Frame #90*



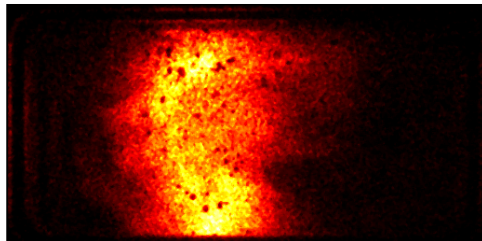
(b) *Frame #91*



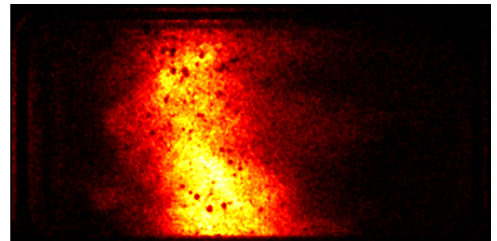
(c) *Frame #92*



(d) *Frame #93*



(e) *Frame #94*



(f) *Frame #95*

Figure 5.7: The sequence of frames above is taken from the high equivalence ratio data set and shows the flame intermittently attaching to the lip of the inlet.

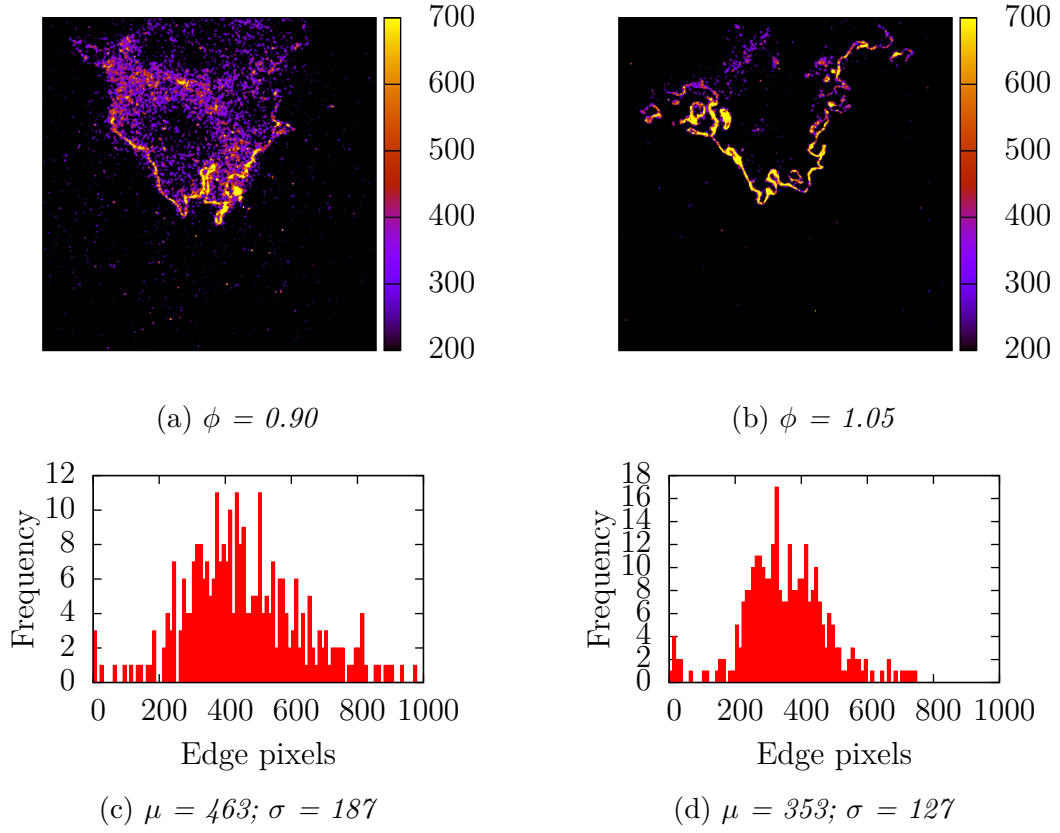


Figure 5.8: *The images above are instantaneous CH PLIF images of a relatively lean and rich flame at preheated, atmospheric pressure conditions. The histograms show the statistics of the number of detected intensity edges over 300 such frames. These experiments are conducted on Configuration B.*

observed, is increasingly compact at fuel-rich conditions. Virtually all other flame images acquired at leaner conditions show a long flame, with the heat release distributed over the entire visible area of the combustor. As discussed in the previous section, a compact heat release zone near the inlet results in strong recirculation features and potentially poor  $\text{NO}_x$  performance, even accounting for the higher equivalence ratio.

Second, the fuel-rich flame brush can be observed to wrap around and anchor itself on the dump plane. This is particularly observable in the Abel-deconvoluted image. The attached region is not as bright as the rest of the flame brush, indicating that the flame may be attaching itself intermittently. This intermittent behavior can be confirmed from the instantaneous images where it is visible on some of the acquired images, but not others. A sequence of such images are shown in Figure 5.7. This behavior was alluded to in Section 5.3 as being the result of the enhanced toroidal recirculation zone produced by this swirler. Thus, the intermittent attachment of the flame to the inlet indicates the increased importance of the toroidal recirculation zone in stabilizing the flame.

It should be noted that the reliance on a toroidal recirculation zone to anchor the flame to the inlet is one of the primary flame stabilization mechanisms used by traditional swirl combustors. Thus, LSB swirlers with high vane angles tend to behave like traditional swirl combustors at fuel-rich conditions.

In order to explore the flame structure of a richer flame, LSB Configuration B was operated at  $\phi$  values of 0.90 and 1.05 and imaged using CH PLIF. The conditions are listed in Table 5.4 and the images are presented in Figure 5.8. On the Borghi diagram, increasing  $\phi$  causes a higher  $S_L$  and reduces  $\delta_f$ . This moves the operating point down and to the right, taking it closer to a wrinkled flame regime. This is reflected in the histogram where the richer flame is seen to be less wrinkled.

Table 5.5: *The following are the test conditions at which pressure sweeps were performed to study its effects on the flame characteristics. The experiments were conducted on Configuration A and the swirler used for the pressure sweeps is noted.*

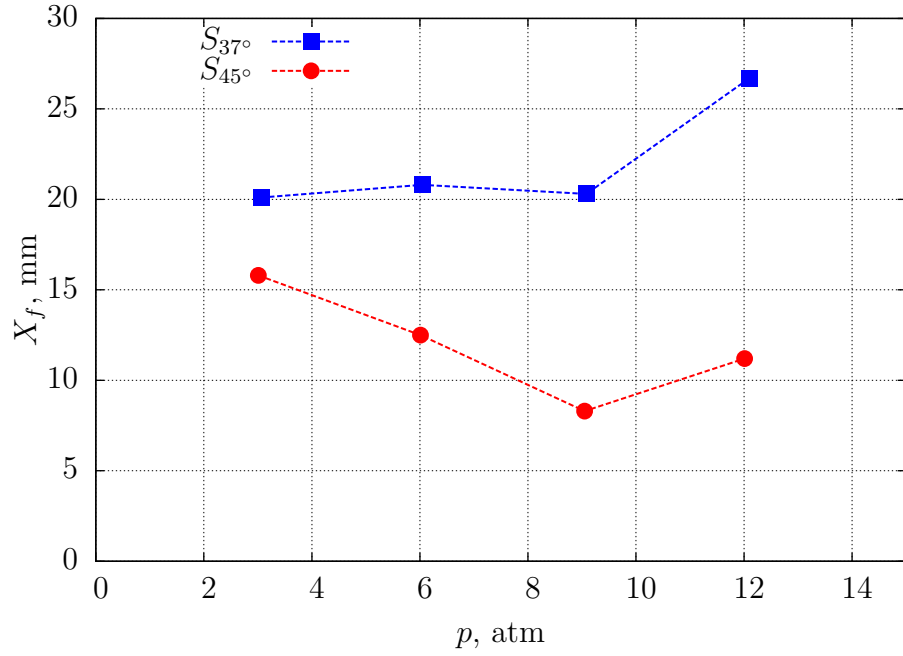
Experiment	$p$ atm	$T$ K	$\phi$	$U_0$ m/s
<hr/>				
$S_{37^\circ}$				
	3.06	506	$0.57 \pm 0.04$	37.8
	6.04	525	$0.57 \pm 0.02$	37.3
	9.08	544	$0.56 \pm 0.02$	37.2
	12.1	559	$0.56 \pm 0.01$	37.4
<hr/>				
$S_{45^\circ}$				
	3.01	485	$0.57 \pm 0.04$	36.7
	6.01	516	$0.58 \pm 0.02$	38.2
	9.05	553	$0.58 \pm 0.01$	39.2
	12.0	582	$0.56 \pm 0.01$	40.9

## 5.5 Effect of Combustor Pressure

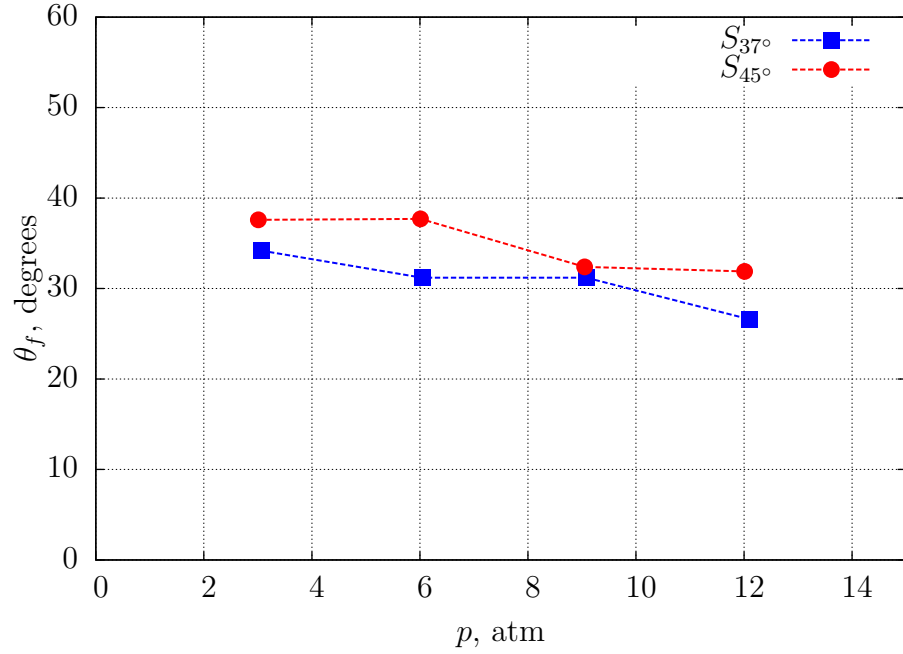
1791

In many gas turbine engines, the combustor pressure varies directly with the loading 1792  
of the engine. Like the preheat temperature, the combustor pressure affects the 1793  
LSB flame both through the fluid mechanics of the flow (by decreasing the kinematic 1794  
viscosity) and the kinetics of the chemical reactions (affecting the laminar flame speed) 1795  
in the flame. 1796

There is some confusion over how to study this effect and what to attribute it to. 1797  
Pressure effects are often tracked using the Reynolds number. However, as noted in 1798  
Section 5.2, it might not be the right parameter to use in the near field of the inlet. 1799  
According to the turbulent flame speed model from Equation 2.4, at high pressures, 1800  
the  $S_L$  term is insignificant compared to  $u'$  and thus, the turbulent flame speed should 1801  
see minimal pressure effects. Indeed, Kobayashi et al.[98,99] have observed precisely 1802  
this—the turbulent flame speed appears to be independent of the combustor pressure 1803  
in their Bunsen burner setup. While Cheng et al. highlight the diminishing role of 1804



(a) Flame standoff distance as a function of the combustor pressure



(b) Flame cone angle as a function of the combustor pressure

Figure 5.9: The plots above show the effect of varying the combustor pressure on the flame location and flame cone angle. The blue curves represent data points from the  $S_{37^\circ}$  swirler tests, while the red curves represent data from the  $S_{45^\circ}$  swirler tests.

$S_L$ , Griebel et al.[100] attribute this behavior to the fact that the decrease in laminar flame speed at high pressure is compensated for by the broadening of the turbulence spectrum. This results in finer turbulent structures in the flow as pressure increases—an observation also made by Kobayashi[101]—that cause a higher turbulent flame surface area and keep the turbulent flame speed nearly constant. Griebel et al. further note that theoretically, a slight drop in the turbulent flame speed with pressure may be expected.

In order to resolve the uncertainties regarding how the LSB flame responds to combustor pressure, the flame was imaged over a range of operating conditions from 3 to 12 atm. For these tests, the reference velocity and the equivalence ratio were held constant. However, the temperature of the reactants continues to increase with pressure. The reason for this was discussed in Chapter 3 and is because of the reduced heat losses in the connecting pipes at the high flow rates required to pressurize the LSB. The experimental conditions are presented in Table 5.5 The flame location and shape inferred from the flame images are presented in Figure 5.9.

At low to moderate pressures, the flame location is nearly invariant for  $S_{37^\circ}$ , but moves upstream for the  $S_{45^\circ}$  cases. This behavior can be explained as follows. The flame stabilization location for the  $S_{45^\circ}$  swirler is closer to the dump plane compared to the  $S_{37^\circ}$  swirler. Since the heat transfer back to the reactants is more efficient, the increasing reactant temperature through our test cases dominate pressure effects and moves the  $S_{45^\circ}$  flame upstream. The  $S_{37^\circ}$  flame is less affected by these processes.

At high pressures, however, both flames are observed to move downstream, despite the increasing preheat temperatures. The apparent decrease in the turbulent flame speed at these conditions is an unexpected result, and Equation 2.4 is insufficient in accounting for this observation. Figure 5.9 also shows that the flame angle for both cases decreases slightly with pressure. This suggests that the turbulent flame speed was consistently and slowly decreasing with pressure as expected by Griebel et al. In

light of this, the nearly constant location of the  $S_{37^\circ}$  flame could be attributed to the effects of increasing combustor pressure and preheat temperature nearly canceling each other out at the lower pressures.

This has repercussions for the gas turbine designers as a flame stabilized further away from the inlet is likelier to be blown off due to perturbations. Increasing the preheat of the reactants could offset this behavior, as can increasing the swirl in the flow field. In practice, these may be non-trivial to implement in a gas turbine engine. Adding hydrogen to the reactants may be a simpler way to stabilize the high pressure flames.

Finally, it is interesting to examine this on a Borghi diagram to deduce any changes in the flame structure that might result. Kobayashi et al.[101] report that the increasing pressure causes a weak drop in  $u'$ , reaching a minimum around 10 atm. However, the  $\frac{u'}{S_L}$  factor would be dominated by the precipitous fall in the laminar flame speed, causing it to in fact increase with pressure. On the X-axis, the integral length scale is very nearly unaffected by the pressure change, but the flame thickness decreases rapidly. Thus, pressure causes the operating point to move up and to the right on the diagram. This motion is unlikely to cause the turbulent combustion regime to change. In the absence of a drastic change in the turbulent combustion characteristics, the only observable effect is likely to be an increase in the fine structure of the wrinkles in the flame due to the broadened turbulence spectrum.

## 5.6 Summary of Results

The effect of various flow parameters on the LSB flame characteristics have been examined using both CH\* chemiluminescence imaging and CH PLIF. The key results from this investigation are as follows:

1. Low to moderate reference velocities do not affect the flame at high pressure.



- High reference velocities cause the flame to shift downstream. The flame be- 1857  
comes more wrinkled due to increased turbulence. 1858
2. Preheating the reactants causes the flame to move upstream, but may also 1859  
strengthen recirculation zones in the combustor. The flame structure is expected 1860  
to become more wrinkled. 1861
  3. Swirl—controlled either through the vane angle or through the mass flow split— 1862  
causes the flame to anchor closer to the inlet and have a larger cone angle. The 1863  
decreased flow rate through the core reduces wrinkling in the flame structure. 1864
  4. Richer flames at high pressure and high swirl can change flame shape and behave 1865  
like attached flames. Equivalence ratio also results in strong combustion and a 1866  
less wrinkled flame. 1867
  5. At high pressures, the LSB flame moves downstream. In order to preserve 1868  
flame stability, this should be countered by increasing the preheat or changing 1869  
the swirl number, if possible. 1870

**CHAPTER 6**  
**CONCLUSIONS**

1871

1872

## APPENDIX A

1873

### SEEDER DESIGN

1874

A new seeder was designed for use in high pressure implementations of diagnostic techniques like Laser Doppler Velocimetry (LDV), Particle Image Velocimetry (PIV), etc.

1875  
1876  
1877

The previous design, as shown in Figure A.1, was a fluidized bed seeding generator. Seeding particles in a cylindrical vessel are fluidized by an air-turbine vibrator. Air is introduced into the vessel in the form of two opposing jets directed tangentially to produce a small amount of swirl in the flow field. Particles are picked up by the air flow and the swirl aids in separating the heavy/coagulated clumps of seeding particles by centrifugal acceleration.

1878

1879

1880

1881

1882

1883

This design had several shortcomings. First, it is observed that the seeding density of the seeded flow generally decreases over time, even if the seeding particles have not been depleted. The seeding particles tend to coagulate over time, due to the buildup of moisture, static charge, etc. In such cases, the vibrator can no longer effectively fluidize the particles. Further, the tangential introduction of the air flow preferentially depletes particles near the walls of the container, leaving the center relatively undisturbed. The cumulative effect of these phenomena diminishes the effectiveness of the seeder.

1884

1885

1886

1887

1888

1889

1890

1891

Second, the fluidized bed requires a minimum amount of seeding particles to function effectively. This requires the seeder to be refilled even before all the seeding particles are consumed.

1892

1893

1894

Third, when designed for high pressure applications, the seeder will become quite heavy due to flanges and other fittings. Such a setup cannot be easily fluidized using a reasonable-sized air-turbine vibrator.

1895

1896

1897

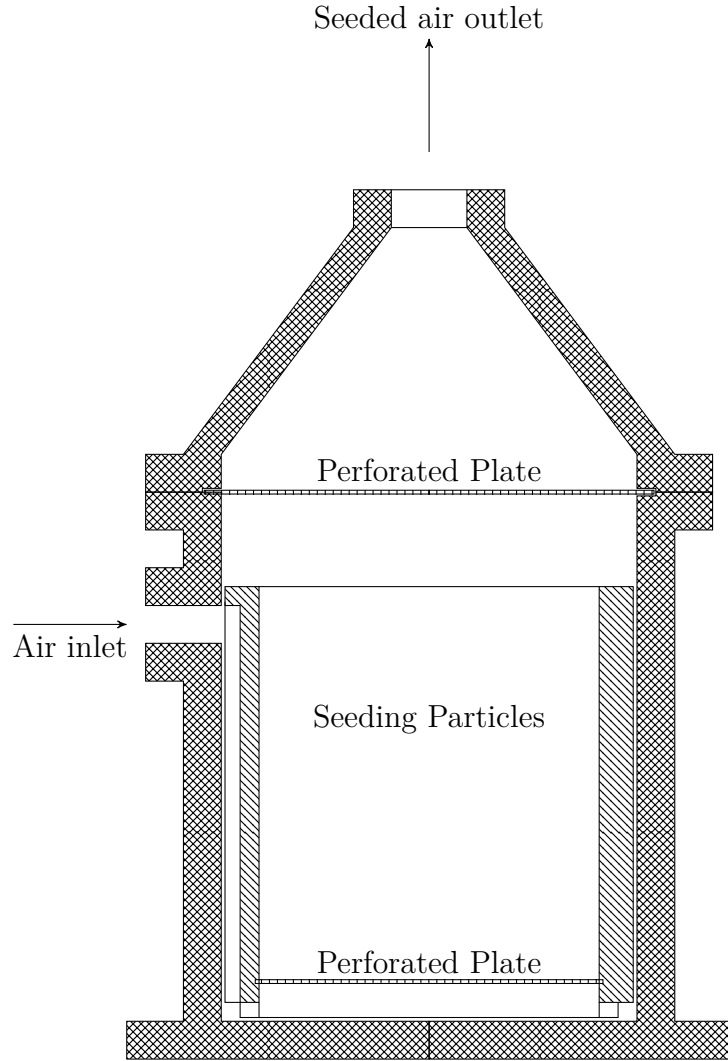


Figure A.1: A schematic of the old fluidized bed seeder is presented. The air enters the seeder through a groove along the inner vessel and is injected with a tangential velocity at the base of the seeder. The whole assembly is vibrated (vibrator not shown) to keep the particle bed fluidized. The seeded air flow exits through the outlet on the top.

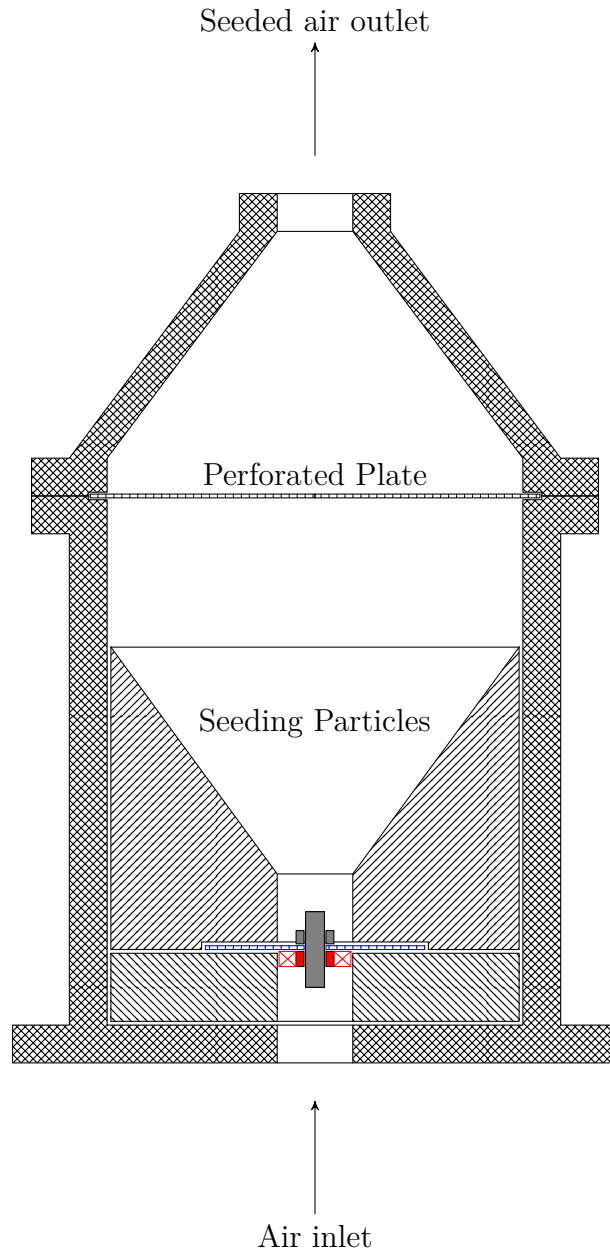


Figure A.2: *The improved design of the seeder is shown here in schematic form. The air enters the assembly from the inlet at the bottom, passes through the swirler (shown in red) and enters the seeder. The perforated plate at the bottom (shown in blue) keeps the seeding particles within the seeder. The swirler hub is threaded, allowing it to be secured to the perforated plate by a short steel bolt (shown in gray). After picking up the particles, a second perforated plate prevents large clumped seeding particles from passing through. The seeded air flow exits through the outlet at the top.*

The new seeder design is shown in Figure A.2, and resembles a funnel with a 1898  
swirler located halfway up the stem. A perforated base plate holds the swirler and 1899  
the seeding particles in the conical section of the swirler. Due to the steep angle of the 1900  
sides of the conical section, the seeding particles continuously collapse into the central 1901  
section. This negates any need for vibrating the system. Air is introduced from the 1902  
bottom of the seeder and enters the vessel by passing through the swirler. Since all 1903  
the air enters this way, there is a considerable amount of swirl in the resulting flow 1904  
field, Heavy/coagulated seeding particles are flung outward, while lighter particles are 1905  
carried with the air. After a sufficient distance to allow for the cyclonic separation 1906  
to be effective, the seeded air passes through another perforated plate which further 1907  
limits the presence of large clumps of particles. The exiting air is now spatially and 1908  
temporally uniformly seeded. 1909

# REFERENCES

1910

- [1] I. Glassman, *Combustion*. Academic Press, 1996. 1911
- [2] N. Syred and J. M. Beér, “Combustion in Swirling Flows: A Review,” *Combustion and Flame*, vol. 23, no. 2, pp. 143–201, 1974. 1912  
1913
- [3] D. G. Lilley, “Swirl Flows in Combustion: A Review,” *AIAA Journal*, vol. 15, 1914  
no. 8, pp. 1063–1078, 1977. 1915
- [4] B. Bédat and R. K. Cheng, “Experimental Study of Premixed Flames in Intense 1916  
Isotropic Turbulence,” *Combustion and Flame*, vol. 100, no. 3, pp. 485–494, 1917  
1995. 1918
- [5] R. S. Barlow, R. W. Dibble, J. Y. Chen, and R. P. Lucht, “Effect of Damköhler 1919  
Number on Superequilibrium OH Concentration in Turbulent Nonpremixed Jet 1920  
Flames,” *Combustion and Flame*, vol. 82, no. 3-4, pp. 235–251, 1990. 1921
- [6] C. F. Kaminski, J. Hult, and M. Aldén, “High repetition rate planar laser 1922  
induced fluorescence of OH in a turbulent non-premixed flame,” *Applied Physics 1923  
B: Lasers and Optics*, vol. 68, no. 4, pp. 757–760, 1999. 1924
- [7] J. Hult, U. Meier, W. Meier, A. Harvey, and C. F. Kaminski, “Experimental 1925  
analysis of local flame extinction in a turbulent jet diffusion flame by high 1926  
repetition 2-D laser techniques and multi-scalar measurements,” in *Proceedings 1927  
of the Combustion Institute*, vol. 30, pp. 701–709, 2005. 1928
- [8] H. Malm, G. Sparr, J. Hult, and C. F. Kaminski, “Nonlinear diffusion filtering 1929  
of images obtained by planar laser-induced fluorescence spectroscopy,” *Journal 1930  
of The Optical Society of America A: Optics, image science, and vision*, vol. 17, 1931  
no. 12, pp. 2148–2156, 2000. 1932

- [9] R. Abu-Gharbieh, G. Hamarneh, T. Gustavsson, and C. F. Kaminski, “Flame front tracking by laser induced fluorescence spectroscopy and advanced image analysis,” *Optics Express*, vol. 8, no. 5, pp. 278–287, 2001.
- [10] C. M. Vagelopoulos and J. H. Frank, “An experimental and numerical study on the adequacy of CH as a flame marker in premixed methane flames,” in *Proceedings of the Combustion Institute*, vol. 30, pp. 241–249, 2005.
- [11] M. Köhler, A. Brockhinke, M. Braun-Unkhoff, and K. Kohse-Höinghaus, “Quantitative Laser Diagnostic and Modeling Study of C<sub>2</sub> and CH Chemistry in Combustion,” *The Journal of Physical Chemistry A*, vol. 114, no. 14, pp. 4719–4734, 2010.
- [12] C. P. Fenimore, “Formation of nitric oxide in premixed hydrocarbon flames,” in *Symposium (International) on Combustion*, vol. 13, pp. 373–380, 1971.
- [13] Z. S. Li, J. Kiefer, J. Zetterberg, M. Linvin, A. Leipertz, X. S. Bai, and M. Aldén, “Development of improved PLIF CH detection using an Alexandrite laser for single-shot investigation of turbulent and lean flames,” in *Proceedings of the Combustion Institute*, vol. 31, pp. 727–735, 2007.
- [14] H. N. Najm, P. H. Paul, C. J. Mueller, and P. S. Wyckoff, “On the Adequacy of Certain Experimental Observables as Measurements of Flame Burning Rate,” *Combustion and Flame*, vol. 113, no. 3, pp. 312–332, 1998.
- [15] J. Kiefer, Z. S. Li, J. Zetterberg, X. S. Bai, and M. Aldén, “Investigation of local flame structures and statistics in partially premixed turbulent jet flames using simultaneous single-shot CH and OH planar laser-induced fluorescence imaging,” *Combustion and Flame*, vol. 154, no. 4, pp. 802–818, 2008.



- [16] P. H. Paul and H. N. Najm, “Planar laser-induced fluorescence imaging of flame heat release rate,” in *Symposium (International) on Combustion*, vol. 27, pp. 43–50, 1998.
- [17] B. O. Ayoola, R. Balachandran, J. H. Frank, E. Mastorakos, and C. F. Kaminiski, “Spatially resolved heat release rate measurements in turbulent premixed flames,” *Combustion and Flame*, vol. 144, no. 1, pp. 1–16, 2006.
- [18] J. Kiefer, Z. S. Li, T. Seeger, A. Leipertz, and M. Aldén, “Planar laser-induced fluorescence of HCO for instantaneous flame front imaging in hydrocarbon flames,” in *Proceedings of the Combustion Institute*, vol. 32, pp. 921–928, 2009.
- [19] C. K. Chan, K. S. Lau, W. K. Chin, and R. K. Cheng, “Freely propagating open premixed turbulent flames stabilized by swirl,” in *Symposium (International) on Combustion*, vol. 24, pp. 511–518, 1992.
- [20] R. K. Cheng, “Velocity and Scalar Characteristics of Premixed Turbulent Flames Stabilized by Weak Swirl,” *Combustion and Flame*, vol. 101, no. 1-2, pp. 1–14, 1995.
- [21] T. Plessing, C. Kortschik, N. Peters, M. S. Mansour, and R. K. Cheng, “Measurements of the turbulent burning velocity and the structure of premixed flames on a low-swirl burner,” in *Proceedings of the Combustion Institute*, vol. 28, pp. 359–366, 2000.
- [22] I. G. Shepherd and R. K. Cheng, “The Burning Rate of Premixed Flames in Moderate and Intense Turbulence,” *Combustion and Flame*, vol. 127, no. 3, pp. 2066–2075, 2001.
- [23] R. K. Cheng, I. G. Shepherd, B. Bédard, and L. Talbot, “Premixed turbulent flame structures in moderate and intense isotropic turbulence,” *Combustion Science and Technology*, vol. 174, no. 1, pp. 29–59, 2002.

- [24] I. G. Shepherd, R. K. Cheng, T. Plessing, C. Kortschik, and N. Peters, “Pre-  
mixed flame front structure in intense turbulence,” in *Proceedings of the Com-  
bustion Institute*, vol. 29, pp. 1833–1840, 2002.
- [25] C. Kortschik, T. Plessing, and N. Peters, “Laser optical investigation of turbu-  
lent transport of temperature ahead of the preheat zone in a premixed flame,”  
*Combustion and Flame*, vol. 136, no. 1-2, pp. 43–50, 2004.
- [26] L. P. H. de Goey, T. Plessing, R. T. E. Hermanns, and N. Peters, “Analysis of  
the flame thickness of turbulent flamelets in the thin reaction zones regime,” in  
*Proceedings of the Combustion Institute*, vol. 30, pp. 859–866, 2005.
- [27] J. B. Bell, R. K. Cheng, M. S. Day, and I. G. Shepherd, “Numerical simulation  
of Lewis number effects on lean premixed turbulent flames,” in *Proceedings of  
the Combustion Institute*, vol. 31, pp. 1309–1317, 2007.
- [28] D. T. Yegian and R. K. Cheng, “Development of a lean premixed low-swirl  
burner for low NO<sub>x</sub> practical applications,” *Combustion Science and Technol-  
ogy*, vol. 139, no. 1, pp. 207–227, 1998.
- [29] R. K. Cheng, D. T. Yegian, M. M. Miyasato, G. S. Samuelsen, C. E. Benson,  
R. Pellizzari, and P. Loftus, “Scaling and development of low-swirl burners for  
low-emission furnaces and boilers,” in *Proceedings of the Combustion Institute*,  
vol. 28, pp. 1305–1313, 2000.
- [30] D. Littlejohn, A. J. Majeski, S. Tonse, C. Castaldini, and R. K. Cheng, “Labo-  
ratory investigation of an ultralow NO<sub>x</sub> premixed combustion concept for indus-  
trial boilers,” in *Proceedings of the Combustion Institute*, vol. 29, pp. 1115–1121,  
2002.
- [31] M. R. Johnson, D. Littlejohn, W. A. Nazeer, K. O. Smith, and R. K. Cheng, “A  
comparison of the flowfields and emissions of high-swirl injectors and low-swirl

- injectors for lean premixed gas turbines,” in *Proceedings of the Combustion Institute*, vol. 30, pp. 2867–2874, 2005.
- [32] W. A. Nazeer, K. O. Smith, P. Sheppard, R. K. Cheng, and D. Littlejohn, “Full scale testing of a low swirl fuel injector concept for ultra-low NO<sub>x</sub> gas turbine combustion systems,” in *Proceedings of ASME Turbo Expo GT2006-90150*, 2006.
- [33] R. K. Cheng, D. Littlejohn, W. A. Nazeer, and K. O. Smith, “Laboratory studies of the flow field characteristics of low-swirl injectors for adaptation to fuel-flexible turbines,” in *Proceedings of ASME Turbo Expo GT2006-90878*, 2006.
- [34] R. K. Cheng, D. Littlejohn, W. A. Nazeer, and K. O. Smith, “Laboratory Studies of the Flow Field Characteristics of Low-Swirl Injectors for Adaptation to Fuel-Flexible Turbines,” *Journal of Engineering for Gas Turbines and Power*, vol. 130, p. 021501, 2008.
- [35] R. K. Cheng and D. Littlejohn, “Effects of combustor geometry on the flowfields and flame properties of a low-swirl injector,” in *Proceedings of ASME Turbo Expo GT2008-50504*, 2008.
- [36] R. K. Cheng and D. Littlejohn, “Laboratory Study of Premixed H<sub>2</sub>-Air and H<sub>2</sub>-N<sub>2</sub>-Air Flames in a Low-Swirl Injector for Ultralow Emissions Gas Turbines,” *Journal of Engineering for Gas Turbines and Power*, vol. 130, p. 031503, 2008.
- [37] D. Littlejohn and R. K. Cheng, “Fuel effects on a low-swirl injector for lean premixed gas turbines,” in *Proceedings of the Combustion Institute*, vol. 31, pp. 3155–3162, 2007.
- [38] R. K. Cheng, D. Littlejohn, P. A. Strakey, and T. Sidwell, “Laboratory investigations of a low-swirl injector with H<sub>2</sub> and CH<sub>4</sub> at gas turbine conditions,” in *Proceedings of the Combustion Institute*, vol. 32, pp. 3001–3009, 2009.

- [39] D. Littlejohn, R. K. Cheng, D. R. Noble, and T. Lieuwen, “Laboratory Investi- 2031  
gations of Low-Swirl Injectors Operating With Syngases,” *Journal of Engineer-* 2032  
*ing for Gas Turbines and Power*, vol. 132, p. 011502, 2010. 2033
- [40] P. Petersson, J. Olofsson, C. Brackman, H. Seyfried, J. Zetterberg, M. Richter, 2034  
M. Aldén, M. A. Linne, R. K. Cheng, A. Nauert, D. Geyer, and A. Dreizler, “Si- 2035  
multaneous PIV/OH-PLIF, Rayleigh thermometry/OH-PLIF and stereo PIV 2036  
measurements in a low-swirl flame,” *Applied Optics*, vol. 46, no. 19, pp. 3928– 2037  
3936, 2007. 2038
- [41] R. H. Barnes, C. E. Moeller, J. F. Kircher, and C. M. Verber, “Dye-Laser 2039  
Excited CH Flame Fluorescence,” *Applied Optics*, vol. 12, no. 11, pp. 2531– 2040  
2532, 1973. 2041
- [42] J. F. Verdieck and P. A. Bonczyk, “Laser-induced saturated fluorescence in- 2042  
vestigations of CH, CN and NO in flames,” in *Symposium (International) on* 2043  
*Combustion*, vol. 18, pp. 1559–1566, 1981. 2044
- [43] M. G. Allen, R. D. Howe, and R. K. Hanson, “Digital imaging of reaction zones 2045  
in hydrocarbon-air flames using planar laser-induced fluorescence of CH and 2046  
 $C_2$ ,” *Optics Letters*, vol. 11, no. 3, pp. 126–128, 1986. 2047
- [44] M. Namazian, R. L. Schmitt, and M. B. Long, “Two-wavelength single laser CH 2048  
and  $CH_4$  imaging in a lifted turbulent diffusion flame,” *Applied Optics*, vol. 27, 2049  
no. 17, pp. 3597–3600, 1986. 2050
- [45] R. W. Schefer, M. Namazian, and J. Kelly, “Stabilization of lifted turbulent-jet 2051  
flames,” *Combustion and Flame*, vol. 99, no. 1, pp. 75–86, 1994. 2052
- [46] P. H. Paul and J. E. Dec, “Imaging of reaction zones in hydrocarbon-air flames 2053  
by use of planar laser-induced fluorescence of CH,” *Optics Letters*, vol. 19, 2054  
no. 13, pp. 998–1000, 1994. 2055

- [47] C. D. Carter, J. M. Donbar, and J. F. Driscoll, “Simultaneous CH planar laser-  
induced fluorescence and particle imaging velocimetry in turbulent nonpremixed  
flames,” *Applied Physics B: Lasers and Optics*, vol. 66, no. 1, pp. 129–132, 1998.
- [48] K. A. Watson, K. M. Lyons, J. M. Donbar, and C. D. Carter, “Observations  
on the Leading Edge in Lifted Flame Stabilization,” *Combustion and Flame*,  
vol. 119, no. 1-2, pp. 199–202, 1999.
- [49] K. A. Watson, K. M. Lyons, J. M. Donbar, and C. D. Carter, “Simultaneous  
Rayleigh Imaging and CH-PLIF Measurements in a Lifted Jet Diffusion Flame,”  
*Combustion and Flame*, vol. 123, no. 1–2, pp. 252–265, 2000.
- [50] J. M. Donbar, J. F. Driscoll, and C. D. Carter, “Reaction Zone Structure in  
Turbulent Nonpremixed Jet Flames—From CH-OH PLIF Images,” *Combustion  
and Flame*, vol. 122, no. 1-2, pp. 1–19, 2000.
- [51] D. Han and M. G. Mungal, “Simultaneous measurement of velocity and CH  
layer distribution in turbulent non-premixed flames,” in *Proceedings of the Com-  
bustion Institute*, vol. 28, pp. 261–267, 2000.
- [52] P. S. Kothnur, M. S. Tsurikov, N. T. Clemens, J. M. Donbar, and C. D. Carter,  
“Planar imaging of CH, OH, and velocity in turbulent non-premixed jet flames,”  
in *Proceedings of the Combustion Institute*, vol. 29, pp. 1921–1927, 2002.
- [53] D. Han and M. G. Mungal, “Simultaneous measurements of velocity and CH  
distributions. Part 1: jet flames in co-flow,” *Combustion and Flame*, vol. 132,  
no. 3, pp. 565–590, 2003.
- [54] D. Han and M. G. Mungal, “Simultaneous measurements of velocity and CH  
distributions. Part II: deflected jet flames,” *Combustion and Flame*, vol. 133,  
no. 1–2, pp. 1–17, 2003.

- [55] J. A. Sutton and J. F. Driscoll, “Optimization of CH fluorescence diagnostics in flames: range of applicability and improvements with hydrogen addition,” *Applied Optics*, vol. 42, no. 15, pp. 2819–2828, 2003.
- [56] Z. S. Li, J. Zetterberg, M. Linvin, M. Aldén, J. Kiefer, T. Seeger, and A. Leipertz, “Planar laser-induced fluorescence of combustion intermediates in turbulent methane/air flames stabilized on a co-axial jet flame burner,” in *Proceedings of the European Combustion Meeting, ECM2007, Chania, Crete, Greece*, vol. 3, pp. 5–12–1–6, 2007.
- [57] J. Kiefer, Z. Li, J. Zetterberg, M. Linvin, and M. Aldén, “Simultaneous laser-induced fluorescence and sub-Doppler polarization spectroscopy of the CH radical,” *Optics Communications*, vol. 270, no. 2, pp. 347–352, 2007.
- [58] Z. S. Li, M. Afzelius, J. Zetterberg, and M. Aldén, “Applications of a single-longitudinal-mode alexandrite laser for diagnostics of parameters of combustion interest,” *Review of Scientific Instruments*, vol. 75, no. 10, pp. 3208–3215, 2004.
- [59] G. Damköhler, “Der Einfluss der Turbulenz auf die Flammengeschwindigkeit in Gasgemischen (Influence of turbulence on the velocity of flames in gas mixtures),” *Zeitschrift für Elektrochemie und Angewandte Physikalische Chemie*, vol. 46, no. 11, pp. 601–626, 1940.
- [60] R. Borghi, *On the structure and morphology of turbulent premixed flames*, pp. 117–138. Plenum Press, New York, 1985.
- [61] A. C. Eckbreth, *Laser diagnostics for combustion temperature and species*. CRC, 1996.
- [62] J. W. Daily, “Laser induced fluorescence spectroscopy in flames,” *Progress in Energy and Combustion Science*, vol. 23, no. 2, pp. 133–199, 1997.

- [63] J. Luque and D. R. Crosley, “Electronic transition moment and rotational transition probabilities in CH. II.  $B^2\Sigma^- - X^2\Pi$  system,” *Journal of Chemical Physics*, vol. 104, no. 11, pp. 3907–3913, 1996.
- [64] N. L. Garland and D. R. Crosley, “Energy transfer processes in CH  $A^2\Delta$  and  $B^2\Sigma^-$  in an atmospheric pressure flame,” *Applied Optics*, vol. 24, no. 23, pp. 4229–4237, 1985.
- [65] G. Richmond, M. L. Costen, and K. G. McKendrick, “Collision-Partner Dependence of Energy Transfer between the CH  $A^2\Delta$  and  $B^2\Sigma^-$  States,” *The Journal of Physical Chemistry A*, vol. 109, no. 4, pp. 542–553, 2005.
- [66] E. F. van Dishoeck, “Photodissociation processes in the CH molecule,” *The Journal of Chemical Physics*, vol. 86, no. 1, pp. 196–214, 1987.
- [67] J. Luque, R. J. H. Klein-Douwel, J. B. Jeffries, and D. R. Crosley, “Collisional processes near the CH  $B^2\Sigma^- v' = 0, 1$  predissociation limit in laser-induced fluorescence flame diagnostics,” *Applied Physics B: Lasers and Optics*, vol. 71, no. 1, pp. 85–94, 2000.
- [68] J. Luque and D. R. Crosley, “Electronic transition moment and rotational transition probabilities in CH. I.  $A^2\Delta - X^2\Pi$  system,” *Journal of Chemical Physics*, vol. 104, no. 6, pp. 2146–2155, 1996.
- [69] P. F. Bernath, “The vibration-rotation spectrum of CH( $X^2\Pi$ ),” *The Journal of Chemical Physics*, vol. 86, no. 9, pp. 4838–4842, 1987.
- [70] A. Marshall, P. Venkateswaran, D. Noble, J. Seitzman, and T. Lieuwen, “Development and characterization of a variable turbulence generation system,” *Experiments in Fluids*, vol. 51, no. 3, pp. 611–620, 2011.

- [71] A. Melling, "Tracer particles and seeding for particle image velocimetry," *Measurement Science and Technology*, vol. 8, no. 1, pp. 1406–1416, 1997. 2127 2128
- [72] B. Hemmerling, "Beam steering effects in turbulent high-pressure flames," in *Proceedings of SPIE*, vol. 3108, pp. 32–37, 1997. 2129 2130
- [73] C. J. Dasch, "One-dimensional tomography: a comparison of abel, onion-peeling, and filtered backprojection methods," *Applied Optics*, vol. 31, no. 8, pp. 1146–1152, 1992. 2131 2132 2133
- [74] N. L. Garland and D. R. Crosley, "Relative transition probability measurements in the  $A - X$  and  $B - X$  systems of CH," *Journal of Quantitative Spectroscopy and Radiative Transfer*, vol. 33, no. 6, pp. 591–595, 1985. 2134 2135 2136
- [75] C. J. Nokes, G. Gilbert, and R. J. Donovan, "Direct kinetic study of  $\text{CH}(A^2\Delta)$ ," *Chemical Physics Letters*, vol. 99, no. 5-6, pp. 491–493, 1983. 2137 2138
- [76] F. L. Tabarés and A. G. U. na, "Electronic quenching of  $\text{CH}(A^2\Delta - X^2\Pi)$  and  $\text{OH}(A^2\Sigma^+ - X^2\Pi)$  by  $\text{N}_2$  and  $\text{O}_2$ ," *Journal of Photochemistry*, vol. 21, no. 4, pp. 281–289, 1983. 2139 2140 2141
- [77] T. A. Cool and P. J. H. Tjossem, "Direct observations of chemi-ionization in hydrocarbon flames enhanced by laser excited  $\text{CH}^*(A^2\Delta)$  and  $\text{CH}^*(B^2\Sigma^-)$ ," *Chemical Physics Letters*, vol. 111, no. 1-2, pp. 82–88, 1984. 2142 2143 2144
- [78] C. J. Nokes and R. J. Donovan, "Time-resolved kinetic studies of electronically excited CH radicals. II. Quenching efficiencies for  $\text{CH}(A^2\Delta)$ ," *Chemical Physics*, vol. 90, no. 1-2, pp. 167–174, 1984. 2145 2146 2147
- [79] N. L. Garland and D. R. Crosley, "On the collisional quenching of electronically excited OH, NH and CH in flames," in *Symposium (International) on Combustion*, vol. 21, pp. 1693–1702, 1986. 2148 2149 2150



- [80] N. L. Garland and D. R. Crosley, “Collisional quenching of CH  $A^2\Delta$ ,  $v' = 0$  at 1300 K,” *Chemical Physics Letters*, vol. 134, no. 2, pp. 189–194, 1987.
- [81] P. Heinrich, R. D. Kenner, and F. Stuhl, “Collisional quenching at 300 K: CH( $A^2\Delta$ ) by H<sub>2</sub>O, NH<sub>3</sub> and other gases and NH( $A^3\Pi$ ) by H<sub>2</sub>O,” *Chemical Physics Letters*, vol. 147, no. 6, pp. 575–580, 1988.
- [82] K. J. Rensberger, M. J. Dyer, and R. A. Copeland, “Time-resolved CH( $A^2\Delta$  and  $B^2\Sigma^-$ ) laser-induced fluorescence in low pressure hydrocarbon flames,” *Applied Optics*, vol. 27, no. 17, pp. 3679–3689, 1988.
- [83] D. E. Heard, J. B. Jeffries, and D. R. Crosley, “Collisional quenching of  $A^2\Sigma^+$  NO and  $A^2\Delta$  CH in low pressure flames,” *Chemical Physics Letters*, vol. 178, no. 5,6, pp. 533–537, 1991.
- [84] R. D. Kenner, S. Pfannenberger, P. Heinrich, and F. Stuhl, “Electronic Quenching of CH( $A^2\Delta$ ), NH( $A^3\Pi$ ), NH( $c^1\Pi$ ), and PH( $A^3\Pi$ ) between 240 and 420 K,” *The Journal of Physical Chemistry*, vol. 95, no. 17, pp. 6585–6593, 1991.
- [85] C. Chen, X. Wang, S. Yu, Q. Lu, and X. Ma, “Collisional quenching of CH( $A^2\Delta$ ) at 300 K by O<sub>2</sub>, alkane, chloromethane and CS<sub>2</sub> molecules,” *Chemical Physics Letters*, vol. 197, no. 3, pp. 286–291, 1992.
- [86] J. L. Cooper and J. C. Whitehead, “Collisional Removal Rates for Electronically Excited CH Radicals  $B^2\Sigma^-$  and  $C^2\Sigma^+$ ,” *Journal of the Chemical Society, Faraday Transactions*, vol. 88, no. 16, pp. 2323–2327, 1992.
- [87] C. Chen, Q. Ran, S. Yu, and X. Ma, “Time-resolved kinetic studies on quenching of CH( $A^2\Delta$  and  $B^2\Sigma^-$ ) by (CX<sub>3</sub>)<sub>2</sub>CO, CF<sub>3</sub>COOX, and CXCl<sub>3</sub> (X=H or D) and alkane molecules,” *The Journal of Chemical Physics*, vol. 99, no. 2, pp. 1070–1075, 1993.

- [88] C. Chen, Y. Sheng, S. Yu, and X. Ma, “Investigation of the collisional quenching  
of  $\text{CH}(A^2\Delta$  and  $B^2\Sigma^-)$  by Ar,  $\text{O}_2$ ,  $\text{CS}_2$ , alcohol, and halomethane molecules,”  
*The Journal of Chemical Physics*, vol. 101, no. 7, pp. 5727–5730, 1994.
- [89] P. Heinrich and F. Stuhl, “Electronic Quenching of  $\text{CH}(A^2\Delta)$  and  $\text{NH}(A^3\Pi)$   
between 300 and 950 K,” *Chemical Physics*, vol. 199, no. 1, pp. 105–118, 1995.
- [90] C. Chen, F. Wang, Y. Chen, and X. Ma, “Temperature effect on quenching of  
 $\text{CH}(A^2\Delta)$ ,” *Chemical Physics*, vol. 230, no. 2–3, pp. 317–325, 1998.
- [91] M. Tamura, P. A. Berg, J. E. Harrington, J. Luque, J. B. Jeffries, G. P. Smith,  
and D. R. Crosley, “Collisional Quenching of  $\text{CH}(A)$ ,  $\text{OH}(A)$ , and  $\text{NO}(A)$  in  
Low Pressure Hydrocarbon Flames,” *Combustion and Flame*, vol. 114, no. 3–4,  
pp. 502–514, 1998.
- [92] C. Cerezo and M. Martin, “Rotational level dependence in the collisional re-  
moval of  $\text{CH}/\text{D}(A^2\Delta)$ ,” *Journal of Photochemistry and Photobiology A: Chem-  
istry*, vol. 134, no. 1–2, pp. 127–132, 2000.
- [93] M. W. Renfro, K. K. Venkatesan, and N. M. Laurendeau, “Cross sections for  
quenching of  $\text{CH } A^2\Delta, v' = 0$ , by  $\text{N}_2$  and  $\text{H}_2\text{O}$  from 1740 to 2160 K,” in *Pro-  
ceedings of the Combustion Institute*, vol. 29, pp. 2695–2702, 2002.
- [94] C. J. Randall, C. Murray, and K. G. McKendrick, “State-specific collisional cou-  
pling of the  $\text{CH } A^2\Delta$  and  $B^2\Sigma^-$  states,” *Physical Chemistry Chemical Physics*,  
vol. 2, no. 4, pp. 461–471, 2000.
- [95] M. Zachwieja, “New Investigations of the  $A^2\Delta - X^2\Pi$  Band System in the  
 $\text{CH}$  Radical and a New Reduction of the Vibration-Rotation Spectrum of  $\text{CH}$   
from the ATMOS Spectra,” *Journal of Molecular Spectroscopy*, vol. 170, no. 2,  
pp. 285–309, 1995.

- [96] P. A. Berg, D. A. Hill, A. R. Noble, G. P. Smith, J. B. Jeffries, and D. R. 2199  
Crosley, “Absolute CH Concentration Measurements in Low-Pressure Methane 2200  
Flames: Comparisons with Model Results,” *Combustion and Flame*, vol. 121, 2201  
no. 1-2, pp. 223–235, 2000. 2202
- [97] S. H. Stårner and R. W. Bilger, “Joint measurements of velocity and scalars in 2203  
turbulent diffusion flame with moderate swirl,” in *Symposium (International)* 2204  
*on Combustion*, vol. 21, pp. 1569–1577, 1986. 2205
- [98] H. Kobayashi, Y. Kawabata, and K. Maruta, “Experimental study on general 2206  
correlation of turbulent burning velocity at high pressure,” in *Symposium (In-* 2207  
*ternational) on Combustion*, vol. 27, pp. 941–948, 1998. 2208
- [99] H. Kobayashi, “Experimental study of high-pressure turbulent premixed 2209  
flames,” *Experimental Thermal and Fluid Science*, vol. 26, no. 2, pp. 375–387, 2210  
2002. 2211
- [100] P. Griebel, P. Siewert, and P. Jansohn, “Flame characteristics of turbulent lean 2212  
premixed methane/air flames at high pressure: Turbulent flame speed and flame 2213  
brush thickness,” in *Proceedings of the Combustion Institute*, vol. 31, pp. 3083– 2214  
3090, 2007. 2215
- [101] H. Kobayashi, T. Nakashima, T. Tamura, K. Maruta, and T. Niioka, “Tur- 2216  
bulence Measurements and Observations of Turbulent Premixed Flames at El- 2217  
evated Pressures up to 3.0 MPa,” *Combustion and Flame*, vol. 108, no. 1-2, 2218  
pp. 104–117, 1997. 2219